

**ADDITIVELY MANUFACTURED SHAPE-CHANGING RF DEVICES ENABLED
BY ORIGAMI-INSPIRED STRUCTURES**

A Dissertation
Presented to
The Academic Faculty

By

Yepu Cui

In Partial Fulfillment
of the Requirements for the Degree
Doctor of Philosophy in the
School of Electrical and Computer Engineering

Georgia Institute of Technology

December 2022

Copyright © Yepu Cui 2022

**ADDITIVELY MANUFACTURED SHAPE-CHANGING RF DEVICES ENABLED
BY ORIGAMI-INSPIRED STRUCTURES**

Approved by:

Dr. Manos M. Tentzeris, Advisor
School of Electrical Engineering
Georgia Institute of Technology

Dr. Andrew F. Peterson
School of Electrical Engineering
Georgia Institute of Technology

Dr. Gregory D. Durgin
School of Electrical Engineering
Georgia Institute of Technology

Dr. Suresh K. Sitaraman
School of Mechanical Engineering
Georgia Institute of Technology

Dr. Sungjoon Lim
Department of Electrical and Elec-
tronics Engineering
Chung-Ang University

Date Approved: August 15, 2022

认准了，就去做，不跟风，不动摇。

李彦宏

Just do it if you have determined, don't follow suit, don't hesitate.

Robin Li

For my parents.

ACKNOWLEDGEMENTS

I would like to express my great gratitude to my advisor, Dr. Manos M. Tentzeris, for his guidance and support throughout my Ph.D. career. His support for new ideas encourages me to take challenges, think differently, and be creative, which are invaluable skills that will benefit my entire career. He also provides me countless opportunities to expose myself to both the academia and the industry to help me make confident career decisions. Our group agreed he is the best advisor possible.

I would also like to thank my proposal and defence committee members for providing me feedbacks and guidances selflessly.

My deepest appreciation also goes to my ATHENA group members, including but not limited to: Dr. Ajibayo Adeyeye, Dr. Aline Eid, Dr. Ali Alreshaid, Dr. Bijan Tehrani, Charles Lynch, Dr. Eui Min Jung, Dr. Jimmy G.D. Hester, Kexin Hu, Dr. Ryan Bahr, Dr. Salem A. Alotaibi, Dr. Soyeon Jeong, Dr. Syed Abdullah Nauroze, Dr. Tong-hong Lin, Dr. Wenjing Su, Dr. Xuanke He, Dr. Yunnan Fang... I will never forget the countless late night researches and group events we spent together.

Finally, I would like to thank my parents Quanhua Li and Shijun Cui for their love and support.

TABLE OF CONTENTS

Acknowledgments	v
List of Tables	x
List of Figures	xi
Summary	xvii
Chapter 1: Introduction	1
1.1 Motivation	1
1.2 Thesis Outline	2
Chapter 2: Previous Efforts in Shape-changing Origami-inspired RF Devices . .	4
2.1 Origami-inspired Reconfigurable Frequency Selective Surfaces (FSSs) . . .	5
2.1.1 Single Layer Origami-inspired FSS	5
2.1.2 Multi-layer Origami-inspired FSS	7
2.2 Origami-inspired Antennas	8
2.2.1 Folded Origami-inspired Antennas	9
2.2.2 3D Printed Origami-inspired Antennas	11
2.3 Summary	13

Chapter 3: Review of Additive Manufacturing Techniques and Additively Manufactured RF Devices	15
3.1 Overview of Various AM Technologies	15
3.2 Additively Manufactured RF Devices	17
3.2.1 Antennas	19
3.2.2 System on Packages/Antennas	20
3.2.3 RFID Sensors	22
3.3 Summary	23
Chapter 4: Hybrid Printing Process	25
4.1 Hybrid Printing Process For Shape-changing RF Devices	26
4.1.1 3D Printed Dielectric Substrate	27
4.1.2 Inkjet Printed Buffer Layers	28
4.1.3 Inkjet Printed Conductor Patterns	31
4.2 Hybrid Printed Origami-inspired reconfigurable FSS	33
4.2.1 Single Layer Miura-ori FSS	33
4.2.2 Multi-layer Miura FSS	38
4.3 Hybrid Printed Pressure Sensors	42
4.3.1 Hybrid Printed Planar Pressure Sensor Using Metamaterial Absorber	43
4.3.2 Hybrid Printed Planar Pressure Sensor Using Substrate Integrated Waveguide (SIW) Technology	46
Chapter 5: 3D Printed “Kirigami”-Inspired Deployable Bi-focal Beam-scanning Dielectric Reflectarray	48
5.1 Introduction	48

5.2	Element Design and Analysis	50
5.2.1	Mechanical Design	50
5.2.2	RF Design	53
5.3	Reflectarray Design, Fabrication and Measurement	54
5.3.1	Reflectarray Design	54
5.3.2	Fabrication	60
5.3.3	Simulation and Measurement Results	62
5.4	Summary	65
 Chapter 6: Truly Conformal Tile-based Beamforming Phased Array With Novel 3D Depth Camera Calibration		 67
6.1	Introduction	67
6.2	3D Depth Camera	68
6.2.1	Proof-of-concept Experiments	69
6.2.2	Phased Array Tile	79
 Chapter 7: Additional Research: A Novel 4-DOF Wide-range Tunable Frequency Selective Surface Using Origami "Eggbox" Structure		 88
7.1	Introduction	88
7.2	Element Design	89
7.2.1	Mechanical Design	89
7.2.2	RF Design	90
7.3	6×6 Eggbox FSS Design	92
7.3.1	Mechanical Simulation	92
7.3.2	Fabrication	93

7.3.3	Simulation and Measurement Results	94
7.4	Summary	98
 Chapter 8: Additional Research: 3D-printing and Characterization of Polyte- trafluoroethylene (PTFE) Demonstrating Extremely Low Loss mm- Wave Dielectric Reflectarrays		
8.1	Introduction	100
8.2	3D Printing and Characterization of PTFE	102
8.3	Extremely Low Loss mm-Wave Dielectric Reflectarrays	105
8.3.1	Unit Cell Design and Simulation	105
8.3.2	Array Design	108
8.3.3	Fabrication, Results, and Discussion	110
8.4	Summary	112
 Chapter 9: Contributions and Potential Future Works		
9.1	Contributions	114
9.1.1	Fabrication Improvement	114
9.1.2	Novel Shape-changing RF Designs	115
9.2	Potential Future Works	115
9.2.1	Fabrication Improvement	115
9.2.2	Novel Shape-changing RF Designs	116
 References		130

LIST OF TABLES

3.1	Capabilities and Limitations of Inkjet and Aerosol-jet Printing	16
3.2	Capabilities and Limitations of Various 3D Printing Technologies	18
4.1	Variance of the measured surface profile	30
4.2	Equivalent inductance of the single layer Miura FSS	37
4.3	Bandwidth Comparison Between Single and Multi-layer M-FSS	42
4.4	Insertion Loss Performance Comparison Between Single-layer and Multi-layer Designs.	43
5.1	Performance Comparison of Different Phase Offset	60
5.2	Summary of The Measurement Results @30 GHz	65
5.3	State-of-the-art Comparison	65
6.1	Rotation Angle Detection Preliminary Measurement Results	80
6.2	Summary of the Single Tile Performance	84
6.3	Summary of the 2-Tile Array Performance	87
7.1	Performance comparison of typical origami inspired FSS	97
8.1	Material Properties of Commonly Used SLA and FDM Materials	104
8.2	Measured Performance of the SLA PTFE DR and Formlabs Clear DR . . .	112

LIST OF FIGURES

2.1	One of the first origami-inspired FSS: (a) Miura-ori unit cell structure [8], (b) Miura-ori FSS with cross-shaped elements [8].	6
2.2	Miura-ori FSS with dipole-shaped conductive traces: (a) 1-RiM configuration with two conductive traces on one Miura-ori element [9], (b) 3-RiM configuration with two conductive traces across three Miura-ori elements [9].	6
2.3	Miura-ori FSS with rhombic loop resonators: (a) a 4×3 configuration showing the unit cell at different folding states. [11], (b) fabricated FSS on a polyimide substrate [11].	7
2.4	Miura-ori-based FSSs with multilayer configurations: (a) “mirror-stacked”, (b) “inline-stacked”[12].	8
2.5	Origami-inspired helical antennas (a) a deployable helical antenna [19] (b) a tunable Quasi-Yagi antenna realized by three origami helical antennas [22].	9
2.6	Origami “Flasher” antenna: (a)–(j) folding process, (k)–(n) transforming process from unfolded to folded states.	10
2.7	(a) Origami-inspired 4-element patch array with integrated hinge structures [27] (b) reconfigurable C-band dipole antenna array [28].	11
2.8	3D printed microfluidics-based origami antennas (a) “Chinese-fan” inspired antenna [29], (b) origami reconfigurable antenna “trees” [30].	12
2.9	3D printed SMP-based origami antennas (a) cube-shaped origami patched antenna [31], (b) packaging-integrated antenna array mounted on Broadcom BCM2835 SoC	13
3.1	(a) Formlabs Form3 SLA 3D printing system [54] (b) Fujifilm Dimatix 2800 series inkjet printer [55].	19

3.2	Additively manufactured antennas: (a) fully inkjet printed multi-layer Yagi-Uda antenna [56] (b) 3D printed Voronoi inverted feed discone antenna [58].	20
3.3	Schematic of a fully integrated 3D stacked module enabled by 3D printing and inkjet printing techniques [59].	21
3.4	Additively manufactured SoA and SoP: (a) Exploded view of the of a SoA proof-of-concept topology, with the various components required [60]. (b) Flexible system demonstrated layer by layer [61].	21
3.5	Additively manufactured RFID sensors: (a) A photo of an all-inkjet-printed microfluidic sensor[68]. (b) A 3D view of the printed microfluidic sensor [68]. (c) inkjet printed sensor platform for agriculture application [64]. . . .	23
4.1	Schematic of the hybrid printing process to realize Miura-ori FSS.	26
4.2	Prototype of the single layer hybrid printed tunable Miura-ori FSS.	27
4.3	Directions of the surface respect to the printing plane.	28
4.4	Surface profile measurement results: (a)perpendicular to the printing line; (b) Surface profile parallel to the printing line.	29
4.5	(a) Contact angle of silver nanoparticle ink before UV-Ozone treatment (b) contact angle of silver nanoparticle ink after UV-Ozone treatment.	31
4.6	Comparison of sintering process: (a) high temperature sintering (b) low temperature gradient sintering.	32
4.7	Single layer Miura-ori element: (a) an optimized Miura element with $l_1=5$ mm, $l_2=7$ mm, $\theta = 110^\circ$, $w_c=1$ mm, $l_c=6$ mm, substrate thickness=0.8 mm; (b) 3D printed Miura element with stress release structures.	33
4.8	Measurement setup with frame and holder.	34
4.9	Simulation and measurement results: (a) frequency response of single layer M-FSS($\theta=110^\circ$) for different values of angle of incidence; (b) frequency response with different values of folding angle θ	36
4.10	Equivalent circuit of the FSS.	37
4.11	Multi-layer Miura-ori element: (a) a mirror stacked Miura unit with $l_1=5$ mm, $l_2=7$ mm, $\theta = 110^\circ$, $w_c=1$ mm, $l_c=6$ mm, substrate thickness=0.7 mm; (b) 3D printed Miura unit with stress release design.	39

4.12	Fabricated mirror-stack multi-layer M-FSS.	40
4.13	Frequency response of multi-layer M-FSS($\theta=110^\circ$) for different values of angle of incidence	41
4.14	Frequency response with different values of folding angle θ	42
4.15	Design of the hybrid printed metamaerial-enabled pressure sensor: (a) perspective view; (b) top view; (c) side view.	44
4.16	COMSOL simulation results of the hybrid printed metamaerial-enabled pressure sensor.	45
4.17	Simulated and measured frequency response of the hybrid printed metamaerial-enabled pressure sensor.	45
4.18	Design of the hybrid printed SIW cavity pressure sensor in perspective view.	47
4.19	Measured frequency response of the hybrid printed SIW cavity pressure sensor.	47
5.1	Element design: (a) deployed structure and top-view of one element; (b) folded structure and a detailed schematic of the ground plane retraction mechanism.	50
5.2	Mechanical simulation results: (a) Force versus Displacement, from “Deployed” stage to “Retracted” stage; (b) maximum element height versus geometry parameters t_1, t_2, t_3 sweep around the design baseline values.	52
5.3	Formlabs Flexible80A Material Characterization Results: dielectric constant versus frequency (top); loss tangent versus frequency (bottom)	53
5.4	Simulated phase response versus element height for different AoI values at 30 GHz.	55
5.5	Simulated reflection coefficient versus element height for different AoI values at 30 GHz.	55
5.6	Schematic of the bi-focal beam scanning reflectarray setup.	56
5.7	Schematic of the phase optimization program.	58
5.8	Output of the phase optimization program: lowest phase error at 333° offset.	59

5.9	(a) Phase distribution of the bi-focal reflectarray; (b) Element height distribution of the bi-focal reflectarray.	60
5.10	Fabricated sample: (a) fully deployed sample (front side); (b) fully retracted sample (back side).	61
5.11	Measurement setup.	62
5.12	(a) Simulated and measured realized gain versus scanning angle at 30 GHz; (b) measured realized gain versus frequency at different scanning angles. . .	63
5.13	Measured and Simulated radiation patterns at 30 GHz with scan angles from -10° to -30°	64
5.14	Measured and Simulated radiation patterns at 30 GHz with scan angles from 10° to 30°	64
6.1	Detectable transformation of conformal phased array using 3D depth camera: rotation, shift, and twist.	69
6.2	The TrueDepth camera module inside an iPhone 12 Mini.	70
6.3	Projected IR dots captured by a full-spectrum modified CCD sensor with a B+W 093 900 nm IR pass filter	70
6.4	Modified app based on the SDK [114] with 3D real-time preview and data saving functions	71
6.5	Captured depth image of a computer desk transformed from uvw (left) to xyz (right) coordinate system.	72
6.6	(a) Design of the measurement setup to verify the feasibility of measuring “Rotation” angles using the TrueDepth camera; (b) 3D printed dummy samples with different rotation angles from 10° to 30°	73
6.7	First step of data processing: calibrate x-y plane; (a) raw data; (b) edge detection; (c) line detection; (d) line selection.	74
6.8	Results of the first step data processing: (a) definition of the sample holder’s plane normal; (b) without x-y plane calibration; (c) with x-y plane calibration.	75
6.9	Second step of data processing: calibrate z axis; (a) output of the first step; (b) crop the image to focus on the dummy sample; (c) line detection with lower threshold; (d) line selection.	76

6.10	Results of the second step data processing: without x-axis calibration (left); with x-axis calibration (right).	76
6.11	Third step of data processing: data sampling.	78
6.12	Curve fitting results of the left side (angle1) and right side (angle2) of the dummy sample.	78
6.13	Rotation angle detection preliminary measurement Results.	79
6.14	Concept demonstration of the conformal tile-based phased array architecture.	80
6.15	Design of a single tile	81
6.16	Simulated return loss of the single tile patch elements.	82
6.17	Simulated radiation pattern of the single tile patch elements.	83
6.18	Simulated beam steering performance of the single tile.	83
6.19	Microstrip-to-Microstrip transition.	85
6.20	Two configurations of the 2-tile array design: (a) 0° rotation angle; (b) 15° rotation angle.	85
6.21	Simulated radiation patterns for different steering angles: (a) 0° rotation angle; (b) 15° rotation angle.	86
7.1	Eggbox element design: (a) 2D flat eggbox outline pattern; (b) 3D folded eggbox structure; (c) 3D folded eggbox volumetric boundary box.	89
7.2	The variation of different geometric parameters with folding angles α from 0° to 120°	91
7.3	Design of cross-dipole eggbox FSS element: (a) perspective view; (b) top view; (c) equivalent circuit.	92
7.4	Demonstration of four degrees of freedom tuning methodology: fold along x axis; fold along y axis; rotate x axis; rotate y axis.	93
7.5	Three-step fabrication process for eggbox FSS: perforate eggbox pattern; inkjet print conductive traces; fold to 3D eggbox structure.	94

7.6	Fabricated sample of 6×6 cross-dipole eggbox FSS and incidence angles: normal incidence (blue), rotate y axis (green), rotate x axis (red).	95
7.7	Horizontal (x-axis) polarization with different folding angles simulation and measurement results.	96
7.8	Vertical (y-axis) polarization with different folding angles simulation and measurement results.	97
7.9	Resonance frequency versus folding angles of horizontal polarization (x-axis)	98
7.10	Horizontal polarization (x-axis) with different y-axis rotating angles simulation and measurement results.	98
7.11	Vertical polarization (y-axis) with different x-axis rotating angles simulation and measurement results.	99
8.1	(a) Material calibration measurement setup with WR28 waveguide to coaxial adapter, $1/4\lambda$ spacer, and test samples; (b) measured SLA PTFE dielectric constant and loss tangent from 26.5 GHz to 40 GHz.	103
8.2	Unit cell design: four elements perspective view, single element top view. ($h = 28$ mm, $l = 6$ mm, $\alpha = 90^\circ$, $t = \text{variable}$)	106
8.3	Unit cell simulation results for SLA PTFE and Formlabs Clear: phase vs wall thickness, return loss vs wall thickness.	106
8.4	Proposed DR configuration ($\theta_a = \theta_b = 20^\circ$, $h_a = 80$ mm).	107
8.5	(a) Phase control patterns for SLA PTFE DR (left) and Formlabs Clear DR (right); (b) wall thickness distribution patterns for SLA PTFE DR (left) and Formlabs Clear DR (right).	108
8.6	Fabricated prototypes: SLA PTFE DR (left), Formlabs Clear DR (right). . .	109
8.7	Radiation pattern and gain measurement setup in an anechoic chamber. . . .	110
8.8	Simulated and measured radiation patterns at 40 GHz: (a) SLA PTFE DR; (b) Foamlabs Clear DR.	111

SUMMARY

At the time of writing, we're in the midst of the revolution of the 5th generation (5G) wireless network that promises much faster data speeds and more reliable service. To meet the ambitious goals in 5G, microwave components are required to have adaptive frequency and radiation response over a wide spectrum based on the environment, region, and type of service. Traditional tunable microwave devices use active diodes, switches, phase shifters to achieve fast response, but at the same time, they can be expensive, fragile, difficult to realize, and increase the overall size of the RF system. Therefore, new topologies need to be investigated to realize high-performance tunable microwave components in a low-cost, easy to fabricate, and sustainable manner.

The work presented in this thesis explores the possibility of implementing origami-inspired shape-changing structures into microwave designs to enable continuous performance tunability as well as deployability. The research not only experimented novel structures that have unique mechanical behaviour, but also developed automated additive manufacturing (AM) fabrication process that pushes the boundary of realizable frequency from Sub-6 GHz to mm-wave. High-performance origami-inspired reconfigurable frequency selective surfaces (FSSs) and reflectarray antennas are realized for the first time at mm-wave frequencies with AM techniques. The research also investigated the idea of combining mechanical tuning and active tuning methods in a hybrid manner to realize the first truly conformal beam-forming phased array antenna that can be applied onto any arbitrary surface and can be re-calibrated with a 3D depth camera system.

CHAPTER 1

INTRODUCTION

1.1 Motivation

The exponential growth of smartphones, self driving cars, internet of things (IoT), smart cities, etc., are pushing network providers and authorities to allocate more frequency bands to fulfill the continuously increasing data traffic. Therefore, microwave devices for next generation communication systems are required have adaptive frequency response over a wider frequency range based on the environment, region, and type of service. In recent years, significant amount of research has been undertaken on reconfigurable microwave devices to realize a variable frequency response. Various of methodologies can be utilized to achieve on-demand tunability. One common approach is by introducing active components such as p-i-n diodes, varactor diodes, or microelectromechanical systems (MEMS) capacitors/switches to turn part of the device on and off or change the parasitic loading of the device. While the active tuning approach can achieve responsive and accurate frequency response, at the same time, they can be expensive, fragile and require complex biasing and feeding circuits that dramatically increase the cost and fabrication difficulty, limiting the scalability of the tunable microwave devices.

Another approach to realize reconfigurable microwave devices is by changing the geometry mechanically using foldable origami-inspired 3D structures. Microwave designs with origami-inspired structures eliminate the need of active components, featuring unprecedented capabilities for deployability, power handling, and continuous-range tunability, enabling drastic improvements in the performance of devices such as antennas, sensors, frequency selective surfaces (FSSs), etc. However, one of the biggest challenges with many origami-inspired designs is that they are utilizing paper as the substrate, which is prone to

absorbing moisture, tearing, and has significant dielectric losses. In addition, the fabrication process of paper-based origami-inspired designs is usually labor intensive involves manual cutting and folding that lacks accuracy. For these reasons, it is important to develop a new fully automated process that utilizes durable and weather resistant materials to realize origami-inspired structures to fit the needs in real-life and future mm-wave applications.

As a potential solution to this problem, additive manufacturing (AM) methods such as 3D printing and inkjet printing techniques can be utilized to deposit both dielectric and conductive materials in a 2.5D/3D fashion, where complex origami-inspired designs can be realized directly. 3D printing allows the rapid design and fabrication of free-form three dimensional objects with ease. Fully 3D printed flexible substrates eliminate the requirement of folding and cutting which enables more complicated design elements such as slots, round holes, etc. Meanwhile, inkjet printing technique allows selective deposition of wide variety of materials, including metals, dielectrics, and nano-materials. Fully automated high-accuracy additive manufacturing methodologies can also reduce the size of a unit cell, opening the potential for 5G and mm-wave applications.

1.2 Thesis Outline

This thesis explores the concept of combining 3D printing with inkjet printing technology to realize state-of-the-art origami-inspired tunable and deployable microwave devices, including mm-wave reconfigurable single- and multi-layer FSSs, high-sensitivity chipless RFID sensors, deployable antennas and arrays, etc. This thesis consists of 8 sections:

- Chapter 2 reviews the current advances and challenges of shape-changing microwave devices.
- Chapter 3 reviews various additive manufacturing technologies and additively manufactured RF devices.

- Chapter 4 presents newly developed hybrid printing process as well as hybrid printed origami-inspired FSSs and sensors.
- Chapter 5 presents the first origami-inspired high-performance antenna array enabled by a novel two-stage “snapping-like” structure.
- Chapter 6 presents the design of a truly conformal phased array system that features tile-based scalable architecture, mechanical tuning, electrical beam-steering, as well as on-the-fly calibration using computer vision and 3D depth camera.
- Chapter 7 presents the addition work on novel origami-inspired “eggbox” structure.
- Chapter 8 presents the addition work on the characterization of low-loss 3D printable dielectrics.
- Chapter 9 discusses the contributions and the potential future works.

CHAPTER 2

PREVIOUS EFFORTS IN SHAPE-CHANGING ORIGAMI-INSPIRED RF DEVICES

As discussed in Chapter 1, one of the most popular and widely used techniques to realize tunable RF structures is by using electronic components (such as diodes, varactors, and microelectromechanical systems) to change the electromagnetic properties of the resonant structures. These structures can achieve high tuning speed but they suffer from a high failure rate and limited tunability range, and become harder to realize as their overall size increases. Other techniques include using ferrite substrates and integrated microfluidic channels that change the RF structures' electromagnetic response by varying the substrate's effective permittivity and selectively loading the resonant structures, respectively. However, they require high operating voltages and are hard to control.

While origami-inspired RF structures present a promising methodology to realize novel communication modules and systems for next-generation mm-wave systems, they present a number of novel challenges that need to be addressed for a robust design. These include the realization of truly flexible conductive traces, multilayer configuration with interconnects (that maintain high conductivity during folding or bending process), folding automation techniques (especially for thick substrates), mathematical modeling of origami structures (including its kinematics and design), and their relationship to the EM behavior of the RF structures. In this work, inkjetprinting technology is used to fabricate highly flexible conductive traces as it facilitates rapid fabrication of complex multilayer multimaterial 2D/3D flexible RF structures on a wide range of substrates.

2.1 Origami-inspired Reconfigurable Frequency Selective Surfaces (FSSs)

Frequency selective surface (FSS) is a periodic structure with arrays of elements arranged on a dielectric substrate to absorb, reflect, or transmit electromagnetic waves based on the frequency [1]. The frequency response of an FSS can be determined by the element shape, size, distribution, and the type of the dielectric substrate. FSSs have found great range of applications including spatial frequency filtering, electromagnetic shielding, absorbers, radomes, sensors, etc. In recent years, a significant amount of research has been undertaken on reconfigurable FSSs to realize a variable frequency response. Various methodologies can be utilized to achieve on-demand tunability, with one common approach is by introducing active components such as p–i–n diodes [2, 3], varactor diodes [4, 5], or microelectromechanical systems (MEMS) capacitors/switches [6, 7] to tune the parasitics of the FSS equivalent circuits. This active tuning approach can be responsive and accurate. However, those active components can also be expensive, fragile, and require complex biasing circuits that dramatically increase the cost and fabrication difficulty, limiting the scalability of the reconfigurable FSS.

Another approach to realize reconfigurable FSSs is by changing the shape mechanically using foldable origami-inspired 3D structures. A great number of origami-inspired 3D FSSs have been studied in recent years, showing unprecedented capabilities for deployability and continuous-range tunability.

2.1.1 Single Layer Origami-inspired FSS

Miura-ori shown in Fig.2.1a is one of the most commonly used element structures in origami-inspired 3D FSS designs. One of the first origami-inspired FSS utilizes Miura-ori structure was presented in [8] in 2012 with 40×40 elements realized on a paper-based substrate, each element contains four chemically etched cross-shaped conductive patterns (Fig. 2.1b). When folding the structure, the equivalent electrical length of the conductive

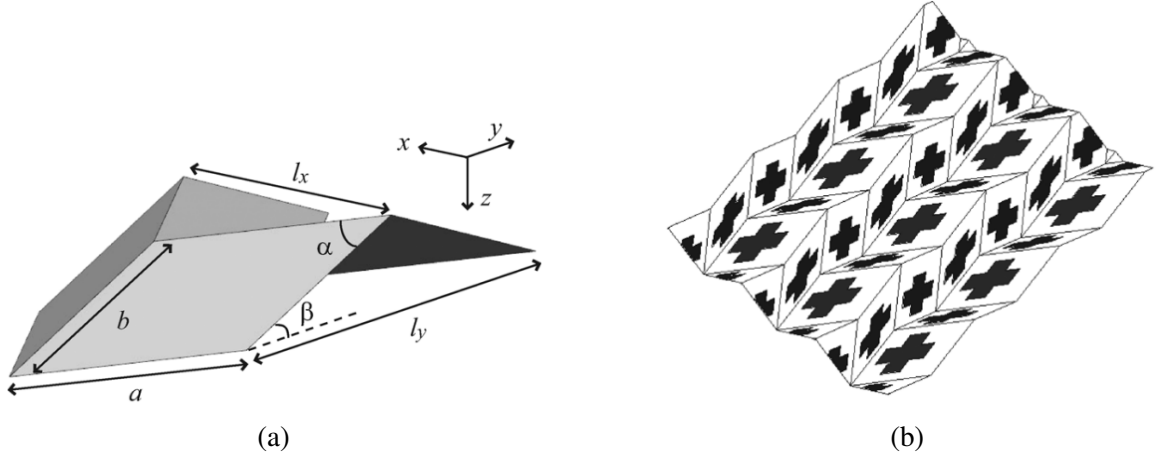


Figure 2.1: One of the first origami-inspired FSS: (a) Miura-ori unit cell structure [8], (b) Miura-ori FSS with cross-shaped elements [8].

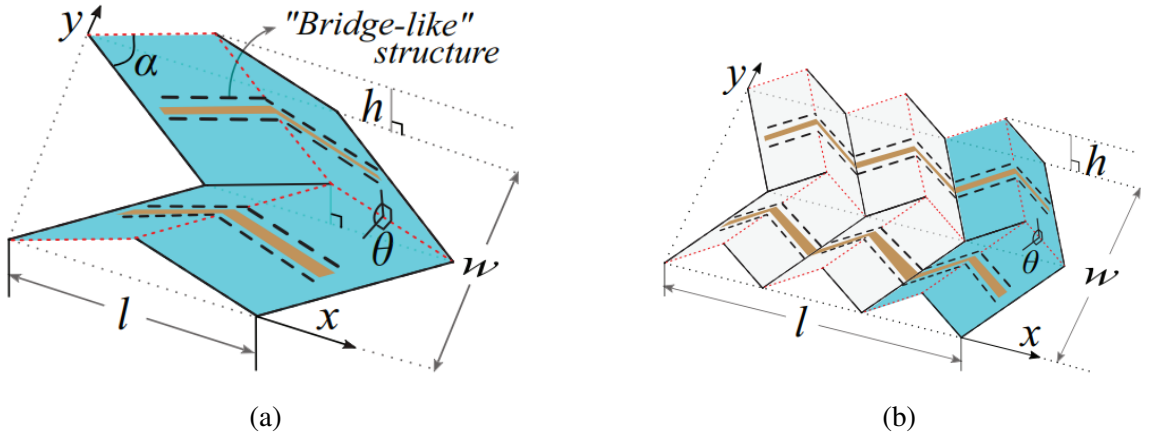


Figure 2.2: Miura-ori FSS with dipole-shaped conductive traces: (a) 1-RiM configuration with two conductive traces on one Miura-ori element [9], (b) 3-RiM configuration with two conductive traces across three Miura-ori elements [9].

patterns will be reduced, as a result, the resonate frequency can be tuned from 10 GHz to 11 GHz. However, for this cross-shaped design, the frequency response is very sensitive to the angle of incidence (AoI) due to the strong inter-element coupling.

Later in 2017, [10] presented a Miura-ori-based FSS utilizes dipole-shaped element (Fig. 2.2a) that can be tuned from 7.2 GHz to 8.2 GHz. The dipole-shaped element has more stable frequency response under larger AoI as it only has one polarization. By expanding the length of the dipole elements, the conductor can span across multiple foldlines and morph into a ripple-shaped structure as shown in Fig. 2.2b. With this “n-RiM” config-

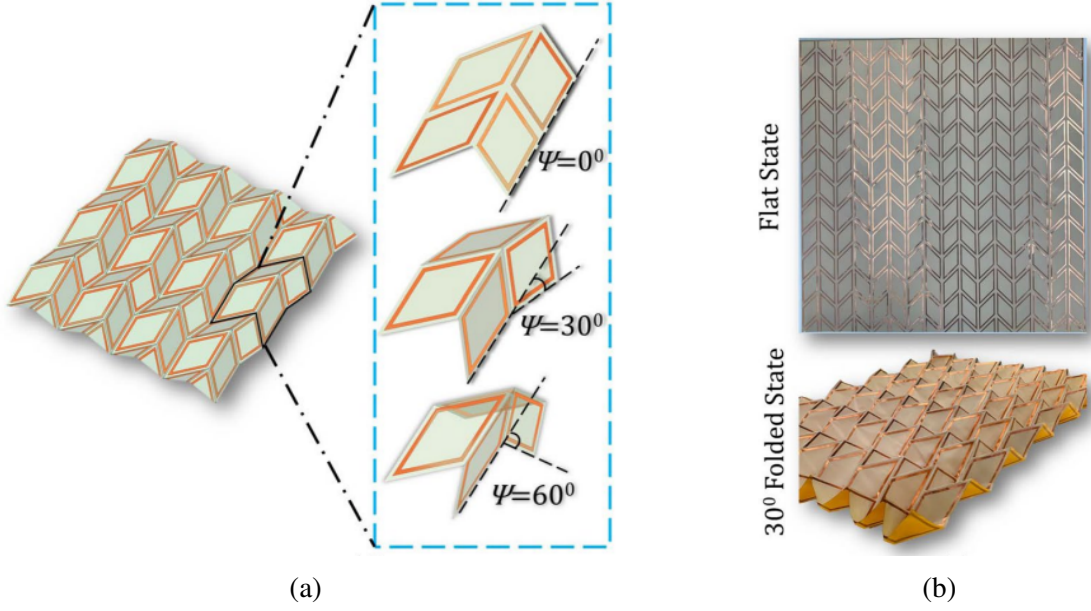


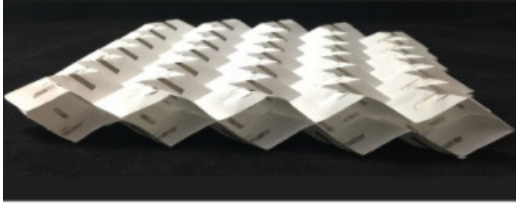
Figure 2.3: Miura-ori FSS with rhombic loop resonators: (a) a 4×3 configuration showing the unit cell at different folding states. [11], (b) fabricated FSS on a polyimide substrate [11].

uration, the bandwidth and frequency tunability can be significantly improved. [9] reported the 3-RiM configuration can demonstrate 100 % increasement in resonant frequency tunable range and 200 % increasement in bandwidth compared to a traditional 1-RiM design.

In 2020, [11] presents a Miura-ori FSS with rhombic loop elements (Fig. 2.3), where the resonate frequency of TE mode can be tuned by folding the structure and the TM mode has a stable frequency response. By conforming the strongly coupled rhombic loop resonators, this FSS can be transformed from a single-band to a dual-band configuration. These discoveries give the origami-inspired FSS designers more flexibility to meet a certain target performance.

2.1.2 Multi-layer Origami-inspired FSS

To further improve the bandwidth and angle of incidence stability, [12] presents a series of origami-inspired Miura-based FSS with multi-layer configurations. With “mirror-stacked” (Fig 2.4a) and “inline-stacked” (Fig 2.4b) configurations, the FSS can achieve different



(a)



(b)

Figure 2.4: Miura-ori-based FSSs with multilayer configurations: (a) “mirror-stacked”, (b) “inline-stacked”[12].

specifications such as multiple bands, broadband response, narrowband response, AoI rejection, etc, based on the application.

Manually operated mechanical frames are the most popular actuation method to reconfigure the origami-inspired FSSs. While a frame is good enough for proof-of-concept demonstrations, it is not practical for real-life implementations. [13] investigated a thermal actuation mechanism to deploy multi-layer origami-inspired FSS designs. Using heat sensitive paper as a spacer layer, the actuation can be controlled by varying the temperature, making the origami-inspired FSS more attractive for terrestrial, outer-space and electromagnetic cloaking applications.

2.2 Origami-inspired Antennas

To ensure the wireless devices can operate without interruption in different regions and environment conditions, the antenna must have the ability of switching the resonant frequency and radiation performance adaptively. Similar to the conventional tunable FSSs, most of the reconfigurable antennas were realized with active components such p-i-n diodes [14, 15], MEMS switches [16, 17], FETs [18] to turn part of the antenna on and off, or change the parasitic loading of the antenna. The active components with feeding or biasing circuits are adding extra power consumption, weight, cost and fabrication difficulty. Moreover, the rigid active components can be a bottleneck that limits the flexibility for wearable or conformal electronic devices. To address this challenge, origami-inspired antennas can be an

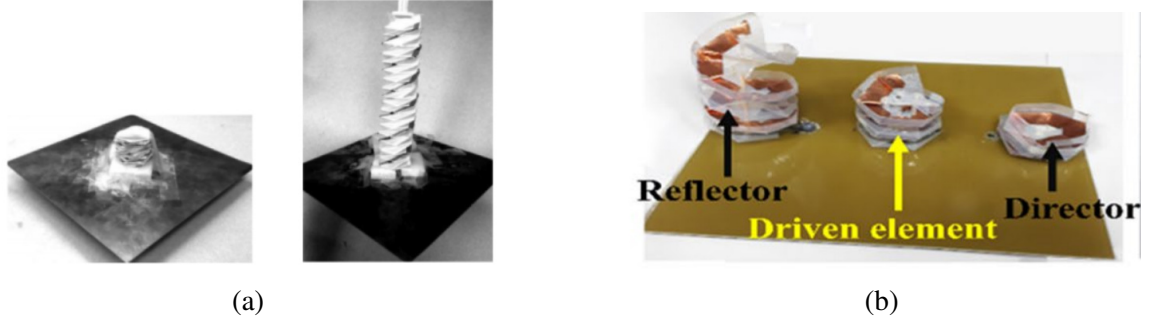


Figure 2.5: Origami-inspired helical antennas (a) a deployable helical antenna [19] (b) a tunable Quasi-Yagi antenna realized by three origami helical antennas [22].

excellent option because of their light weight, low cost, and ease of deployment. Various origami-inspired antennas have been studied over the years with promising performance, deployability, and reconfigurability.

2.2.1 Folded Origami-inspired Antennas

The most commonly used process to realize origami-inspired antennas is to use a flat paper as substrate, then attach a conductive layer using copper tape onto the substrate, finally, fold onto a 3D structure. [19, 20, 21] utilized this process to realize origami-inspired helical antennas (Fig. 2.5a) for satellite communication applications. The resonant frequency of the antenna can be easily tuned by varying the height of the structure. Additionally, the structure can be retracted to save space. The origami-inspired helical antenna can also be used as unit cell elements for other type of antennas. For example, by placing the origami antenna helical side-by-side [22], a tunable Quasi-Yagi antenna can be realized (Fig. 2.5b) with beam direction and beamwidth switching capability. [23] presented a bi-directional loop antenna array enabled by origami “magic cube” structure. The “magic cube” can be realized in both one-element and multi-element configurations. The volume can be minimized in folded configuration and the structure can be deployed to maximize the radiation performance, that can achieve realized gain of 5.91 dBi with three “magic cube” elements.

Origami-inspired structures can also transform an ordinary antenna into a high-performance

reconfigurable design. [24] uses the “Flasher” structure shown in Fig.2.6 to realize a tunable dipole antenna. This antenna covers 750 MHz to 800 MHz and 1.19 GHz to 1.26 GHz frequency bands with fractional bandwidth (FBW) of 6 % and 7 % respectively. [25] transformed a monopole antenna into a high-gain design utilizes “Tetrahedron” origami structure. The antenna covers 2 GHz to 4 GHz with 66 % FBW and realized peak gain of 9.5 dBi. This design can be very effective for point-to-point wireless communication systems. [26] presented a 2D to 3D convertible spiral antenna enabled by Nojoma wrapping origami structure. The antenna demonstrated wide frequency coverage from 2.1 GHz to 3.5 GHz with realized gain greater than 4 dBi.

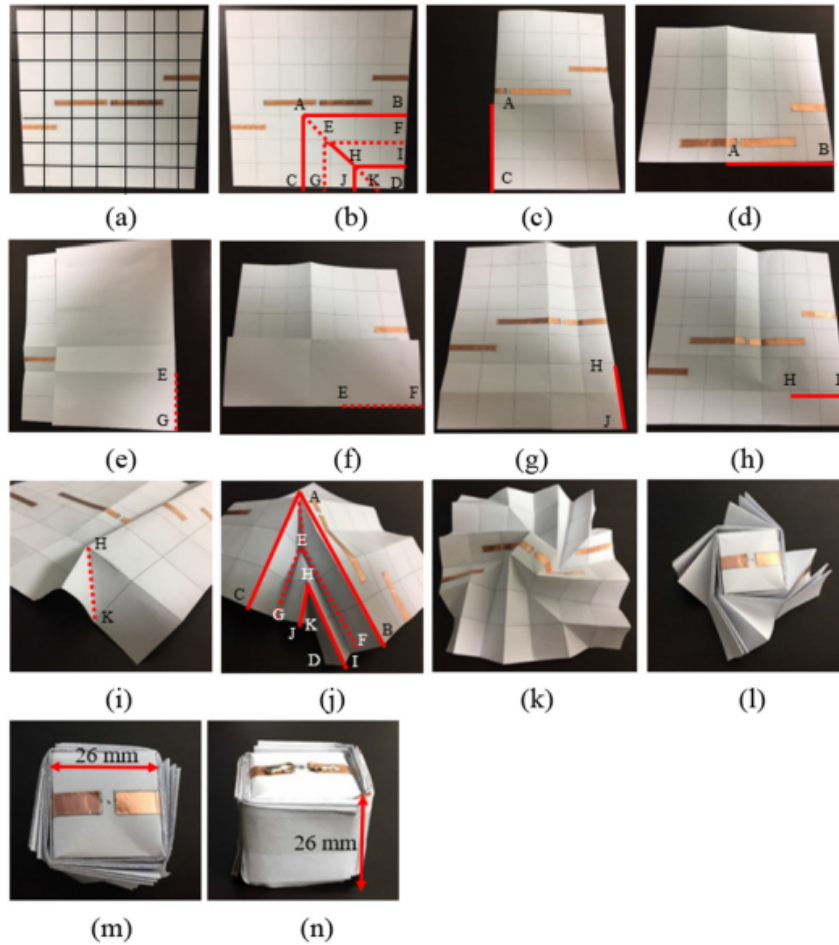


Figure 2.6: Origami “Flasher” antenna: (a)–(j) folding process, (k)–(n) transforming process from unfolded to folded states.

Folded origami-inspired antennas can also be realized on a standard PCB with cutted

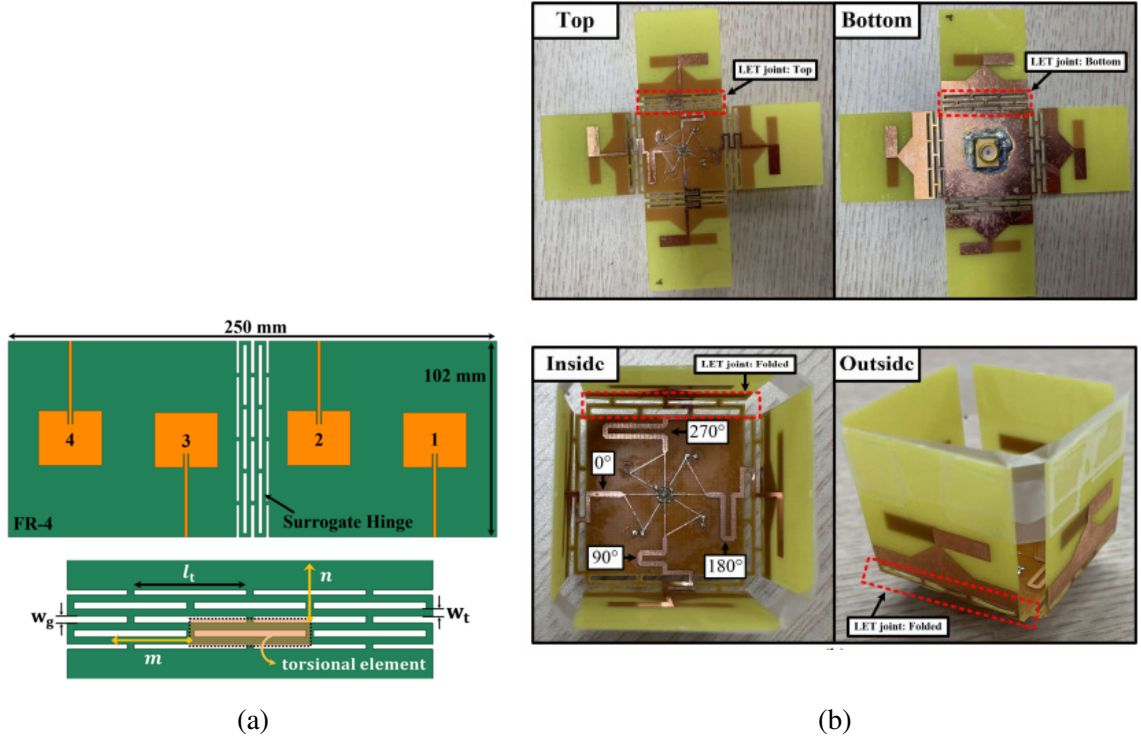


Figure 2.7: (a) Origami-inspired 4-element patch array with integrated hinge structures [27] (b) reconfigurable C-band dipole antenna array [28].

hinge structures. [27] presented one of the first origami antenna on a FR4 substrate with integrated hinges (Fig. 2.7a) that the hinge structure withstood 5000 folding cycles without any failures. The antenna has four patch elements with maximum gain of 9 dBi. By changing the folding angle, the main beam direction can be steered up to 35° . [28] presented a radiation pattern and shape reconfigurable C-band dipole array antenna for CubeSat applications. The design was fabricated with rigid FR4 board with Lamina Emergent Torsion (LET) joints to enable planar and folded modes. The planar mode is designed for linearly polarized omnidirectional inter-satellite communications, while the folded mode is designed for circularly polarized earth-to-satellite communications with high directivity.

2.2.2 3D Printed Origami-inspired Antennas

To realize origami-inspired antennas with more complicated structures, 3D printing technology can be an excellent solution especially with flexible or shape memory materi-

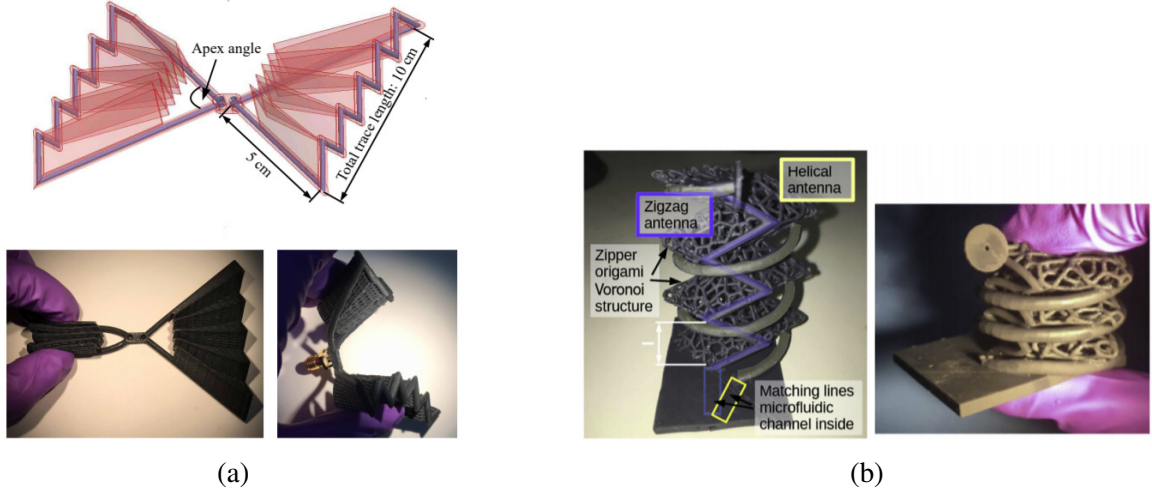


Figure 2.8: 3D printed microfluidics-based origami antennas (a) “Chinese-fan” inspired antenna [29], (b) origami reconfigurable antenna “trees” [30].

als. [29] proposes a 3D printed “Chinese fan” inspired origami antenna (Fig. 2.8a) with microfluidics-based liquid metal alloy (LMA). The resonant frequency can be tuned from 896 MHz to 992 MHz by changing the apex angle of the structure. [30] proposed an origami-inspired, 3D printed “tree” antenna system that contains zigzag and helical antennas. Both antennas are microfluidic-based and filled with EGaIn. The antenna features dual-band radiation in multiple polarization directions, and the radiation pattern can be re-configured by compressing or stretching the structure. These researches demonstrate the potential of using 3D printing technology to realize more complicated origami-inspired structures as well as using LMA to realize conductor traces with exceptional flexibility.

[31] presented one of the first 3D printed cube-shaped origami antenna utilizes shape memory polymers (SMP). With SMP, the structure can be deployed or retracted by simply changing the temperature, and the radiation pattern will be transformed from directional to omi-directional at the same time. This design is great for wireless energy harvesting applications. [32] presented a self-actuating 3D printed packaging-integrated antenna array with SMP. This design has four 28.8 GHz trapezoidal planar monopole antennas to achieve a wide bandwidth. It can be mounted on top of a Broadcom BCM2835 SoC, and begin deploying when the IC is heated to 62 °C.

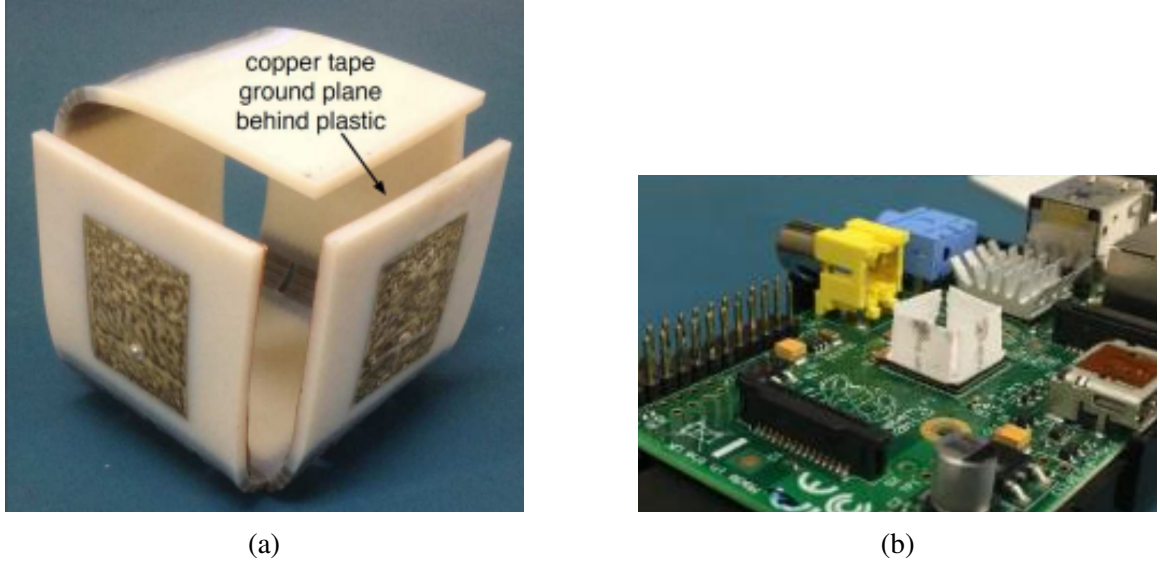


Figure 2.9: 3D printed SMP-based origami antennas (a) cube-shaped origami patched antenna [31], (b) packaging-integrated antenna array mounted on Broadcom BCM2835 SoC

2.3 Summary

Origami-inspired structure gives microwave components the ability of changing the frequency response and radiation performance on-demand, which can be an ideal solution for modern 5G and mm-wave applications. However, there are some challenges:

Lack of automated fabrication process that can utilize durable materials is one of the biggest challenges for origami-inspired designs as most of the designs are using paper as a substrate. While paper is ideal for realizing proof of concept origami-inspired structures, it is prone to absorb moisture, tear and features high dielectric losses. Moreover, paper-based origami RF structures need to be folded manually that limits their use in mm-wave applications when components become very small. For more complicated multilayer configurations, accuracy and durability suffered as the alignment and attachment of multiple substrates becomes a significant problem. For these reasons, it is important to develop a new fully automated process that utilizes durable and weather resistant materials to realize origami-inspired structures to fit the needs in real-life and future mm-wave applications.

Additionally, to date, there's no origami-inspired antenna that can reach mm-wave fre-

quency. This is because the small wavelength at higher frequencies dramatically reduces the feature size of the origami elements, making it challenging to design and fabricate.

Chapter 3 will provide a review of additive manufacturing (AM) technologies as well as additively manufactured RF devices. AM could be the key to solve the fabrication challenges of mm-wave origami-inspired microwave designs.

CHAPTER 3

REVIEW OF ADDITIVE MANUFACTURING TECHNIQUES AND ADDITIVELY MANUFACTURED RF DEVICES

Society is undergoing what is known as the fourth industrial revolution, also known as the digital revolution. While the era is often associated with computers, internet of things, and the world wide web, the fourth industrial revolution highlights the leaps in manufacturing technologies with the utilization of automation and smart machines. Within that domain, additive manufacturing (AM) technologies have seen rapid adoption, becoming accessible worldwide to rapidly prototype new designs and innovative structures that were not possible with traditional fabrication techniques [33, 34]. Additive manufacturing comes with additional benefits, such as reducing fabrication time, reducing waste materials, thereby reducing costs, as well as enabling integration of what would be traditionally fabricated from multiple parts into a single structure. The impact has been staggering, seeing adoption in multiple industries such as education, medical, space, aviation, etc [35, 36, 37, 38].

3.1 Overview of Various AM Technologies

AM can be divided into several categories. Two prominent additive techniques in printing circuit structures include aerosol jet printing and inkjet printing. These are 2.5D technologies which enable multi-layer printing capability that can print a wide variety of materials, including metals, dielectrics, and nano-materials onto both flexible and rigid surfaces with high resolution. While these technologies can deposit material in the x and y planar directions, the vertical height that can be printed (z-direction) is limited to a few millimetres to a few centimetres. The capabilities and limitations of inkjet and aerosol jet printing are listed in Table. 3.1.

Table 3.1: Capabilities and Limitations of Inkjet and Aerosol-jet Printing

Printing Technology	Advantages	Disadvantages
Aerosol Jet Printing	<ul style="list-style-type: none"> • High Print Resolution ($\sim 10\ \mu\text{m}$) [39] • Wide range of printable materials with a wide range of ink viscosity. • Conformal printing on curved surfaces • Nozzles using sheath gas protects nozzles from damage/clogging leading to reliable and repeatable printing 	<ul style="list-style-type: none"> • High Print Resolution leads to slow print time • Difficult to bring to manufacturing scalability due to nozzle cost • Higher operating cost due to additional necessary units to create droplet mist and focused carrier gas stream.[40]
Inkjet Printing	<ul style="list-style-type: none"> • Mature technology, wide range of manufacturers leading to low cost and high nozzle count for quick printing compared to aerosol • Low cost nozzles and adjustable printing densities for thin and thick film deposition • Roll-to-roll production capability for rapid high volume manufacturing[41] 	<ul style="list-style-type: none"> • Materials/inks are limited by its physical properties such as viscosity, surface tension • Limited nozzle lifetime due to clogging after periods of non-use. Nozzle cleaning procedures (purging, spitting) waste ink. • Generally lower resolution than aerosol. With some exceptions of low volume production/prototype systems that achieved sub-micron resolution [42]

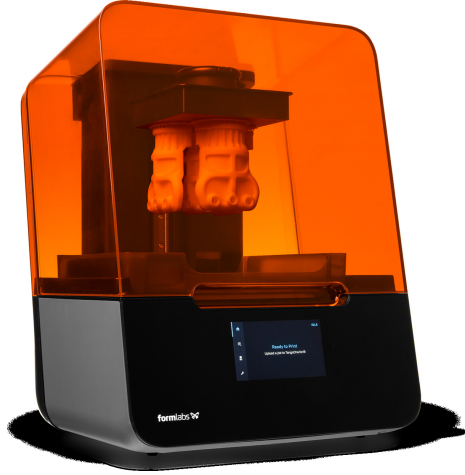
For true 3D structures, 3D printing technologies such as fused deposition modeling (FDM), Stereolithography (SLA), and Selective Laser Sintering (SLS) can be utilized to push the vertical dimension up to tens of centimetres. FDM is the most common type of 3D printing with a wide range of applications, which uses heated extruder to deposit thermoplastics and build up structure layer-by-layer, while SLA is an optical based 3D printing technology that uses laser or optical projectors as the energy source to cure and solidify light sensitive photopolymer resins layer-by-layer to realize complex 3D structures. The resolution is typically decided by the source optics, thereby making it a superior candidate for mm-wave applications. To date, commercialized SLA resins feature a wide variety of mechanical properties and RF characteristics. The availability of flexible elastomer resins makes SLA 3D printing technology an ideal solution for origami-inspired substrates. SLS uses high power laser to fuse the small particles of powder materials. The comparison between these 3D printing technologies is shown in Table. 3.2.

3.2 Additively Manufactured RF Devices

Additive manufacturing methods such as 3D printing and inkjet printing techniques are becoming increasingly popular in the fabrication of RF devices. A commercially available Formlabs Form3 SLA 3D printer is shown in Fig. 3.1a, and a Fujifilm Dimatix 2800 series inkjet printer is shown in Fig. 3.1b. Various types of RF designs have been realized with additive manufacturing process including antennas [43, 44], RFID sensors [45], system-on-chip (SoC) packaging [46], wireless energy harvesters [47], etc. Inkjet printed RF components have been demonstrated up to sub-terahertz frequencies on a variety of flexible substrates including Kepton, paper, liquid polymer crystal (LCP), and polyethylene terephthalate (PET). Inkjet printing technology can also be used to metallize or functionalize 3D printed substrates. This section provides a review of additively manufactured RF devices.

Table 3.2: Capabilities and Limitations of Various 3D Printing Technologies

Printing Technology	Advantages	Disadvantages
Fused Deposition Modeling (FDM)	<ul style="list-style-type: none"> • Low Cost and widely available • Wide range of available filaments for a variety of properties and applications such as flexible, conductive or thermal can be synthesized. [48] • Easy to swap to different extruder for multi-material printing [49] 	<ul style="list-style-type: none"> • High surface roughness requires post-processing, making it not suitable for high frequency mmWave applications [50] • Low resolution mainly limited by nozzle extruder dimensions. Typical nozzle is generally hundreds on microns meaning that the minimum feature size must be higher than the nozzle diameter [51] • Low thermal tolerances based on the nature of thermoplastics.
Stereolithography (SLA)	<ul style="list-style-type: none"> • High resolution, limited by the laser spot size [52], widely available and low cost • Low surface roughness on the order of 100s of nanometers, making surfaces excellent for printing conductive traces [53] • DLP or LCD based SLA exposes patterns in a single exposure allowing for quick fabrication. 	<ul style="list-style-type: none"> • Materials must be UV or light curable or able to be suspended in photopolymer resins, limiting the types of materials used • Cleaning and post-curing of SLA printed materials takes time.
Selective Laser Sintering (SLS)	<ul style="list-style-type: none"> • Lower material cost due to reusable powder materials • No support structure is required thus suitable for complex design • Fast production rate due to high power laser 	<ul style="list-style-type: none"> • Materials must be powder-based to be fused by high power laser, limiting the choices of materials • Higher surface roughness because of the use of powder materials



(a)



(b)

Figure 3.1: (a) Formlabs Form3 SLA 3D printing system [54] (b) Fujifilm Dimatix 2800 series inkjet printer [55].

3.2.1 Antennas

AM technologies such as inkjet printing allows direct deposition of conductive and dielectric materials onto various substrates and surfaces. A great number of miniaturized flexible antennas and antenna arrays have been demonstrate at mm-wave frequencies. [56] presented a fully inkjet printed 24.5 GHz Yagi-Uda antenna with multi-layer configuration (Fig. 3.2a). The antenna was realized on a LCP substrate with a novel microstrip-to-slotline transition structure enabled by inkjet printed SU-8 dielectrdic layer. The realized prototype demonstrated realized gain up to 8 dBi within the 24.5 GHz ISM band. [57] realized a fully inkjet printed 5-element beamforming antenna array at 90 GHz with realized gain of 11.3 dBi. This is the first demonstration of additively manufactured microwave component working at W-band. [58] presented a novel 3D printed Voronoi tessellated antenna (Fig. 3.2b), which cannot be manufactured in any other manner. The metallization of the antenna utilizes electroless copper plating to overcome the highly lossy nature of commonly used 3D printed dielectric materials.

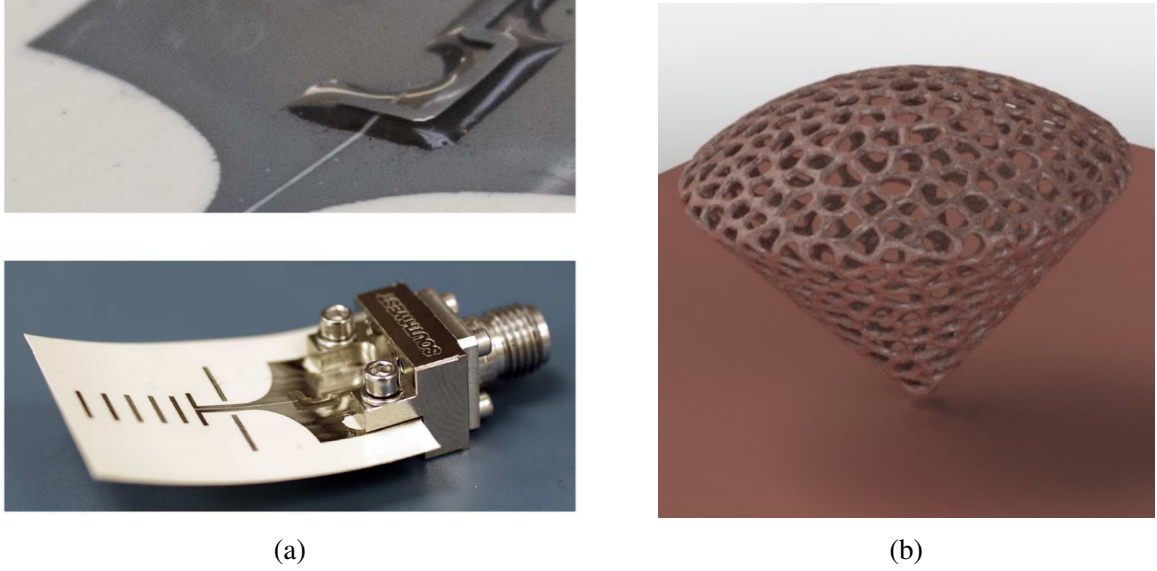


Figure 3.2: Additively manufactured antennas: (a) fully inkjet printed multi-layer Yagi-Uda antenna [56] (b) 3D printed Voronoi inverted feed dish antenna [58].

3.2.2 System on Packages/Antennas

The combination of 3D printing and inkjet printing technologies has great potential of introducing new and novel “smart” packaging designs that are difficult to implement using traditional technologies. Fig. 3.3 demonstrates a fully integrated 3D stacked module enabled by the combination of inkjet and 3D printing techniques. 3D printable low-loss polymer enables the realization of conformal substrates, through-package vias, smart encapsulates, microfluidic channels, as well as dielectric lenses. Inkjet printing technology can deposit conductive materials onto the 3D surfaces directly to realize interconnects, circuits, and EMI shielding layers. By combining various AM technologies, 3D integrated designs with more complicated structures and functionalities can be realized in mm-wave frequencies for both 5G and IoT modules.

Fig. 3.4a shows a completed System on Antenna (SoA) design [60] that has a customized 3D printed antenna excited by integrated MMIC and inkjet printed feeding lines. The SoA design is a combination of traditional SoC/SoP and 3D printed antennas, which can provide the high integration seen in SoC/SoP and high performance on-package anten-

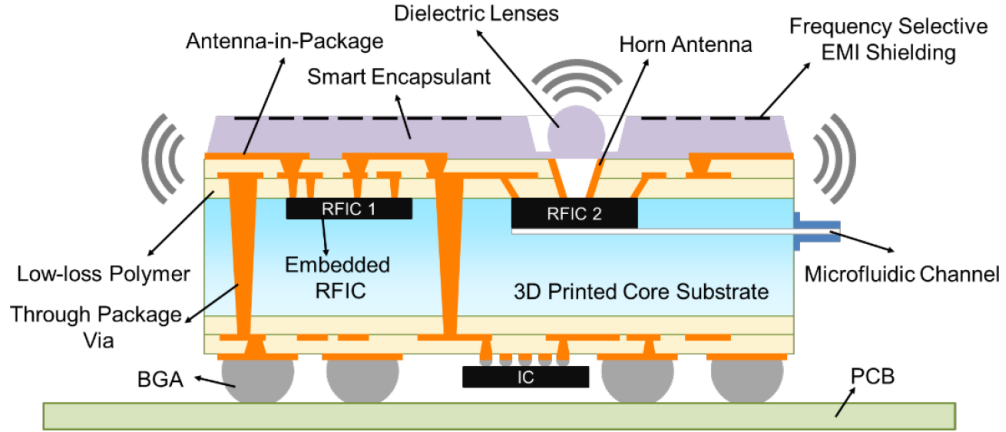


Figure 3.3: Schematic of a fully integrated 3D stacked module enabled by 3D printing and inkjet printing techniques [59].

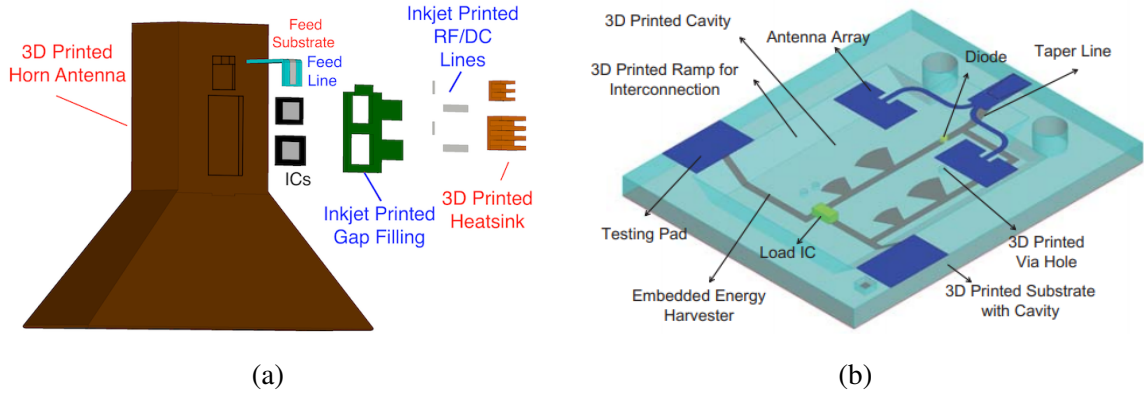


Figure 3.4: Additively manufactured SoA and SoP: (a) Exploded view of the of a SoA proof-of-concept topology, with the various components required [60]. (b) Flexible system demonstrated layer by layer [61].

nas in a low-cost fashion. By embedding the ICs and circuits within the antenna, the entire RF system can be integrated into one single structure, eliminating the need for flanges, coax transitions, and cables so that the system size and losses can be reduced dramatically. Complex system-on/in-package design shown in Fig. 3.4b with embedded energy harvester, loading circuits, and antenna arrays can be realized in a flexible fashion [61]. This design utilizes non-planar interconnects across integrated circuits of various heights as well as non-planar ramps for improved performance. The top of the structure contains inkjet printed on-package antenna that converts 5G mm-wave band from 24.4 GHz to 30.1 GHz.

The embedded energy harvester eliminates the requirements for external batteries or super capacitors by collecting energy from the nearby 5G base stations. The integration of this full system in a flexible package enables compact electronic devices that can be ideal candidates for the next stage of wearables where devices are integrated directly into the human body.

3.2.3 RFID Sensors

Flexible and wearable RFID sensors are a promising driver for the next generation on-body monitoring and testing solutions. Drop-on-demand (DOD) AM techniques such as inkjet printing can play a key role in reducing the fabrication cost of wireless RFID sensors with $10\times$ to $1000\times$ cost savings compared to traditional manufacturing processes. Various printed RFID sensors have been reported in recent years for numerous applications including temperature/humidity monitoring [62, 63, 64], haptic sensing [65], microfluidics [66, 67, 68], gas sensing [69, 70], etc.

[68] presented a fully inkjet printed chipless RFID tag with embedded microfluidic channels (Fig. 3.5a, Fig. 3.5b). Three spiral resonators with different sizes were designed to resonate at 3.4 GHz, 4.4 GHz, and 5.6 GHz. Microfluidic channels are placed in the spiral's gap between adjacent turns. By filling or removing the liquid in each channel, three resonate frequencies can be configured independently, so the RFID sensor can be "encoded" with 3-bit information. [64] demonstrated a fully inkjet printed smart agriculture RFID sensor on low-cost paper substrate (Fig. 3.5c). This sensor can detect soil moisture as well as leaf wetness and transmit the readings with integrated microcontroller and antenna. With inkjet printing process, the cost of the sensor has been kept remarkably low, eliminating the need to collect the densely deployed sensors over vast fields.

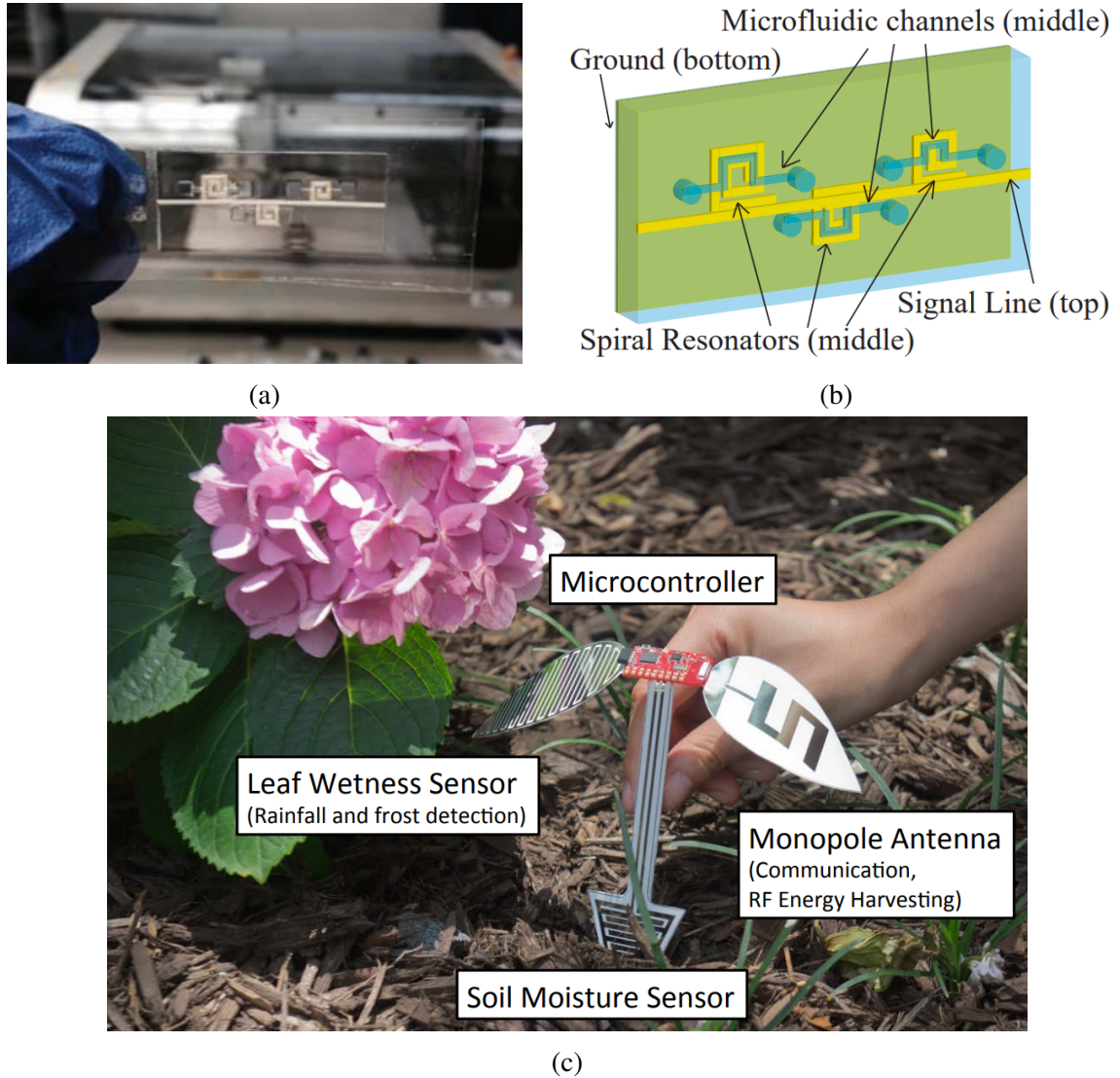


Figure 3.5: Additively manufactured RFID sensors: (a) A photo of an all-inkjet-printed microfluidic sensor[68]. (b) A 3D view of the printed microfluidic sensor [68]. (c) inkjet printed sensor platform for agriculture application [64].

3.3 Summary

High-resolution AM techniques not only reduce fabrication time and cost, but also enable the possibility of realizing novel RF design with irregular 2.5D/3D shape. Origami-inspired structures can potentially be fabricated automatically with high-precision 3D printed flexible substrate along with high-resolution inkjet printed conductive traces. However, it is challenging to combine 3D printing with inkjet printing process because 3D printed sub-

strates can demonstrate a relatively rough surface with periodic “hills” and “valleys” perpendicular to the printing plane. In addition, inkjet printed conductive traces need relatively high sintering temperature which can damage many 3D printed substrates. Placing the substrate at high temperature will dramatically reduce the substrates elasticity, causing the substrate to break after several folds. Thus, a process needs to be developed to metallize 3D printed flexible substrate in order to realize additively manufactured mm-wave devices.

The next chapter will present a newly developed “hybrid printing” process that successfully combines 3D printing and inkjet printing techniques to fabricate origami-inspired RF structures in exceptional accuracy. mm-Wave single-layer and multi-layer Miura-ori FSS as well as two novel wireless pressure sensors will serve as examples of this hybrid printing process.

CHAPTER 4

HYBRID PRINTING PROCESS

As discussed in Chapter 2, one of the biggest challenges with many origami-inspired designs is that they are utilizing paper as the substrate. While paper is ideal for realizing proof of concept demonstrations, it is prone to absorbing moisture, tearing, and has significant dielectric losses. Moreover, the fabrication process of paper based origami designs is usually labor intensive and can lack accuracy resulting from the manual cutting and folding. For these reasons, it is important to develop a new fully automated process that utilizes durable and weather resistant materials to realize origami-inspired structures to fit the needs in real-life and future mm-wave applications.

In this chapter, a new “hybrid printing” approach will be discussed that allows for the fabrication of origami inspired electronics by utilizing flexible 3D printing and multi-layer inkjet printing techniques. 3D printing allows the rapid design and fabrication of free-form three dimensional (3D) objects with ease. Fully 3D printed flexible substrates eliminate the requirement of folding and cutting and enables more complicated design elements such as slots, round holes, etc. Meanwhile, fully automated high-accuracy fabrication methodologies can reduce the unit size, opening the potential for 5G and mm-wave applications. Additive manufacturing technologies enable a wide degree of freedom for designers, allowing limitless shape designs and wide sets of material thickness, ideal for applications such as Miura-ori FSSs, absorbers, multi-layer FSSs, and curved FSS structures. Combining 3D printing with rapid and additive inkjet printing technique allows the deposition of a wide variety of materials, including metals, dielectrics, and nano-materials onto 3D printed non-flat surfaces with high resolution.

This chapter is organized as:

- The detailed procedure of hybrid printing process for shape-changing RF devices.

- Hybrid printed origami-inspired single-layer and multi-layer mm-wave Miura-ori FSSs.
- Hybrid printed pressure sensors.

4.1 Hybrid Printing Process For Shape-changing RF Devices

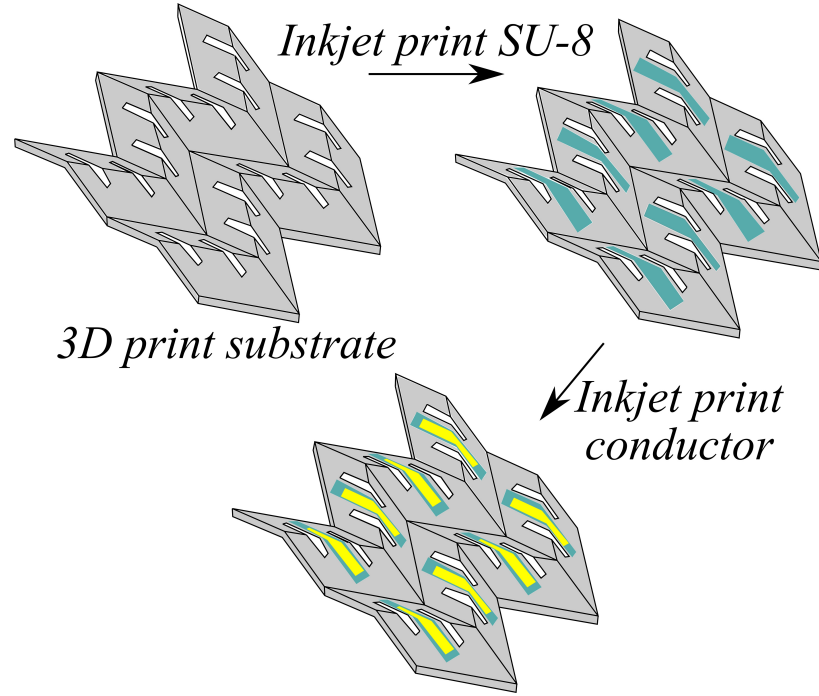


Figure 4.1: Schematic of the hybrid printing process to realize Miura-ori FSS.

The hybrid printing process contains three critical steps is shown in Fig. 4.1, which uses a single layer Miura-ori FSS as an example:

- 3D print dielectric substrate.
- Inkjet print a thin SU-8 buffer layer to smooth out the substrate surface and improve conductive layer adhesion.
- Inkjet print the conductive layers and sinter with a low temperature gradient process.

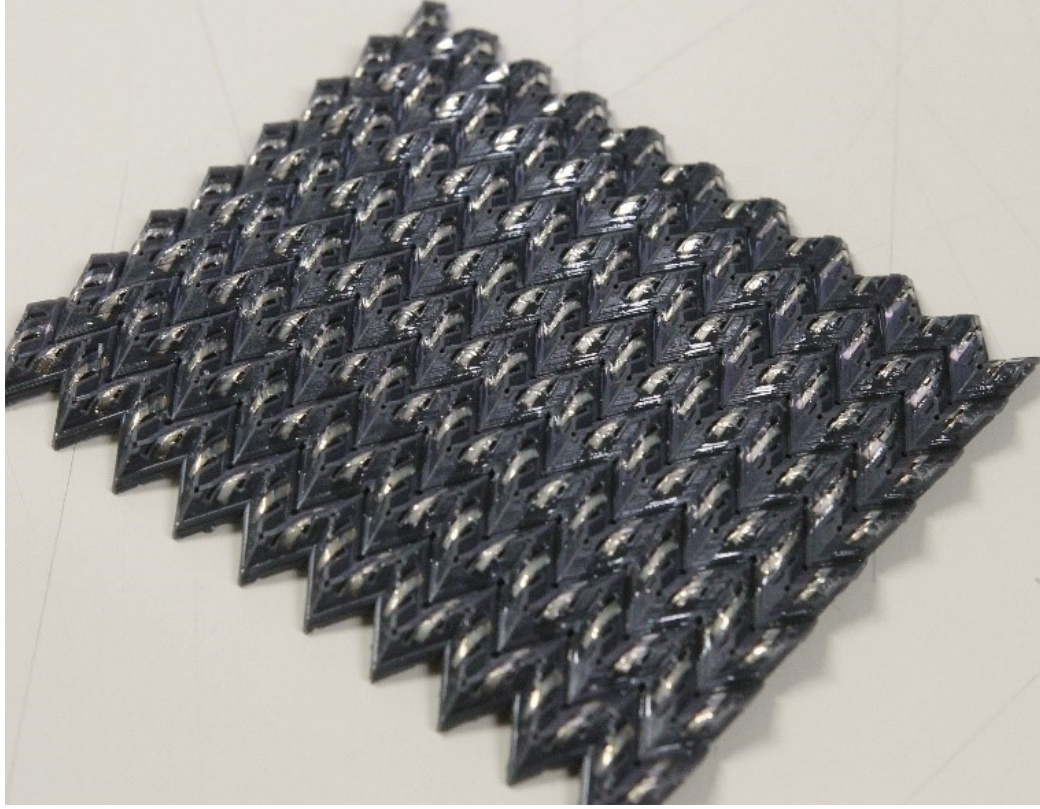


Figure 4.2: Prototype of the single layer hybrid printed tunable Miura-ori FSS.

4.1.1 3D Printed Dielectric Substrate

The substrate structure is printed from a Stereolithography (SLA) 3D printer with flexible materials. SLA is an optical based 3D printing technology that uses laser or optical projectors as the energy source to cure and solidify light sensitive photopolymer resins layer-by-layer to realize complex 3D structures. The resolution is typically limited by the source optics, thereby making it a superior candidate for mm-wave applications as compared to other 3D printing technologies such as Fused Deposition Modeling (FDM) [54]. To date, commercialized SLA resins feature a wide variety of mechanical properties and RF characteristics. The features of flexible elastomer resin make it an ideal origami substrate replacement for paper. The utilized material to fabricate the prototype shown in Fig. 4.2 is Formlabs Flexible (FLGR02) photopolymer. This flexible material is a “rubber-like” elastomer with tensile strength of 7.7 MPa to 8.5 MPa with 80 % elongation and 50 μm

maximum resolution [54]. The characterized dielectric constant at 22 GHz is 2.78 with loss tangent of 0.03.

The substrate is printed with 50 μm layer thickness, and post processed using Formlabs wash and cure system. The wash process uses isopropyl alcohol to remove the extra resin left on sample's surface. The curing system has 405 nm LED lights and a heater to ensure the best structure strength. The wash time used for Flexible resin is 15 min with 99 % isopropyl alcohol, while the cure time is 20 min at 60 $^{\circ}\text{C}$. With this wash-and-cure process, 3D printed substrates will have less chance of failure, smoother surfaces, more consistency, and less electromagnetic losses due to improved cross-linking due to simultaneous thermal and UV exposure curing.

4.1.2 Inkjet Printed Buffer Layers

With 50 μm high resolution 3D printing and optimized post processing, 3D printed substrates can demonstrate a relatively smooth surface, but compared to the 0.8 μm thickness of one layer of inkjet printed silver nanoparticle (SNP) conductor, the 3D printed substrate still has a relatively rough surface in both parallel and perpendicular directions to the print-

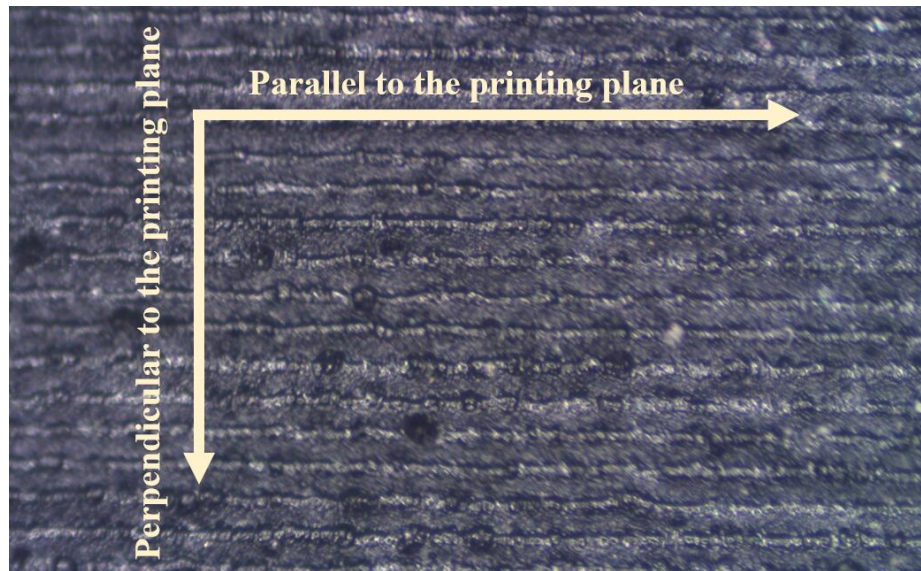
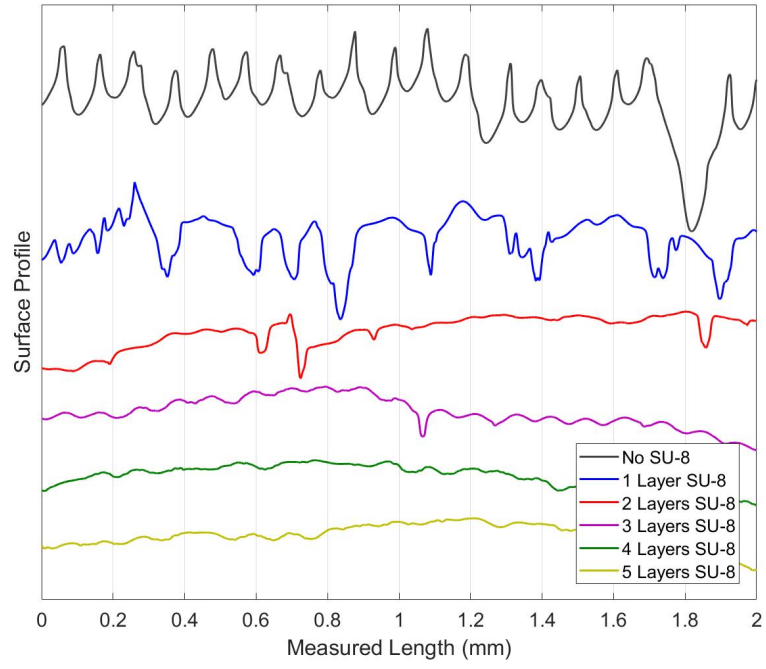
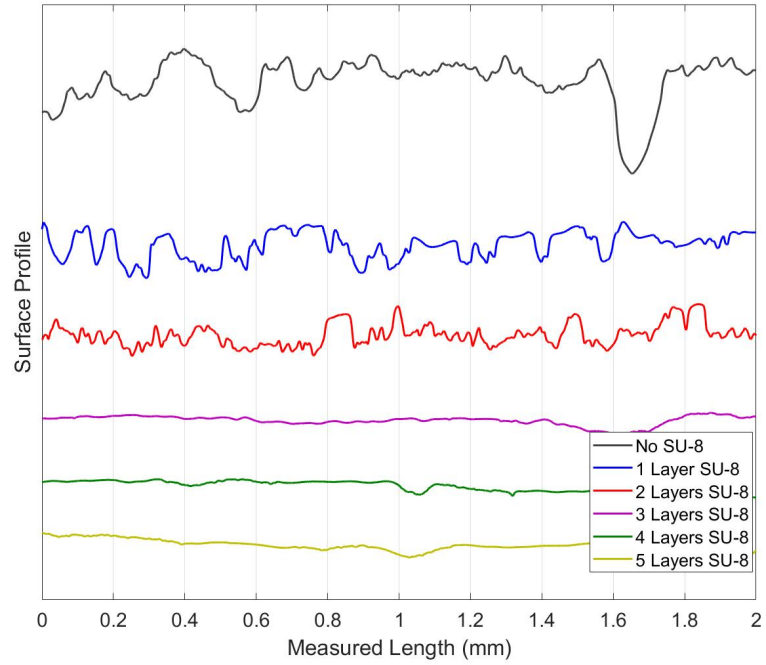


Figure 4.3: Directions of the surface respect to the printing plane.



(a)



(b)

Figure 4.4: Surface profile measurement results: (a)perpendicular to the printing line; (b) Surface profile parallel to the printing line.

Table 4.1:
Variance of the measured surface profile

	Perpendicular	Parallel
No SU-8	42.51 μm	26.54 μm
1 Layer SU-8	26.31 μm	8.12 μm
2 Layers SU-8	9.45 μm	3.24 μm
3 Layers SU-8	4.75 μm	0.78 μm
4 Layers SU-8	1.59 μm	0.66 μm
5 Layers SU-8	1.38 μm	0.49 μm

ing plane (Fig. 4.3 shows the directions of the surface respect to the printing plane). The surface roughness variation can get up to 42.51 μm in the perpendicular direction to the printing layers. Therefore, an inkjet printed SU-8 buffer layer is needed to reduce the surface roughness [71, 72]. In order to minimize the thickness of the SU-8 layer to maintain maximum substrate flexibility, a surface roughness test was performed using a KLA Tencor Alpha-step D-100 stylus profilometer. The measured surface profile with different layers of printed SU-8 in the direction that perpendicular to the 3D printing direction is shown in Fig. 4.4a; the measured surface profile parallel to the 3D printing plane is shown in Fig. 4.4b. From the surface profile measurement, without an SU-8 buffer layer, there are periodic “hills” and “valleys” perpendicular to the printing plane. This is because SLA 3D printer will cure the photoresist resin layer-by-layer, thereby forming periodic microstructures shown in Fig. 4.3. The numerical values of the measured surface roughness variation are shown in Table. 4.1. From the measurement results, the substrate surface roughness has been dramatically improved by printed SU-8 buffer layers. After 4 layers of inkjet printed SU-8, the surface will be smooth enough on both perpendicular and parallel directions, thus, 4 layers of MicroChem SU-8 will be utilized in this process.

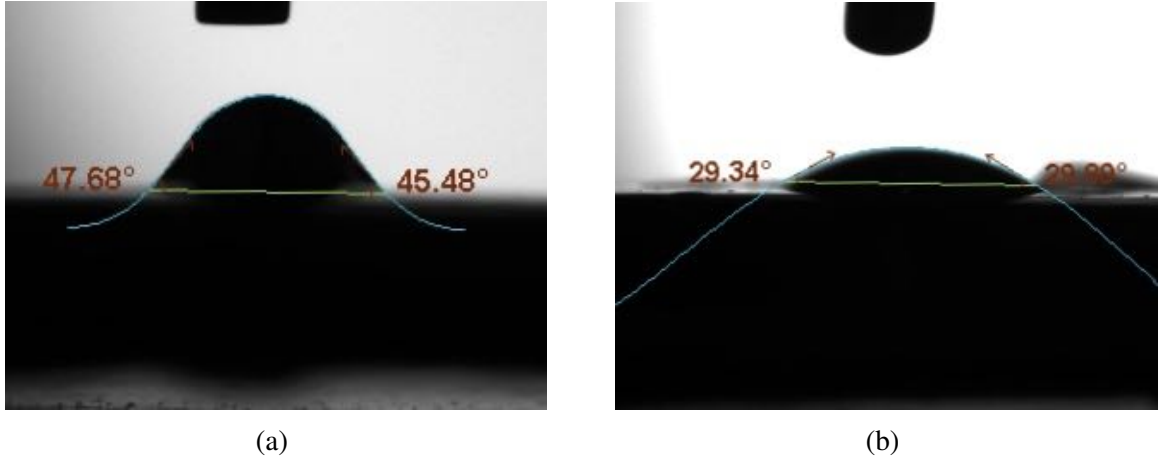


Figure 4.5: (a) Contact angle of silver nanoparticle ink before UV-Ozone treatment (b) contact angle of silver nanoparticle ink after UV-Ozone treatment.

4.1.3 Inkjet Printed Conductor Patterns

The conductor patterns can be inkjet printed with conductive inks such as SunChemical EMD5730 silver nanoparticle (SNP). The inkjet printer used to fabricate the prototype shown in Fig. 4.2 was Fujifilm Dimatix 2800 with 20 μm drop spacing (1270 dpi). Meanwhile, to improve the SNP ink wettability and adhesion without losing too much resolution, 90 s of ultraviolet (UV) ozone (O_3) treatment is adopted before printing the conductive SNP traces [73]. The contact angle of the silver nanoparticle ink on the smoothed SU-8 surface decreases from 46° to 29° as shown in Fig.4.5.

There are two challenges to print the conductors. Firstly, as the conductor is printed on a 3D substrate with a 2D pattern, the actual drop spacing density or drops per inch (DPI) will be compromised on 3D slopes. The reason is that fixed printing nozzles are usually parallel to a 2D flat substrate instead of a 3D substrate, meaning that the 2D pattern is projected onto the 3D shape. For a 3D substrate, the printing area is a ramp that is not parallel to the fixed printing nozzles. In this situation, the actual printed 3D trace is longer than the 2D length of the pattern, which will cause a DPI loss by a factor of $\sin(\theta)$ (θ is the angle between printing head and substrate). For example, the printed sample in Fig. 4.2 has a ramp with 35° maximum angle, so at least 20 % more layers are needed to compensate

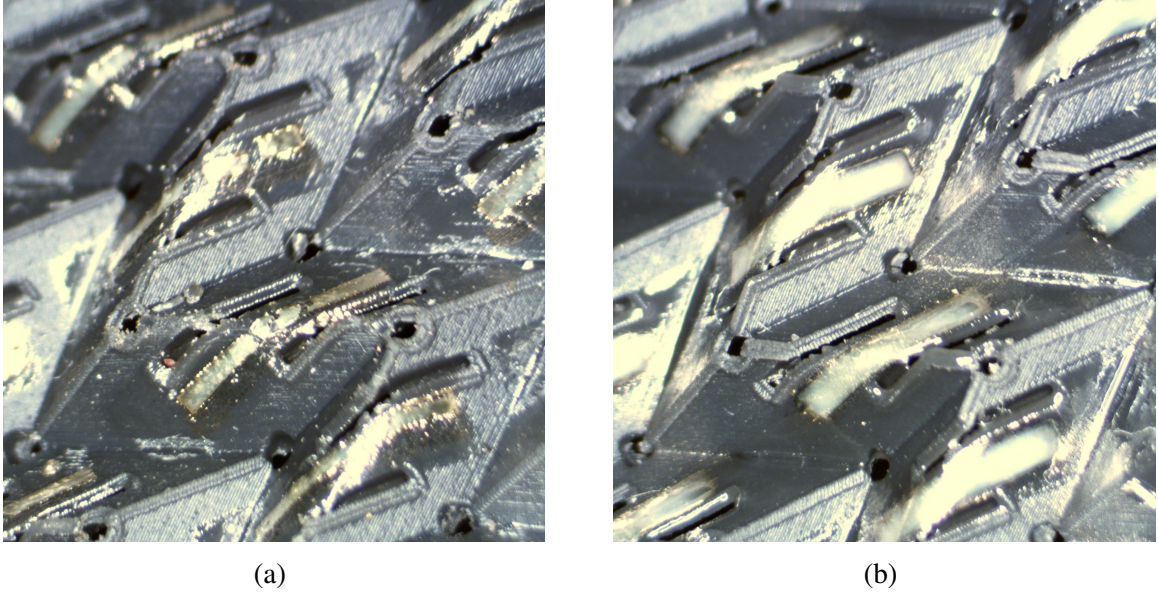


Figure 4.6: Comparison of sintering process: (a) high temperature sintering (b) low temperature gradient sintering.

the resolution losses. With a series of testing, 6 layers of silver printing is adopted for this design.

The second challenge is the fact that SNP inks need relatively high temperature sintering, typically above 180°C for the best conductivity and adhesion, but the high temperature often damages many 3D printed substrates. Placing the substrate at 150°C for 30 min will dramatically reduce the substrates elasticity, causing the substrate to break after several folds. Additionally, the substrate will shrink under high temperatures leading to cracks on metallic traces that create discontinuities (Fig. 4.6a). To solve this problem, a low temperature gradient sintering process is developed. After SNP printing, the sample was placed on a hot plate ramping from room temperature to 90°C with $150^{\circ}\text{C}/\text{h}$ temperature ramp, and hold at 90°C for 30 min to dry the pattern completely. Then, the temperature is increased from 90°C to 120°C with $150^{\circ}\text{C}/\text{h}$ ramp, and hold at 120°C for 30 min to sinter the pattern without breaking the substrate. Finally, the hot plate was turned off so as to let the sample slowly cool down to room temperature to avoid deformation caused by sudden temperature change.

With this low temperature gradient sintering process, the conductor quality is greatly improved and the realized conductor trace shows a conformal and smooth surface (Fig. 4.6b) on a curved 3D substrate. The measured sheet resistance using four-point probe test method is $0.02 \Omega/\text{sq}$ which is identical to the high temperature sintering results on a heat stabilized substrate.

4.2 Hybrid Printed Origami-inspired reconfigurable FSS

4.2.1 Single Layer Miura-ori FSS

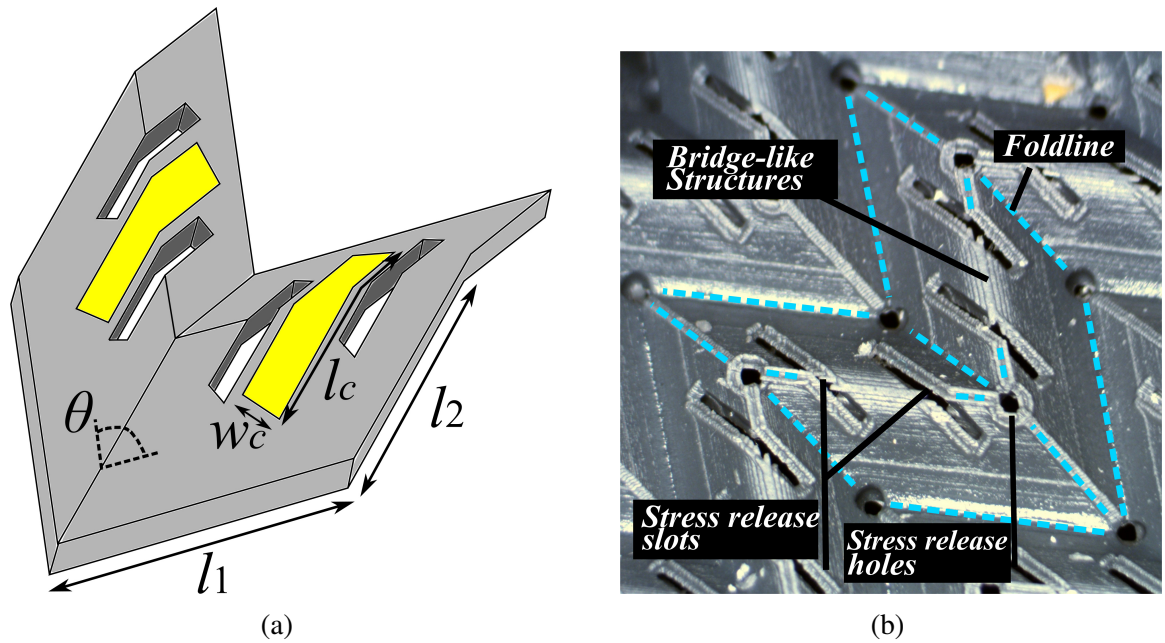


Figure 4.7: Single layer Miura-ori element: (a) an optimized Miura element with $l_1=5 \text{ mm}$, $l_2=7 \text{ mm}$, $\theta = 110^\circ$, $w_c=1 \text{ mm}$, $l_c=6 \text{ mm}$, substrate thickness= 0.8 mm ; (b) 3D printed Miura element with stress release structures.

Design

The design of a single layer Miura-ori FSS element is shown in Fig. 4.7a and Fig. 4.7b. The size of each element is reduced dramatically to $7 \text{ mm} \times 5 \text{ mm}$ compared to previous research [74] that uses a element with the size of approximately $20 \text{ mm} \times 20 \text{ mm}$. The reduced

size and thicker substrate make it especially challenging to produce a foldable Miura-ori FSS because the bending force applied on each foldline may break the substrate as well as the conductor traces. For example, the intersection of the foldlines will have stresses from three different directions applied on this single point; the substrate may break from this point during folding. In this design, a stress release hole (Fig. 4.7b) with 0.4 mm radius is introduced to each foldline intersection to release the applied stresses. However, even with optimized low temperature sintering process for the conductor traces, crack under strong bending stress may still occur. To enable more folding spaces, two slots are introduced by the edge of each conductor to form a “bridge-like” structure (Fig. 4.7b). The “bridge-like” structure can transform bending stress to rotating stress, which will improve the overall flexibility for each trace [74]. Moreover, every sharp edge on the bridge-like structures are smoothed to a 2mm radius round transition that will further increase the flexibility of the conductors. The designed folding range is from $\theta=110^\circ$ to $\theta=60^\circ$.

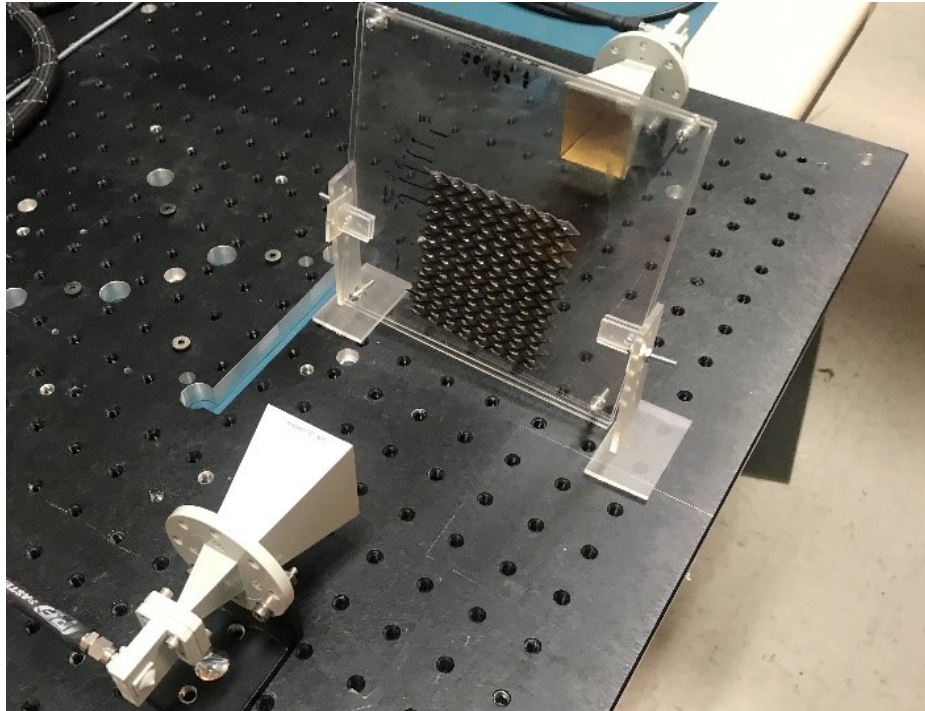


Figure 4.8: Measurement setup with frame and holder.

Simulation and Measurement

This Miura-ori FSS was designed and simulated in Ansys Electronics Desktop with HFSS design. The simulation setup uses master and slave boundaries along with Floquet port excitations. This environment will simulate the FSS as infinitely large but only needs one element, dramatically reducing the simulation time. The simulated results were verified on a bistatic measurement setup shown in Fig. 4.8. Two broadband horn antennas are placed in the line of sight to each other with the Miura FSS placed in the middle. A 3D printed frame and laser cut acrylic holder was made to compress and rotate the sample.

The simulated and measured insertion loss of the single layer Miura-ori FSS with respect to different angle of incidence (AoI) is shown in Fig. 4.9a. The -10 dB bandwidth increase significantly from 14 % to 29 % by the increased AoI from 0° to 60° . The bandwidth change is caused by increased equivalent circuit terminal resistance R_A with larger angles of incidence η , the function of R_A respect to η is shown in (4.1). Note that Z is the intrinsic impedance for 3D printed material, D_x , D_z is FSS element spacing along x and z axis, Δ_t is the transmitted power. As shown in (4.2), the reflection coefficient Γ will increase with R_A , which will boost the insertion loss that results in an improved percentage bandwidth [75].

$$R_A = \frac{Z}{2D_x D_z} \frac{\Delta_t^2}{\cos(\eta)} \sim \frac{1}{\cos(\eta)} \quad (4.1)$$

$$|\Gamma| = \left| \frac{-1}{1 + jX_A/R_A} \right| \quad (4.2)$$

The simulated and measured insertion loss of the Miura FSS for different folding angles ($\theta=110^\circ$, 90° , 80° , 60° are shown in Fig.4.9b. From this figure, it is clear that resonant frequency shifts higher as the folding angle decreases. The frequency shift is caused by reduced effective conductor length due to the folding. The measured frequency shift matches

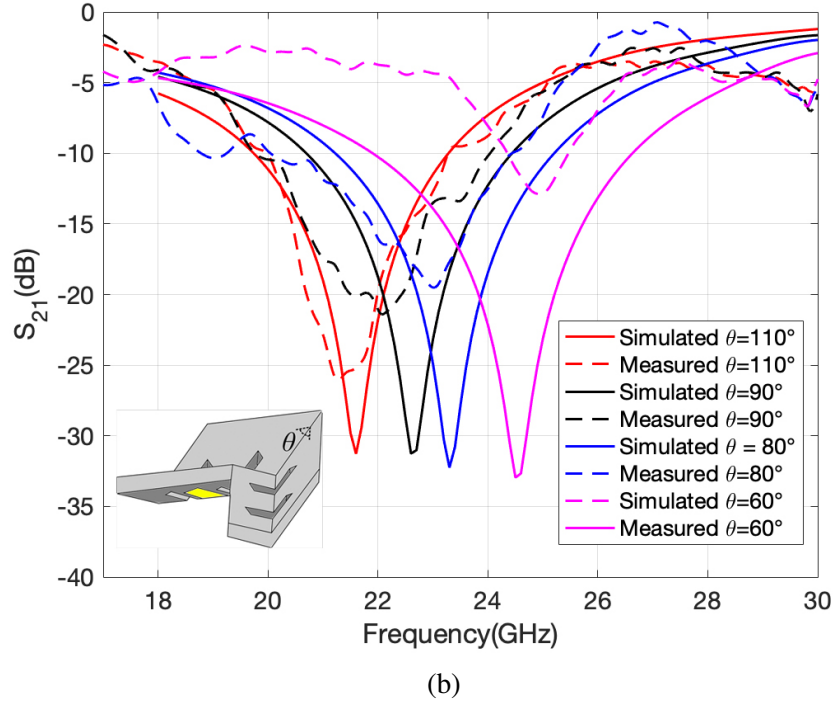
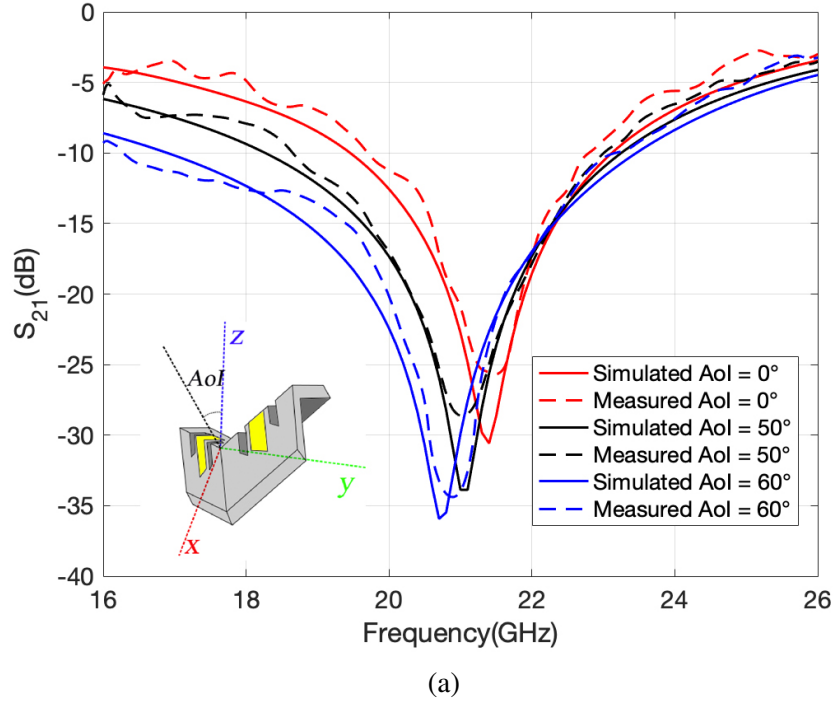


Figure 4.9: Simulation and measurement results: (a) frequency response of single layer M-FSS($\theta=110^\circ$) for different values of angle of incidence; (b) frequency response with different values of folding angle θ .

Table 4.2:
Equivalent inductance of the single layer Miura FSS

	Resonate Frequency	Inductance
$\theta=110^\circ$	21.6 GHz	2.71 nH
$\theta=90^\circ$	22.6 GHz	2.48 nH
$\theta=80^\circ$	23.3 GHz	2.33 nH
$\theta=60^\circ$	24.9 GHz	2.04 nH

closely to the simulated results, but the measured value of insertion loss decreases with smaller folding angles. This is because the simulation considers FSS as infinitely large, so unfolded 10×8 Miura FSS ($50 \text{ mm} \times 60 \text{ mm}$) will cover the whole antenna aperture which can be considered as infinity large. Nevertheless, the size of folded 10×8 Miura FSS will reduce to $50 \text{ mm} \times 7 \text{ mm}$ ($\theta=60^\circ$) which cannot cover the entire illuminating antenna beamwidth anymore. The finite FSS introduces edge currents which lead to leakage that reduces insertion loss [76]. The tested 10×8 Miura FSS substrate is the largest printable size for the utilized 3D printer.

Equivalent Circuit

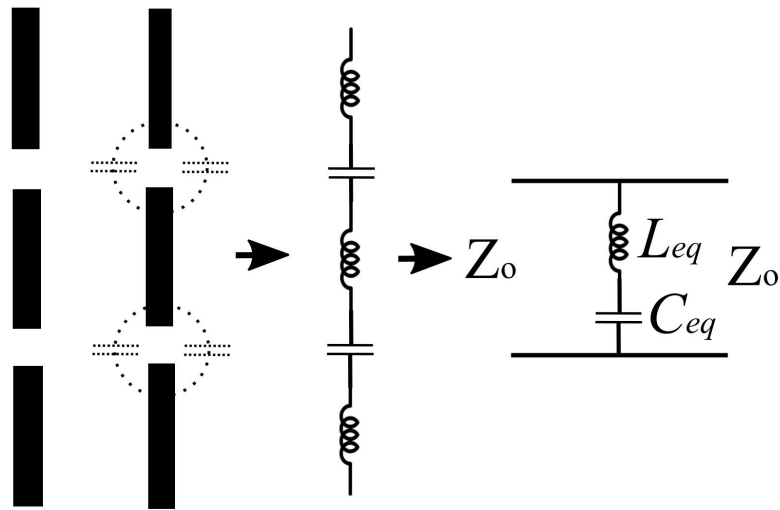


Figure 4.10: Equivalent circuit of the FSS.

In the periodic dipole array FSS, the conductive elements are inductors while the gaps are associated with the series capacitors [75]. So the Miura FSS can be equivalent to a series LC circuit as shown in Fig. 4.10. When the Miura FSS is compressed, the length of the effective conductor will decrease, thus cause the inductance change. The inductance can be calculated by (4.3). The inductance value respect to the folding angle is shown in Table. 4.2, the values are derived and verified in Keysight Advanced Design System (ADS) 2017.

$$L_{eq} = \frac{1}{C_{eq}(2\pi f)^2} \quad (4.3)$$

4.2.2 Multi-layer Miura FSS

Previously reported single-layer origami-inspired FSSs under 15 GHz have shown a very good frequency range tunability and S_{21} performance [12]. However, at higher mm-wave frequencies, the physical size of the FSS structure will be dramatically reduced due to the much shorter wavelength. For example, the size of a 30 GHz unit cell will be 75 % smaller compared to that of a 15 GHz unit cell. The mm-wave single-layer origami FSS discussed in the previous subsection has shown a significant performance degradation when measuring the folded sample. This is because the effective area of the folded mm-wave sample with smaller size can not cover the entire beamwidth of the excitation antennas during the measurement, thus leading to leakage that reduces the insertion loss.

Additionally, single-layer FSS structures have drawbacks of poor selectivity and narrow bandwidth. Thus, this paper introduces multi-layer Miura-ori FSS configurations. Multi-layer configurations have more tunability and better bandwidth performance. While previous research on multi-layer Miura FSS is based on paper [12], to connect two piece of papers together, it requires manual alignment that will reduces accuracy. Further more, multi-layer Miura-ori FSS adds more stress to the fold line, paper-based two piece substrates can easily break or misalign from the connecting point. 3D printed multi-layer

Miura FSS can be made with a one piece substrate utilizes durable and flexible material. Combining with inkjet printing technique, 3D printed multi-layer Miura FSS has more potential applications such as ultra-wideband design, microfluidic implementation, multi-frequency, etc.

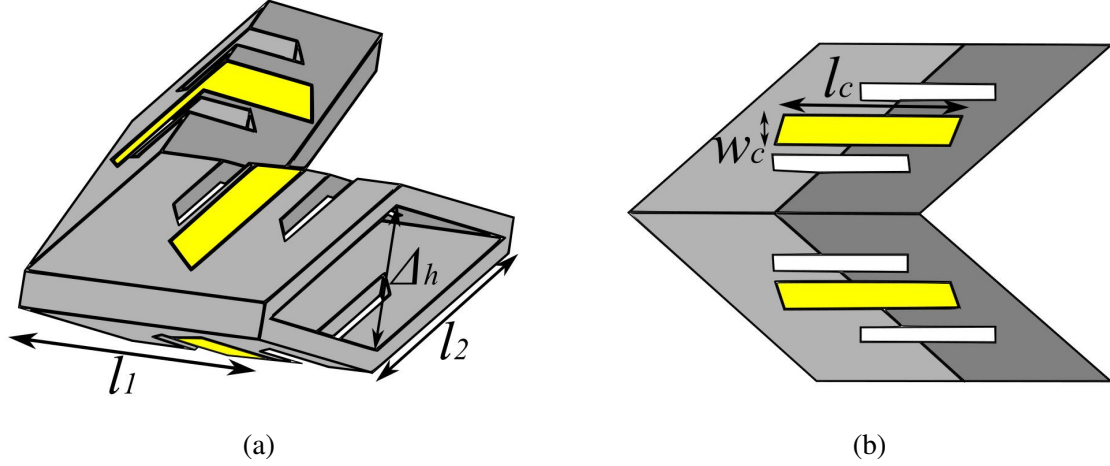


Figure 4.11: Multi-layer Miura-ori element: (a) a mirror stacked Miura unit with $l_1=5$ mm, $l_2=7$ mm, $\theta = 110^\circ$, $w_c=1$ mm, $l_c=6$ mm, substrate thickness=0.7 mm; (b) 3D printed Miura unit with stress release design.

Design

To improve the performance of origami-based FSS at mm-wave frequencies, we can take the advantages of the hybrid printing process to realize a novel mirror-stacked multi-layer Miura-ori FSS design. The element design shown in Fig. 4.11a consists of a single piece 3D printed substrate with two Miura sheets being stacked, and dipole conductive traces on both top and bottom. The multi-layer configuration doubles the density of the conductive elements, resulting in a larger effective area that improves the insertion loss performance over single-layer designs. The element is designed to take full advantage of 3D printing technology which enables more complicated design elements such as slots, holes, hollows, etc. The stress release slots shown in Fig. 4.11b form a “bridge-like” structure that reduces the bending stress applied to the conductors when folding the substrate. The stress release

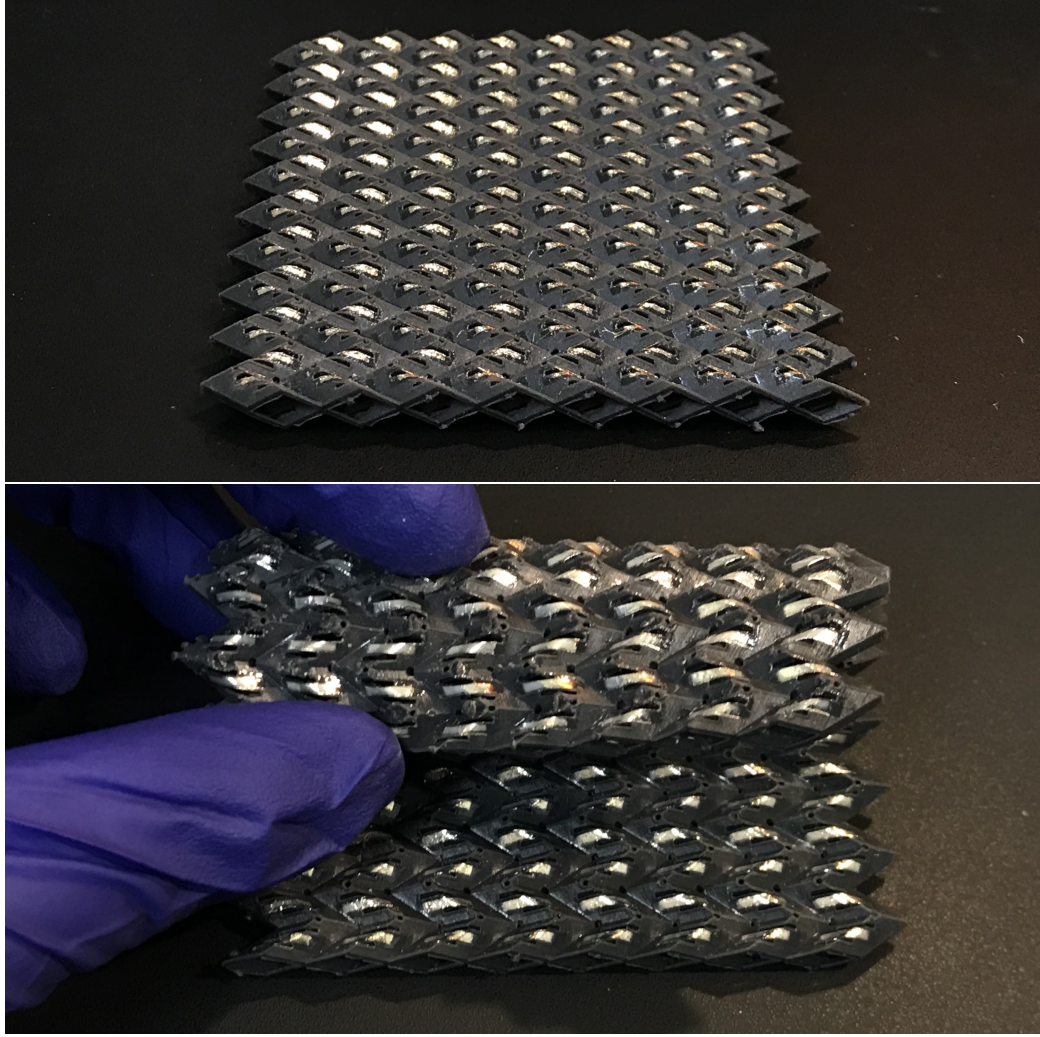


Figure 4.12: Fabricated mirror-stack multi-layer M-FSS.

holes with 0.4 mm radius reduce the mechanical stress on the intersection of foldlines. This multi-layer design has same 7 mm \times 5 mm size as the single layer counterpart, but has a thinner 0.7 mm substrate to improve the flexibility. The fabricated 10 \times 8 prototype is shown in Fig. 4.12. SLA 3D printing technology enables the fabrication of complex substrate structures in high precision. The conductive traces kept enhanced alignment during folding because the interlayer alignment being dramatically improved compared to previous work [12].

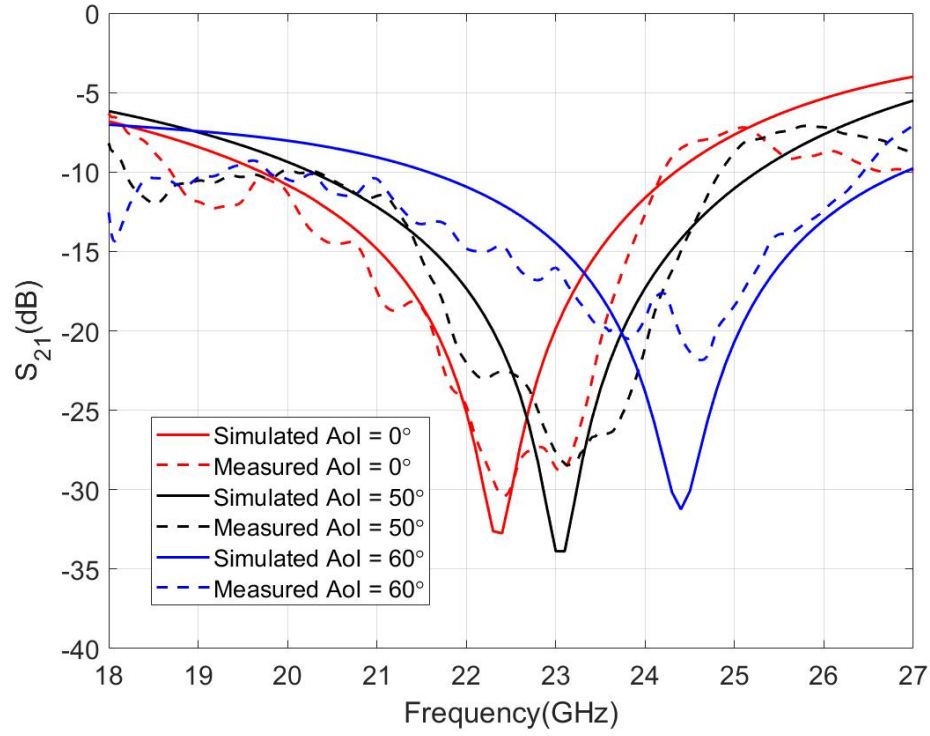


Figure 4.13: Frequency response of multi-layer M-FSS($\theta=110^\circ$) for different values of angle of incidence .

Simulation and Measurement

The multi-layer prototype was simulated and measured with the same set up used in single layer design. The simulated and measured insertion loss with respect to different angle of incidence (AoI) is shown in Fig. 4.13. The multi-layer Miura FSS has a multiple-resonance behaviour due to the stacked structure to realize a much broader bandwidth with up to 47 % increasement. The bandwidth can be further tuned by changing the AoI (Table. 4.3). However, the interlayer distance Δh in the mirror configuration will change with AoI, which can lead to a poor interlayer coupling at higher values of AoI, so we get unstable AoI rejection in Fig. 4.13 above 50° .

The simulated and measured frequency response of the mirror-stacked multi-layer FSS for different folding angles θ are shown in Fig. 4.14. The resonant frequency can be tuned from 22.4 GHz to 26.1 GHz by changing the folding angle θ from 110° to 60° . The

Table 4.3:
Bandwidth Comparison Between Single and Multi-layer M-FSS

	Single Layer BW	Multi-layer BW
AoI=0°	13.9 %	19.5 %
AoI=50°	19.0 %	22.8 %
AoI=60°	28.8 %	33.9 %

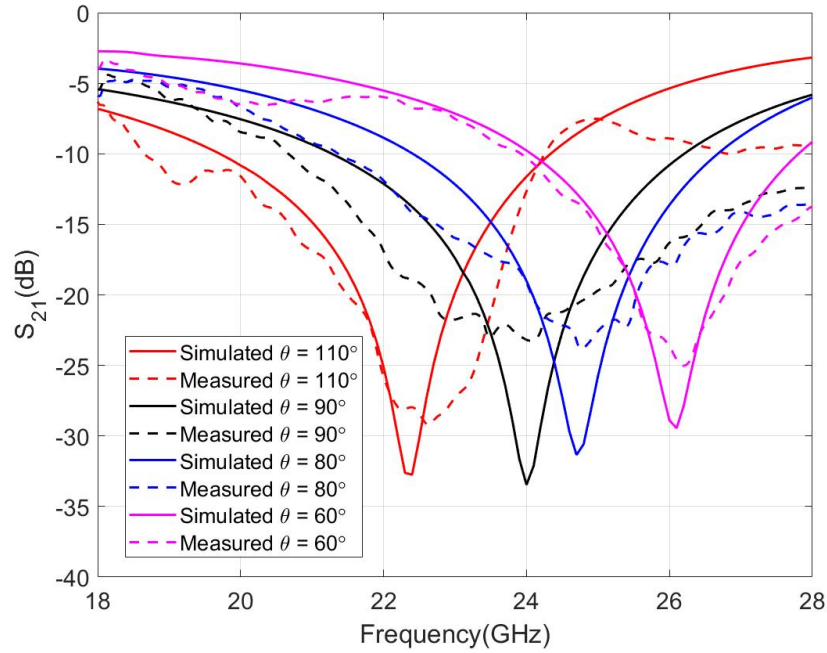


Figure 4.14: Frequency response with different values of folding angle θ .

frequency shift is caused by the reduced equivalent conductor length during folding, which in turn increases the resonant frequency. A performance comparison between multi-layer and single-layer mm-wave Miura FSS is shown in Table 4.4. The multi-layer configurations shows up to 12 dB better insertion loss performance, especially for lower θ values, and wider frequency tunable range thanks to the improved conductor density.

4.3 Hybrid Printed Pressure Sensors

Wireless sensor network (WSN) is an emerging technology that utilizes wirelessly connected sensor nodes to collect and monitor the surrounding environment. One of the key

Table 4.4:
Insertion Loss Performance Comparison Between Single-layer and Multi-layer Designs.

	Single Layer	Multi-layer
$S_{21}:\theta=110^\circ$	-25 dB	-28 dB
$S_{21}:\theta=90^\circ$	-22 dB	-23 dB
$S_{21}:\theta=80^\circ$	-25 dB	-28 dB
$S_{21}:\theta=60^\circ$	-13 dB	-25 dB
Tunable Range	11.7 %	15.7 %

challenges of realizing WSN is the lack of sustainable power supplies to enable consistent data readings over a long period of time without maintenance [77]. A promising solution is to use passive sensors along with chipless radio frequency identification (RFID) technologies to eliminate the need for a power source. Chipless RFID can be realized with multiple resonators, microfluidic channels, variant modulations, etc. However, it is challenging to design passive sensors especially pressure sensors that can cooperate with chipless RFID transmitters.

Pressure sensor plays an essential role in detecting force, strain, and displacement. Among various sensors, conventional pressure sensors use capacitors or piezoelectric that requires biasing and modulation circuits with a power source. Flexible passive RFID sensors enabled by the hybrid printing process can relate real-world physical properties such as force, strain, pressure, and displacement to resonant frequency shifts, realizing a simplified, lower cost, and more robust design.

4.3.1 Hybrid Printed Planar Pressure Sensor Using Metamaterial Absorber

Fig. 4.15 shows the design of the hybrid printed planar pressure sensor enabled by a metamaterial absorber. The one-piece 3D printed flexible substrate has a “sandwich” structure with a planar sensing area on top, a ground plane on the bottom, and a series of tunable hinge structures in the middle. The planar sensing area consists of an array of inkjet-printed metamaterial waveguide elements sitting on inkjet-printed SU-8 dielectric buffer

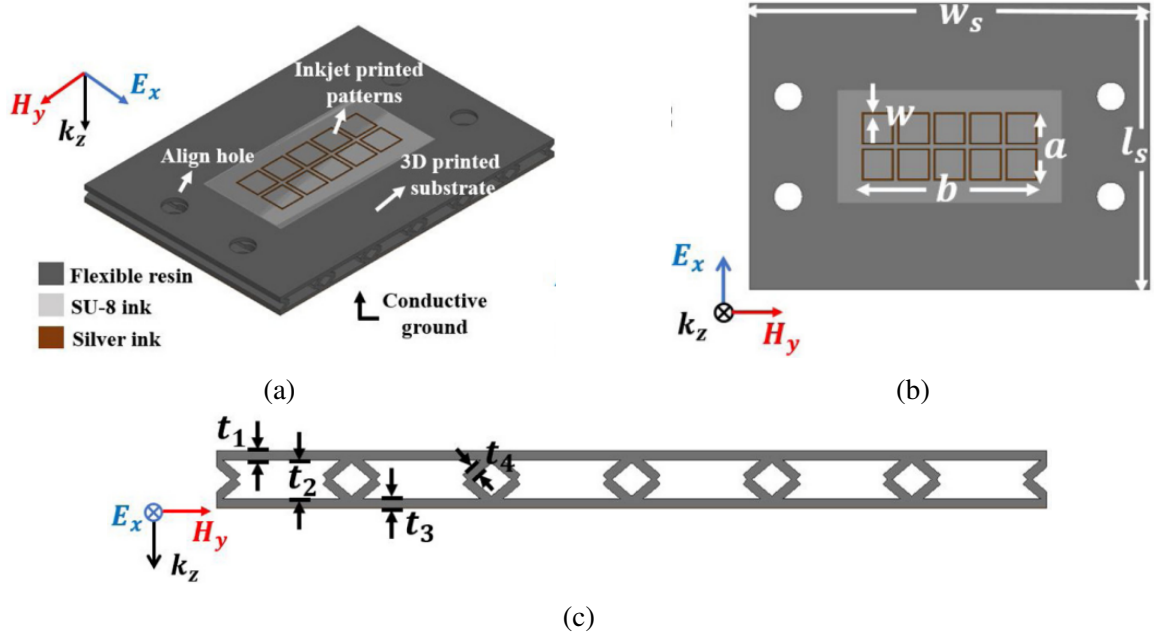


Figure 4.15: Design of the hybrid printed metamaterial-enabled pressure sensor: (a) perspective view; (b) top view; (c) side view.

layer. When applying pressure on top of the sensing area, the origami-inspired hinge will deform, changing the metamaterial waveguide's height and shifting the resonate frequency.

The mechanical performance of this sensor was simulated in COMSOL Multiphysics by applying forces on top of the metamaterial structure. The material properties were set as 5.6 MPa Youngs modulus and 0.45 Poissons ratio. As shown in Fig. 4.16, 45 N compressive force is required in this design to increase the compression length from 0 mm to 1 mm. The electromagnetic performance of the sensor was simulated in ANSYS HFSS and measured with INSTRON 5569 compression electromechanical device. The simulated and measured reflection coefficient is shown in Fig. 4.17. In the initial state, the pressure sensor resonates at 5.2 GHz with a 16 dB reflection coefficient. When the height was varied from 5.9 mm to 6.5 mm, the resonant frequency increased from 5.20 GHz to 5.66 GHz, resulting in a 20 MHz/N sensitivity.

This pressure sensor can be used as passive nodes in WSN and get the readings by measuring the reflected signal. The size of the sensor is expandable (ideally to infinitesize) to be deployed in a larger area. In addition, by tuning the thickness of the origami-inspired

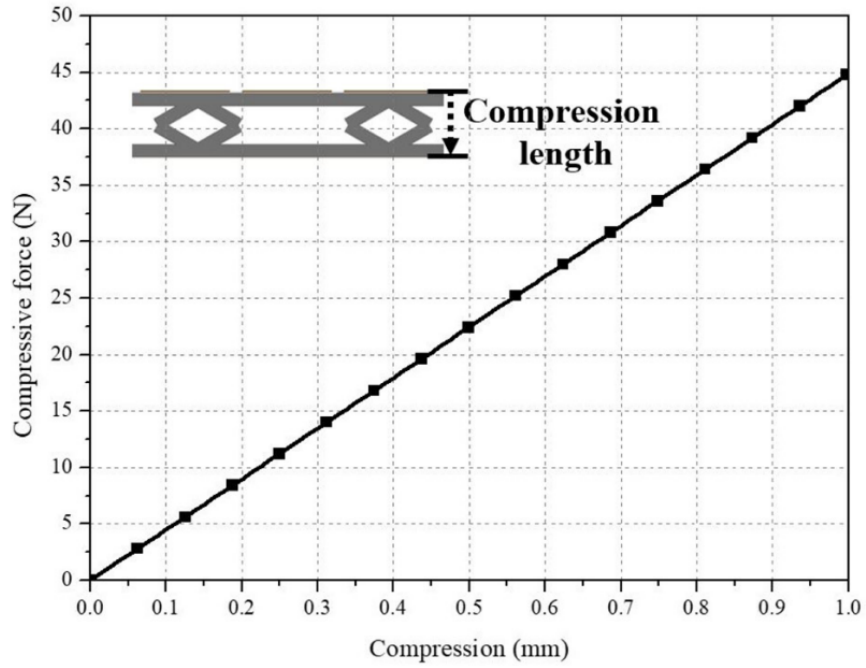


Figure 4.16: COMSOL simulation results of the hybrid printed metamaterial-enabled pressure sensor.

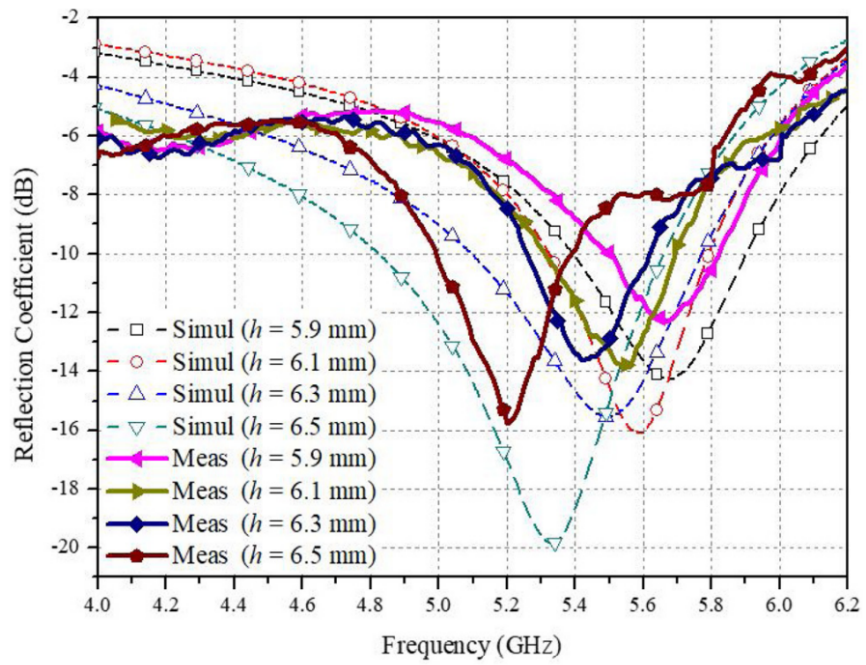


Figure 4.17: Simulated and measured frequency response of the hybrid printed metamaterial-enabled pressure sensor.

hinge structure, the stiffness of the sensor can be changed. Thus, the sensor sensitivity can be easily tuned to fulfill the needs for more application scenarios.

4.3.2 Hybrid Printed Planar Pressure Sensor Using Substrate Integrated Waveguide (SIW) Technology

The hybrid printed metamaterial-based planar pressure sensor has shown excellent sensitivity for large area pressure sensing applications. However, it is challenging for metamaterial-based structures to be miniaturized for small area pressure sensing. Therefore, a substrate integrated waveguide (SIW)-based pressure sensor for small contact area applications is designed. The schematic and fabricated sample of the pressure sensor is shown in Fig. 4.18. It consists of inkjet-printed conductive SIW cavity pattern and a 3D printed flexible substrate. At the center of the substrate, there is a cylindrical cavity which is filled with a 3D printed mesh structure to tune the stiffness of the cavity. When pressure is applied on top of the SIW cavity resonator, the 3D printed mesh structure compresses resulting in a change in effective permittivity and resonant frequency of the SIW cavity resonator.

The structure was simulated in COMSOL Multiphysics to evaluate the mechanical performances. With added 0 kPa to 2.4 kPa pressure, the height change increased from 0 mm to 1.52 mm. The measurement result is shown in Fig. 4.19. As the height change increased from 0.29 mm to 1.5 mm, the resonant shifted from 4.21 GHz to 3.79 GHz, respectively, resulting in a sensitivity of 244 MHz/kPa. The results showed good linearity and sensitivity for a passive pressure sensor design with good frequency response stability over 100 repeats. By changing the density of the mesh structure, the stiffness and sensitivity of sensor can be easily tuned based on the actual need. Along with the metamaterial-based design, the hybrid printed pressure sensor can find their applicable scenarios for both large area and small area pressure/strain sensing applications.

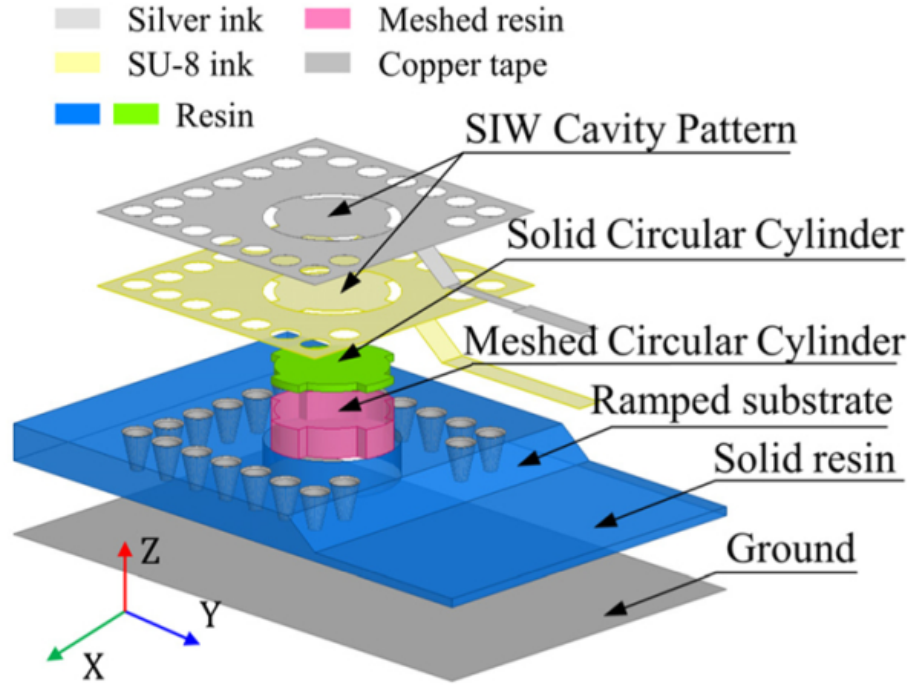


Figure 4.18: Design of the hybrid printed SIW cavity pressure sensor in perspective view.

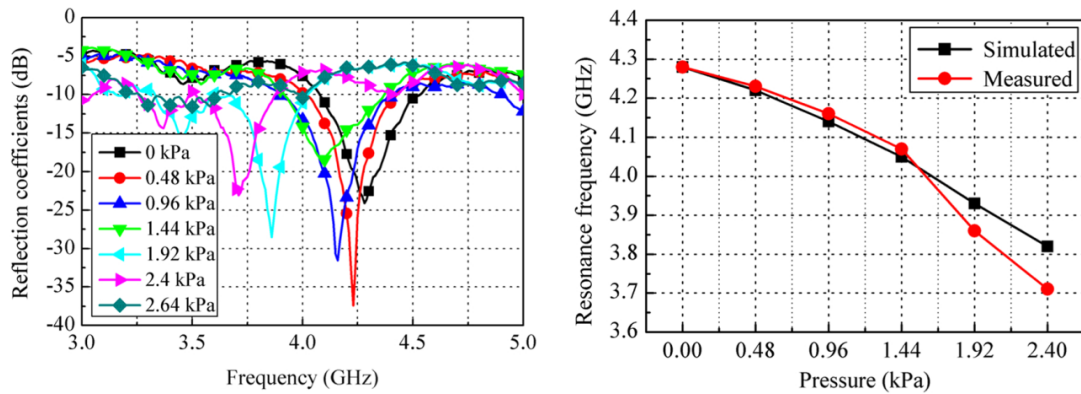


Figure 4.19: Measured frequency response of the hybrid printed SIW cavity pressure sensor.

CHAPTER 5

3D PRINTED “KIRIGAMI”-INSPIRED DEPLOYABLE BI-FOCAL BEAM-SCANNING DIELECTRIC REFLECTARRAY

5.1 Introduction

High performance antennas are critically important in modern wireless applications such as 5G communications, satellite communications, long-range RFID, remote sensing, etc. As discussed in Chapter 2, to date, there’s no origami-inspired antenna that can reach mm-wave frequency and have performance that is comparable to modern antenna arrays.

Parabolic reflectors and phased arrays are two of the most commonly used topologies for applications requiring narrow beams and high-gain antenna systems. However, parabolic reflectors are bulky, expensive and hard to fabricate especially above mm-wave frequencies due to their curved profile. Although phased arrays typically require individual tunable phase shifters, power amplifiers and complex feeding networks that dramatically increase their cost and difficulty of design, they feature significant additional beam steering capabilities. Reflectarray antennas combine some of the best features of both parabolic reflectors and phased array antennas, with the advantage of planar profile, relatively low-cost, ease of fabrication and can realize wide scan angles without any active components and feeding networks [78]. Additionally, planar reflectarray antennas can be transformed to foldable designs utilizing origami-inspired structures [79], membrane [80], or inter-PCB hinges [81], making reflectarray antennas ideal for satellite communication systems. In order to achieve a dynamic radiation pattern with a reflectarray antenna, mechanical tuning techniques can be utilized by rotating the feed source [82, 83]. In recent years, bi-focal design has proven to be an efficient method to improve the reflectarray scanning range [84, 85, 86].

One of the most significant challenges for mm-wave and terahertz reflectarrays is to reduce conductor losses caused by the metallic phase-shifting elements [87]. In recent years, significant work has been undertaken on dielectric reflectarrays, eliminating conductor losses by replacing the metallic phase shifters with high-dielectric phase delay structures. The phase delay can be tuned by changing the height of each element [88, 89, 90, 91, 92] or changing the effective permittivity of each area [93, 94]. Dielectric reflectarrays have demonstrated several advantages over traditional PCB-based reflectarrays: (1) eliminate conductor losses in the metallic resonant patch elements; (2) much wider bandwidth as dielectric structures are generally not frequency selective; (3) low cost and ease of fabrication by utilizing 3D printing and molding processes. However, most dielectric reflectarrays are using a solid block as a element and they are fabricated with rigid materials effectively eliminating the use of current deployable reflectarray techniques, thus, preventing them from being able to transform to portable designs. As a result, current dielectric reflectarrays occupy significantly more volume than traditional microstrip reflectarrays. The lack of deployability and retractability limit the applicable scenarios for dielectric reflectarrays extensively.

In this chapter, a novel “kirigami” inspired dielectric reflectarray is presented featuring high gain, wide bandwidth, beam-scanning ability, and deployability. This antenna features a bi-focal design with beam-scanning ability of -10° to -30° and 10° to 30° enabled by a phase optimization method. The deployable element structure was characterized and simulated to analyse the mechanical performance as well. The prototype was fabricated with a new stereolithography (SLA) 3D printable material Formlabs Flexible 80A with much better durability. A thorough characterization for this material was performed from 26 GHz to 40 GHz.

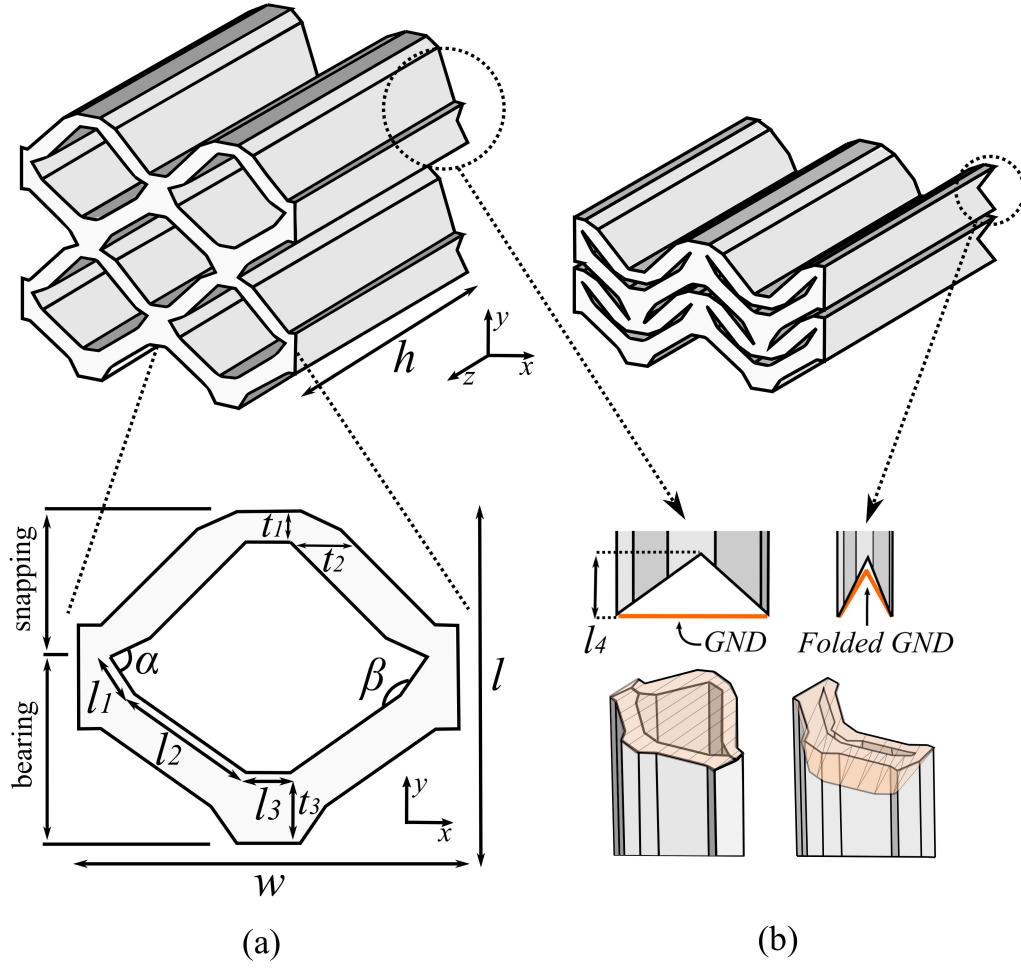


Figure 5.1: Element design: (a) deployed structure and top-view of one element; (b) folded structure and a detailed schematic of the ground plane retraction mechanism.

5.2 Element Design and Analysis

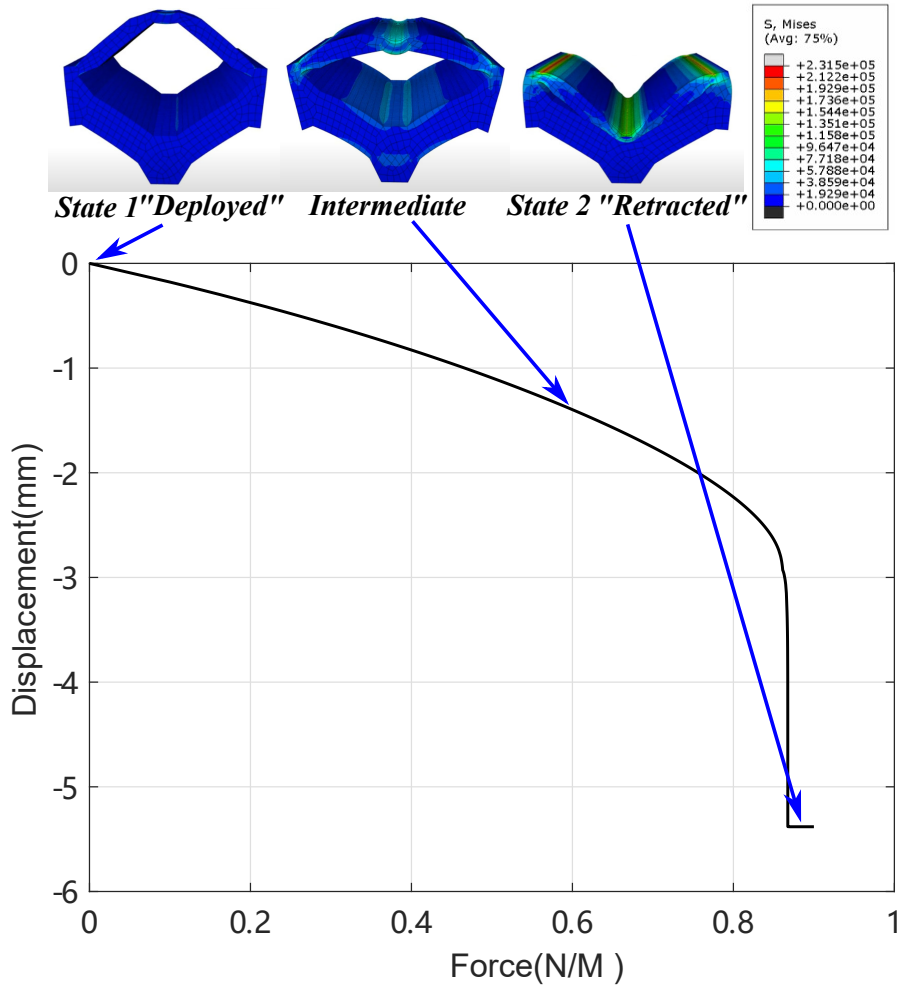
5.2.1 Mechanical Design

To realize a deployable dielectric reflectarray with minimum folded volume, we present a novel “snapping-like” structure inspired by a variation of origami involving cut sections called kirigami [95], as well as monolithic mechanical metamaterials [96]. To ensure an accurate phase-shifting response and geometry placement for reflectarray design, the element will be designed, simulated, and fabricated in a “deployed” configuration.

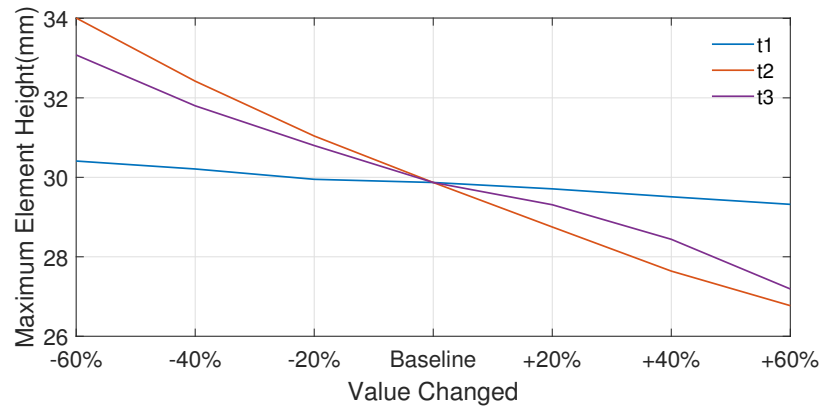
The element design is shown in Fig. 8.2a that consists of two segments: a snapping

segment and a bearing segment, forming a bi-stable mechanism. The structure is designed to be actuated with a electric motor, or a mechanical switch. The phase of the reflected wave is controlled by varying the height h of the element, while each element will have the same cross-section dimensions. The dimensions of the element are defined by four lengths l_1, l_2, l_3, l_4 ; three dielectric thicknesses t_1, t_2, t_3 and two angles: α, β . Another advantage of the proposed design, as compared to a rhomboid structure, is that it minimizes the total width w variation across retracted and deployed states, resulting in a Poisson ratio close to zero. This means that the reflectarray will not expand or contract along the X axis during deployment and operation. This is primarily due to angle α and length l_1 that create a triangle-shaped hinge which allows the snapping segment to “snap” onto the bearing segment. The bottom cut-out with depth l_4 as shown in Fig. 5.1b is to facilitate a foldable ground plane underneath the reflectarray. The dimensions of the element are chosen as: $l_1 = 1\text{mm}$, $l_2 = 2.9\text{mm}$, $l_3 = 1\text{mm}$, $l_4 = 2\text{mm}$, $\alpha = 82^\circ$, $\beta = 160^\circ$, $t_1 = 0.6\text{mm}$, $t_2 = 1.2\text{mm}$, $t_3 = 1.7\text{mm}$, $w = 8.11\text{mm}$, $l = 7.35\text{mm}$, to display good foldability while maintaining an area less than $1\lambda^2$ to ensure an accurate phase distribution.

The material utilized in this design is Formlabs Flexible 80A, a photopolymer with better printability and durability than the previous [97] Flexible FLGR02. This flexible material is a “rubber-like” elastomer with Young’s modulus of 4.4 MPa. The material is simulated based on 80A durometer rubber with Poisson’s ratio of 0.45. The structure is simulated and optimized in Abaqus CAE 2019 with finite element method (FEM) solver. The mechanical response of the structure is shown in Fig. 5.2a. The displacement is defined as the distance of the snapping segment travelled along z-axis when pressure applied on top of it. The color on the 3D structure indicates the Von Mises stress distribution with red color showing the areas with the highest stress. When applying pressure to the deployed structure from the top of the snapping segment, initially, the displacement versus force is linear. When pressure reaches $0.83\text{N}/\text{M}^2$ the snapping segment will rapidly conform to the bearing segment, and the structure will reach it’s second stable “Retracted” state. Generally,



(a)



(b)

Figure 5.2: Mechanical simulation results: (a) Force versus Displacement, from “Deployed” stage to “Retracted” stage; (b) maximum element height versus geometry parameters t_1 , t_2 , t_3 sweep around the design baseline values.

the stiffness of the element structure is controlled by t_1 and t_2 ; for smaller values of t_1 and t_2 , lower values of external forces will be needed to retract the structure but if the t_1 and t_2 are too small, the printability will be reduced. Fig. 5.2b shows how large the element height h needs to be to cover the full 360° phase shift when sweeping the values of t_1 , t_2 , and t_3 from -60% to 60% away from the baseline used for the design. When decreasing the value of t_1 , t_2 , or t_3 , the dielectric density of the element will be reduced, thus, decrease the effective dielectric constant, additional height h will be required for the same amount of phase delay. For larger values of angle α , the snapping segment will tend to lock onto the bearing segment more securely; while for vary small values of angle α , the structure can “pop-up” automatically when the external forces are removed.

5.2.2 RF Design

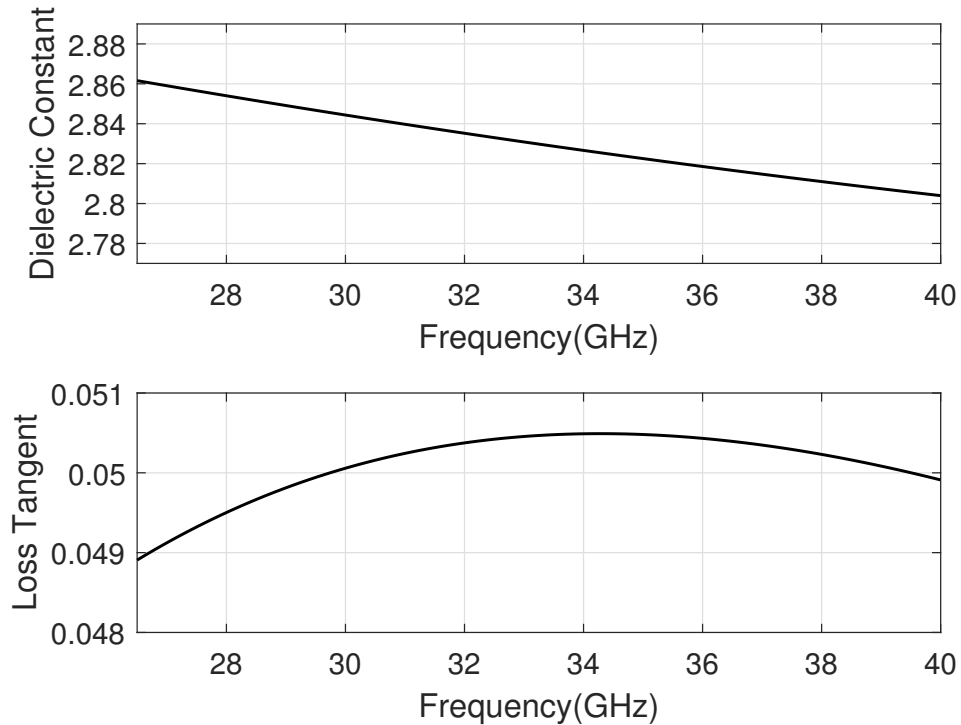


Figure 5.3: Formlabs Flexible80A Material Characterization Results: dielectric constant versus frequency (top); loss tangent versus frequency (bottom)

The Formlabs Flexible80A material is characterized using Nicolson-Ross-Weir (NRW) methodology with 3D printed WR28 waveguide samples and A-INFO 28CLKA2 waveguide calibration kit. The characterization results is shown in Fig. 5.3, the dielectric constant at 30 GHz is 2.763 with loss tangent of 0.042.

The element with dimensions discussed in the previous section is designed and simulated in CST Studio Suite 2019 frequency domain solver with unit cell boundary conditions and Floquet port excitation. The phase delay of one element can be tuned by varying the height h (Fig. 5.1a). The simulated phase response and reflection coefficient with respect to different angle of incidence (AoI) is shown Fig. 5.4 and Fig. 5.5. The phase fluctuations in Fig. 5.4 are caused by the combination of incident and reflected waves. A full 360° phase shift can be obtained by changing the element height h from 8.00 mm to 29.87 mm when $AoI = 0^\circ$. The simulation data is processed with a linear interpolative curve fitting algorithm to ensure any desired phase value can be matched with a precise element height. It can be observed in Fig. 5.4, the phase response of the dielectric element will be changed under different oblique incident angles, introducing phase errors to the design. Thus, it is critical to optimize the phase distribution efficiently to realize wide beam-scanning abilities and minimize the array's overall phase error with the optimization process to be discussed in the following section.

5.3 Reflectarray Design, Fabrication and Measurement

5.3.1 Reflectarray Design

Bi-focal Phase Distribution

To achieve a reconfigurable radiation pattern for a reflectarray antenna, various beam-scanning methodologies can be utilized. One common approach is by introducing active components e.g., use RF diodes/switches to turn the element on and off [98, 99], use electric motors to tune the phase response of each element [100, 101], or use tunable loading

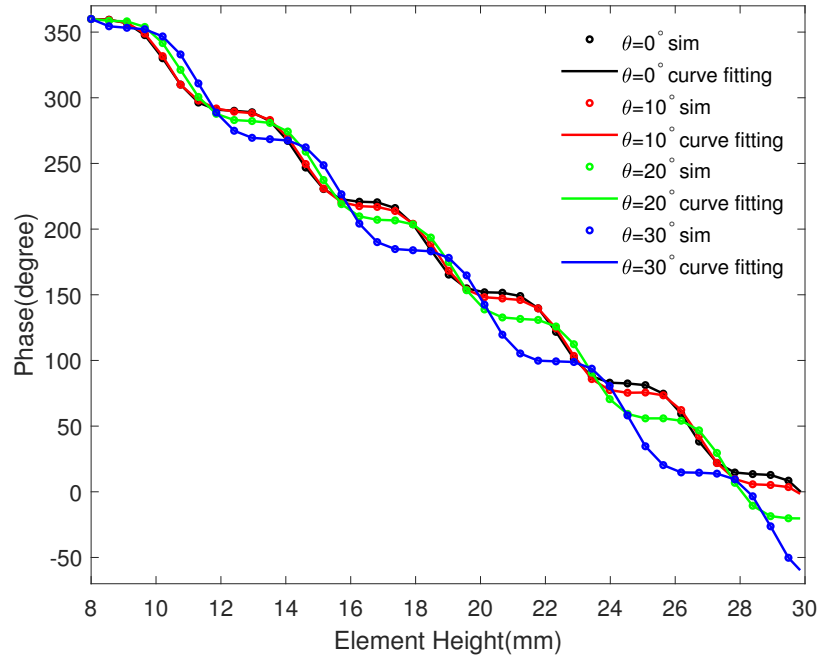


Figure 5.4: Simulated phase response versus element height for different AoI values at 30 GHz.

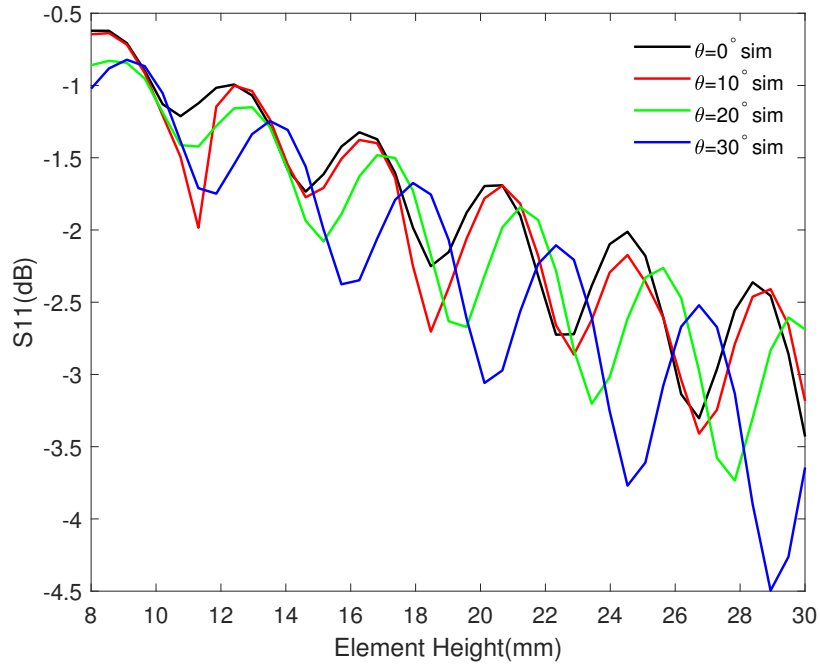


Figure 5.5: Simulated reflection coefficient versus element height for different AoI values at 30 GHz.

materials such as graphite [102], fluids [103], etc. The active tuning approach can be fast, accurate and achieves a wide range of scanning angles. However, the active components can be bulky, expensive and require a complex feeding circuit. As a result, the reflectarray can be unreliable, difficult to fabricate, and occupy a significant larger volume. Another approach to achieve reconfigurable pattern is by rotating the excitation antenna [82, 83, 84]. In contrast, no active component is required so the design can be low-cost, easy to fabricate, and maintain a constant volume.

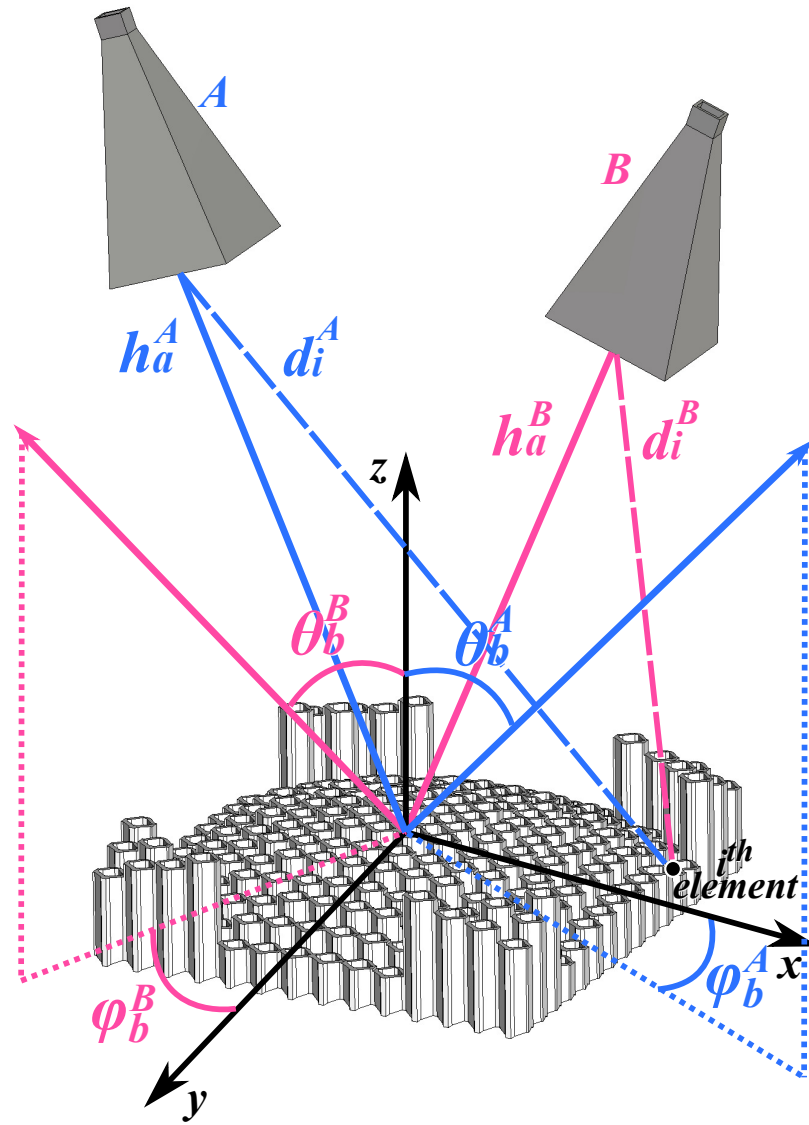


Figure 5.6: Schematic of the bi-focal beam scanning reflectarray setup.

In this design, a well-studied bi-focal method [84] is utilized to realize a wide beam scanning range with uniform gain response across different scanning angles when rotate the feed horn antenna from point A to point B as shown in Fig. 5.6. Two yz-plane symmetrical feed horn antenna positions define the two focal points for the reflectarray. The ideal phase shifting value of the i^{th} element $\phi(x_i, y_i)$ at any given position (x_i, y_i) with respect to feed horn antenna A or B can be calculated by (5.1) and (5.2).

$$\phi(x_i, y_i)^{A/B} = k_0(d_i^{A/B} - (x_i \cos(\varphi_b^{A/B}) + y_i \sin(\varphi_b^{A/B})) \sin(\theta_b^{A/B})) \quad (5.1)$$

$$d_i^{A/B} = \sqrt{(x_i - h_a^{A/B} \sin(\theta_b^{A/B}))^2 + y_i^2 + (h_a^{A/B} \cos(\theta_b^{A/B}))^2} \quad (5.2)$$

where k_0 is the propagation constant in vacuum at the center frequency of the design; d_i is the distance between feed horn A/B phase center and element i ; φ_b is the azimuth angle of the main beam with respect to x-axis and θ_b is the elevation angle of the main beam with respect to z-axis. To simplify the problem, we set $\varphi_b^{A/B} = 0^\circ$. In this design, we choose $\theta_b^A = -30^\circ$, $\theta_b^B = 30^\circ$, $h_a^A = h_a^B = 240\text{mm}$. The ideal phase response can be written as

$$\phi(x_i, y_i)^A = k_0(d_i^A - x_i \sin(\theta_b^A)) \quad (5.3)$$

$$\phi(x_i, y_i)^B = k_0(d_i^B - x_i \sin(\theta_b^B)) \quad (5.4)$$

For bi-focal reflectarray design, the required phase for i^{th} element will be an averaged value of the ideal phases

$$\phi(x_i, y_i) = \frac{\phi(x_i, y_i)^A + \phi(x_i, y_i)^B}{2} \quad (5.5)$$

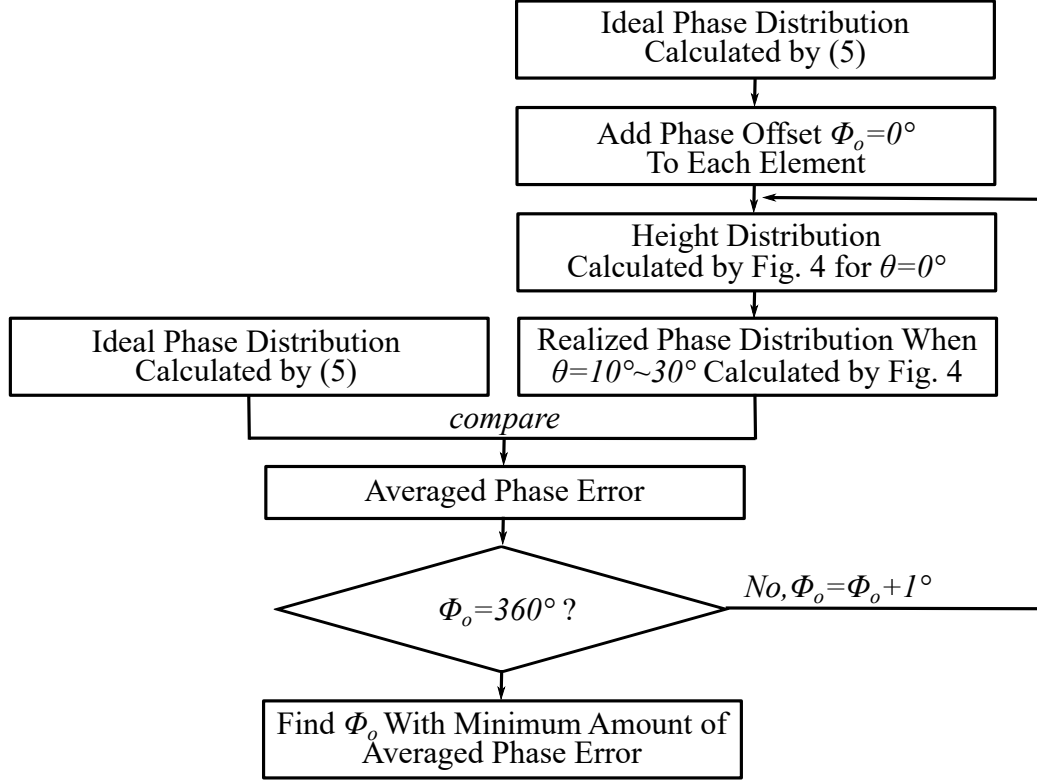


Figure 5.7: Schematic of the phase optimization program.

Phase Optimization

As discussed in Section II, the phase response of every individual dielectric element will change significantly depending on the AoI value. Typically, the reflectarray is designed based on the $AoI = 0^\circ$ simulation results. Thus, significant phase error will be introduced as the feed horn antenna rotates, and the performance of the reflectarray will be compromised. To alleviate this issue, the optimization algorithm shown in Fig. 5.7 is developed to minimize the overall phase error.

The initial reflectarray design with the appropriate element heights relies on the “ideal” phase distribution calculated by (5); then a compensating fixed phase offset ϕ_o is added to all elements. With this added phase offset, the height distribution of the array calculated by Fig. 5.4 for $\theta = 0^\circ$ will be different from the design without a phase offset. Next, we evaluate the realized phase distribution calculated by Fig. 5.4 under different incident

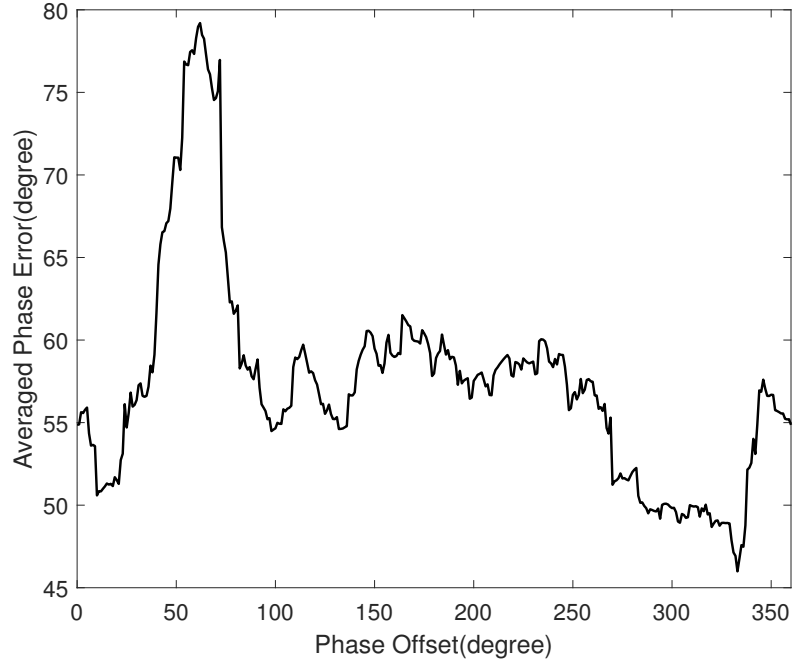


Figure 5.8: Output of the phase optimization program: lowest phase error at 333° offset.

angles, and compare this realized phase distribution with the ideal case calculated by (5), thus, we can obtain the averaged phase error for a certain phase offset ϕ_o . By repeating the process for ϕ_o values increasing by 1° over the range of 0° to 360° , the ϕ_o value featuring the minimum amount of averaged phase error over all different elements with respect to the ideal phase distribution can be identified, thus defining the corresponding compensated phase distribution and height distribution.

In this work, a $118mm \times 118mm$ array with 14×16 elements is presented. The dimension of this design is limited by the size of 3D printer's build plate, 3D printers with larger printable dimension are commercially available for larger array design. The utilized excitation is A-INFO LB-180400-20-C-KF wideband horn antenna. The CAD model of the excitation was imported to CST Studio Suite 2019 for the full-wave simulation to evaluate the performance of the dielectric reflectarray. The output of the optimizer is shown in Fig. 5.8, and performance comparison between optimized phase offset and other offset values is shown in Table 5.1, the phase distribution calculated by (5) is shown in Fig. 5.9a,

Table 5.1: Performance Comparison of Different Phase Offset

Phase Offset	333deg (best)	150deg	67deg (worst)
Gain@10deg	24.9dBi	23.3dBi	18.9dBi
SLL@10deg	-20.17dB	-17.34dB	-15.43dB
Gain@30deg	25.0dBi	24.3dBi	20.4dBi
SLL@30deg	-18.5dB	-16.33dB	-13.44dB

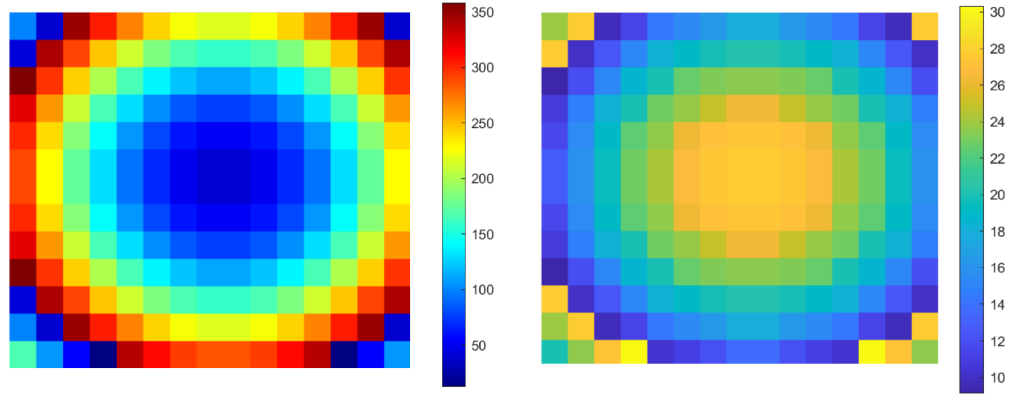


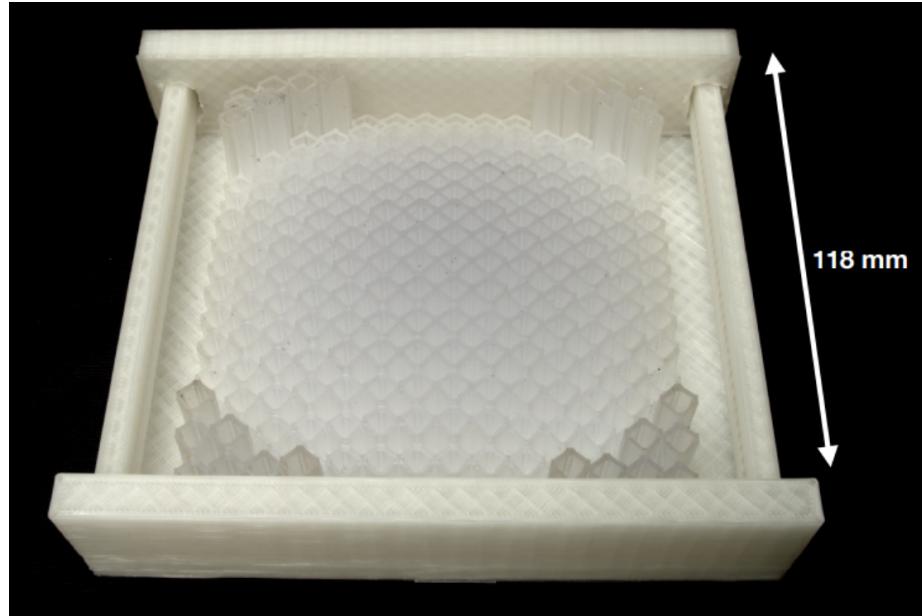
Figure 5.9: (a) Phase distribution of the bi-focal reflectarray; (b) Element height distribution of the bi-focal reflectarray.

and the height distribution calculated according to Fig.5.4 $\theta = 0^\circ$ is shown in Fig. 5.9b.

5.3.2 Fabrication

The prototype is fabricated with Formlabs Form 3 3D printing system. The photosensitive resin Flexible80A is commercially available with consistent material properties. The prototype is printed flat to avoid internal support structures with ground plane side facing build plate. $50\mu\text{m}$ layer thickness is utilized during the printing and a wash-and-cure post processing is proceeded after the printing. SLA 3D printed samples generally have uncured leftover resin, hence a 10 minutes wash in 91% isopropyl alcohol is utilized to remove the extra resin to ensure improved accuracy and surface smoothness. Thereafter the washed sample will be cured under 60°C with 405nm LED lights for 30 minutes to maximize cross-linking of the photopolymer, optimize structural properties, increase consistency and

reduce electromagnetic losses.



(a)



(b)

Figure 5.10: Fabricated sample: (a) fully deployed sample (front side); (b) fully retracted sample (back side).

A fabricated sample is shown in Fig. 5.10a, and a fully retracted sample is shown in Fig. 5.10b. The fabricated dielectric reflectarray is held by a 3D printed frame, the retracted array can be deployed in “one-shot” with a mechanical switch. The retracted array demonstrates a 65% volume reduction in comparison with the fully deployed state.

5.3.3 Simulation and Measurement Results

The measurement setup for the beam-scanning dielectric reflectarray is shown in Fig. 8.7. The reflectarray is held by a 3D printed frame with a rotatable arm to tune the scanning angle. Two A-INFO LB-180400-20-C-KF wideband horn antennas are utilized as the excitation and receiver. The distance between the reflectarray and the receiver is 1.70 meters.

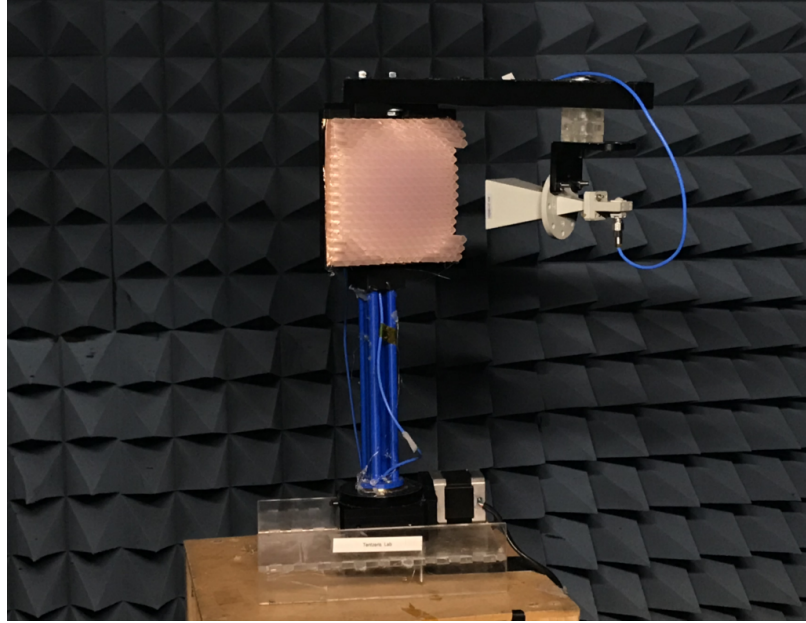
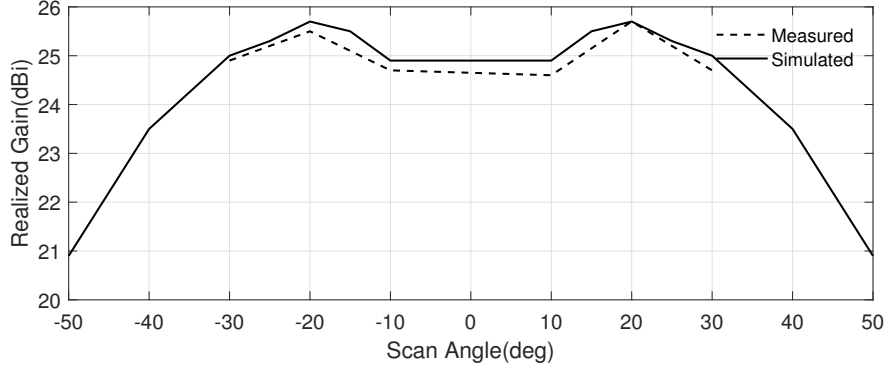


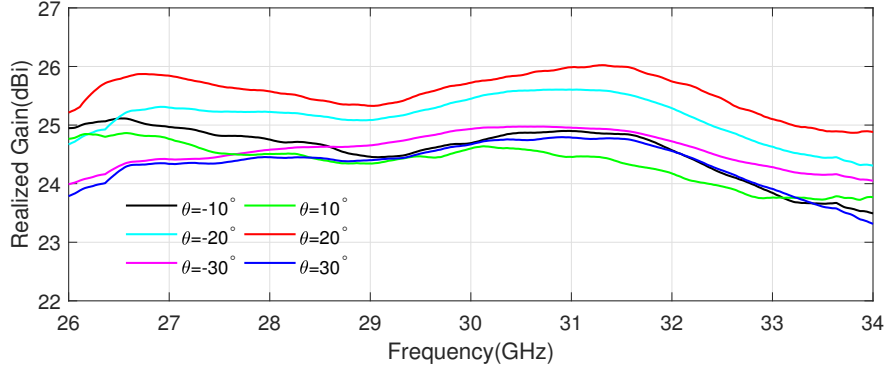
Figure 5.11: Measurement setup.

The simulated and measured realized gain versus scan angles is shown in Fig. 5.12a. The simulation and measurement data show good matching, the optimized bi-focal design shows controlled gain variation behaviour with less than 1dB. The broadside beam (0 scan angle) is not studied due to the aperture blockage effects from the feed antenna. The measured realized gain versus frequency is shown in Fig. 5.12b.

Fig. 5.13 shows the simulated and measured radiation patterns across -10° to -30° scan angles with 10° resolution. Fig. 5.14 shows the simulated and measured radiation patterns across 10° to 30° scan angles with 10° resolution. The optimized bifocal reflectarray shows stable gain pattern and a good side lobe level (SLL) response. The SLL in simulation varies from -20.8dB to -17.68dB, while the measured SLL varies from -19.46dB to



(a)



(b)

Figure 5.12: (a) Simulated and measured realized gain versus scanning angle at 30 GHz; (b) measured realized gain versus frequency at different scanning angles.

-17.32dB. The SLL performance is mainly impacted by the 3D printer's resolution and accuracy. The photopolymer tends to be over-cured with long tube-shaped structures, causing the printed sidewall to be thicker than intended. Additionally, the long RF cable used during the measurement may impact the VNA's effective dynamic range that causes SLL discrepancy. Despite the slightly increased SLL, the measurement result show a close agreement with the simulation.

The realized gain, SLL, beamwidth, and bandwidth versus scan angles is summarized in Table 5.2. The prototype shows promising and consistent performance across the entire beam scan range.

The measured performance of the dielectric reflectarray design presented in this article is compared with state-of-art reflectarrays at similar frequency ranges is shown in Table

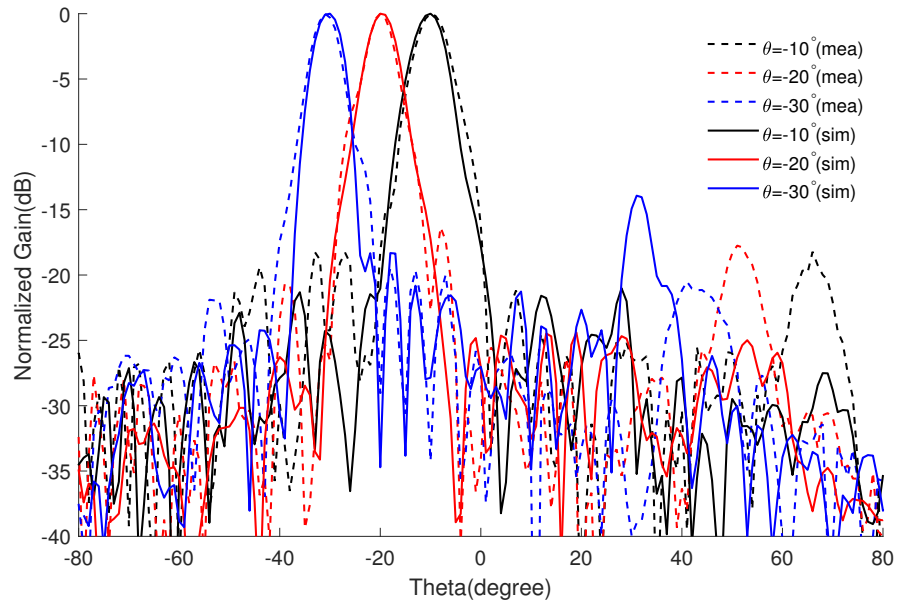


Figure 5.13: Measured and Simulated radiation patterns at 30 GHz with scan angles from -10° to -30° .

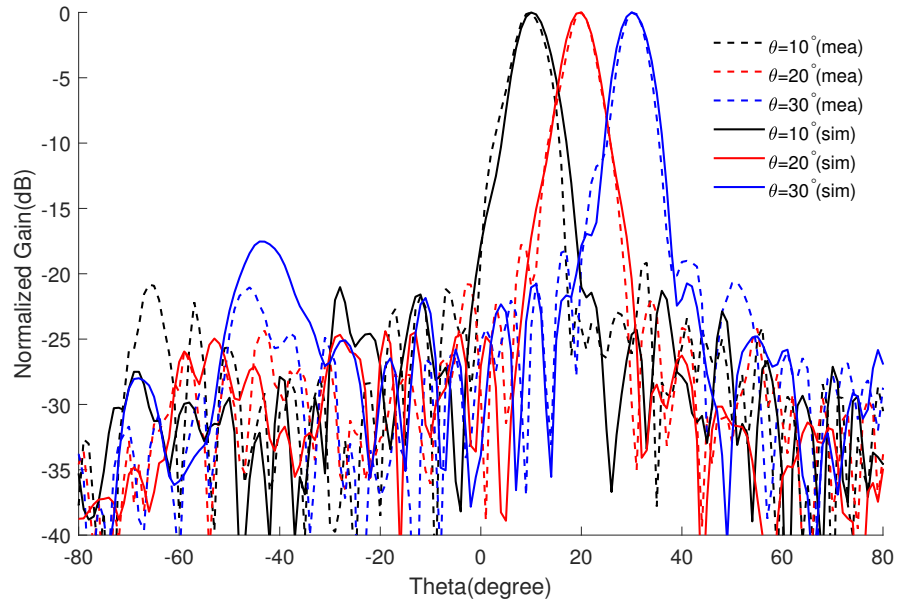


Figure 5.14: Measured and Simulated radiation patterns at 30 GHz with scan angles from 10° to 30° .

5.3. While the proposed design demonstrates widest bandwidth with good radiation performance. The aperture efficiency drop is mainly caused by the dielectric losses from the

Table 5.2: Summary of The Measurement Results @30 GHz

Scan Angle (deg)	-30	-20	-10	10	20	30
Realized Gain (dBi)	24.9	25.5	24.7	24.6	25.7	24.7
SLL (dB)	-19.46	-17.32	-18.22	-19.39	-17.77	-18.39
3dB Beamwidth (deg)	6.1	6.4	7.2	7.1	6.2	5.9
1dB Bandwidth (%)	25.4	21.4	18.7	17.5	21.8	25.2

Table 5.3: State-of-the-art Comparison

Design	[93]	[90]	[91]	[84]	This Work
Frequency	35GHz	30GHz	31GHz	32GHz	30GHz
Size	$153.9\lambda^2$	$144.0\lambda^2$	$154.0\lambda^2$	$227.0\lambda^2$	$129.3\lambda^2$
Realized Gain	23.9dBi	28.0dBi	28.3dBi	30.32dBi	24.6dBi
1dB Bandwidth	NA	10.0%	5.2%	4.3%	17.5%
Dielectric	Y	Y	Y	N	Y
Bi-focal	N	N	N	$\pm 30^\circ$	$\pm 30^\circ$
Deployability	N	N	N	N	Y
Aperture Efficiency	12.7%	34.8%	29.0%	37.6%	22.8%

material. This issue could potentially be improved by utilizing a low-loss flexible polymer. Another reason of the efficiency drop is the fact that when the excitation horn antenna rotates from 30° to 10° , the edge illumination of the array will drop from -3 dB to -8.5 dB as the feed horn antenna has an E-plane -3 dB beamwidth of 14° , and the feed center from the horn to the reflectarray is 240 mm. The proposed reflectarray is the only one offering beam-scanning ability, deployability, and full dielectric design simultaneously.

5.4 Summary

This chapter presented the first-of-its-kind one-shot deployable, beam steerable dielectric reflectarray inspired by kirigami structures and mechanical metamaterials. The design is realized through low-cost commercialized 3D printing systems with flexible materials. The

fabricated prototype shows high realized gain, wide-bandwidth, -10° to -30° and 10° to 30° of scan range, and 65% of volume reduction when retracted, enabling more space-limited high-end communication applications for dielectric reflectarrays. The flexible element structure can potentially introduce multi-stage reconfigurability to the design of dielectric reflectarray in future work.

CHAPTER 6

TRULY CONFORMAL TILE-BASED BEAMFORMING PHASED ARRAY WITH NOVEL 3D DEPTH CAMERA CALIBRATION

6.1 Introduction

Recent advances in communication technologies have created new desires for lightweight, conformal, and high-performance wireless Flexible Hybrid Electronics (FHE) in both consumer and defense applications such as internet of things (IoT), remote sensing, and telecommunications. Advanced communication systems typically require large phased array antennas; however, these phased arrays are usually quite bulky and heavy and come only in very limited sizes, and thus increasing the cost of customization and reducing the adaptability to various end-use cases. In addition, traditional phased arrays have planar design and utilize rigid materials, so it is very difficult to implement them onto non-flat surfaces such as aircraft wings, propellers, and modern buildings. Most of the available conformal phased array designs are transformed from a traditional planar design, and they usually have only one fixed shape so that the phase distribution can be calculated with a fixed formula. If the geometry of the phased array is changed, a very complicated and time-consuming calibration process will be needed to generate a new phase distribution formula.

To date, there are various approaches available to calibrate a phased array system depending on the applications and requirements. The most commonly used methods are probe-based process that measures near field [104, 105, 106], quasi-near field [107], or far field [108]. While probe measurement can provide accurate amplitude and phase data, the measurement process usually takes very long time as the multiple datasets need to be collected in various locations and orientations, which will increase the system downtime significantly. Additionally, the probe-based calibration process requires bulky and expen-

sive equipments, adding more cost in both logistics and human resources. Another approach of calibrating conformal phased array is to detect the mutual coupling between the elements [109, 110, 111]. The mutual coupling calibration methods can demonstrate good accuracy in detecting the radius for cylindrical phased arrays. However, for more complicated cases such as uneven surfaces and arbitrary spacings, the mutual coupling method will have very limited resolution. Furthermore, mutual coupling detection requires additional feeding circuits and requires the phased array elements to be switchable between TX mode and RX mode. This will significantly increase the cost and complicity of phased array systems as many of them are TX or RX only. Thus, an accurate, low-cost, easy-to-use method needs to be developed that has the ability of calibrating conformal phased arrays in any arbitrary shape on-the-fly.

In this chapter, a novel conformal phased array calibration method utilizes 3D depth camera and computer vision will be introduced. This method use the 3D depth camera or LiDAR sensor that are built into modern smartphones to calibrate conformal phased arrays within a few seconds on-the-fly. The concept is similar to the laser metrology computer control system used in Green Bank Telescope [112]. To demonstrate the performance of this method, a tile-based fully printable phased array architecture will be designed, the phased array tiles will be connected to a flexible inkjet printed tiling layer to enable the flexibility of the array.

6.2 3D Depth Camera

With the advancement of self-driving cars, smartphones, and AR/VR/MR technologies, the cost of a 3D depth camera system has been reduces dramatically from tens of thousands of dollars to a few hundreds of dollars. More and more 3D camera systems have been deployed onto consumer electronic devices such as stereo vision cameras used in drones from DJI, LiDAR sensors used in Apple iPad Pro tablets and Intel RealSense modules, structured-light 3D camera used in Apple FaceID modules and Microsoft Kinect modules,

these 3D cameras add depth information to the image that enables advanced applications in obstacle avoidance, 3D scanning, face and gesture recognition, etc.

Another potential application for these 3D depth cameras is to use the true depth and geometric information to detect and calibrate conformal phased arrays with arbitrary shapes shown in Fig. 6.1 such as rotation, shift, twist, etc.

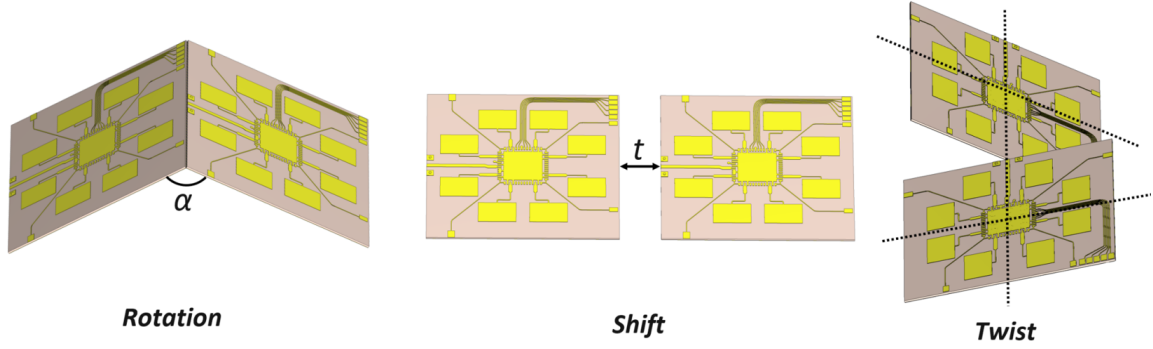


Figure 6.1: Detectable transformation of conformal phased array using 3D depth camera: rotation, shift, and twist.

6.2.1 Proof-of-concept Experiments

TrueDepth Camera

For proof-of-concept experiments, we are using the TrueDepth camera that built into most of the Apple iPhone smartphones since 2017. This camera module is picked for its availability and accessibility, low cost, as well as matured SDK (software development kit). Fig. 6.2 shows the TrueDepth camera module inside an iPhone 12 Mini that consists an IR (infrared) dot projector, an RGB (red-green-blue) camera, and an IR camera. This 3D depth camera module uses structured-light 3D reconstruction method where the IR dot projector will project a pre-defined IR dot grid, by detecting the parallax shift of the IR dots using the IR camera, the depth information can be extracted [113]. Fig. 6.3 shows the dot grid projected by the IR dot projector captured by a full-spectrum modified CCD sensor with a B+W 093 900 nm IR pass filter.

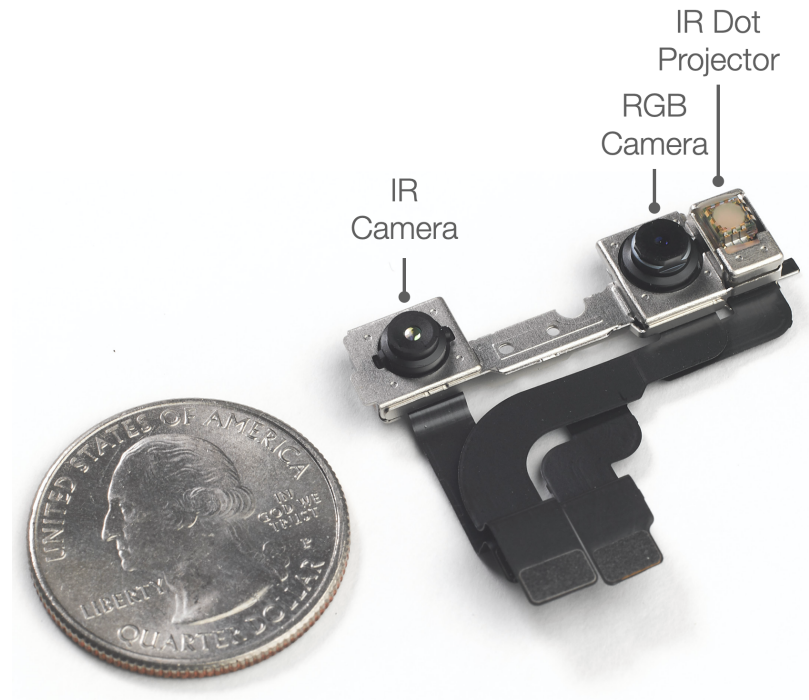


Figure 6.2: The TrueDepth camera module inside an iPhone 12 Mini.

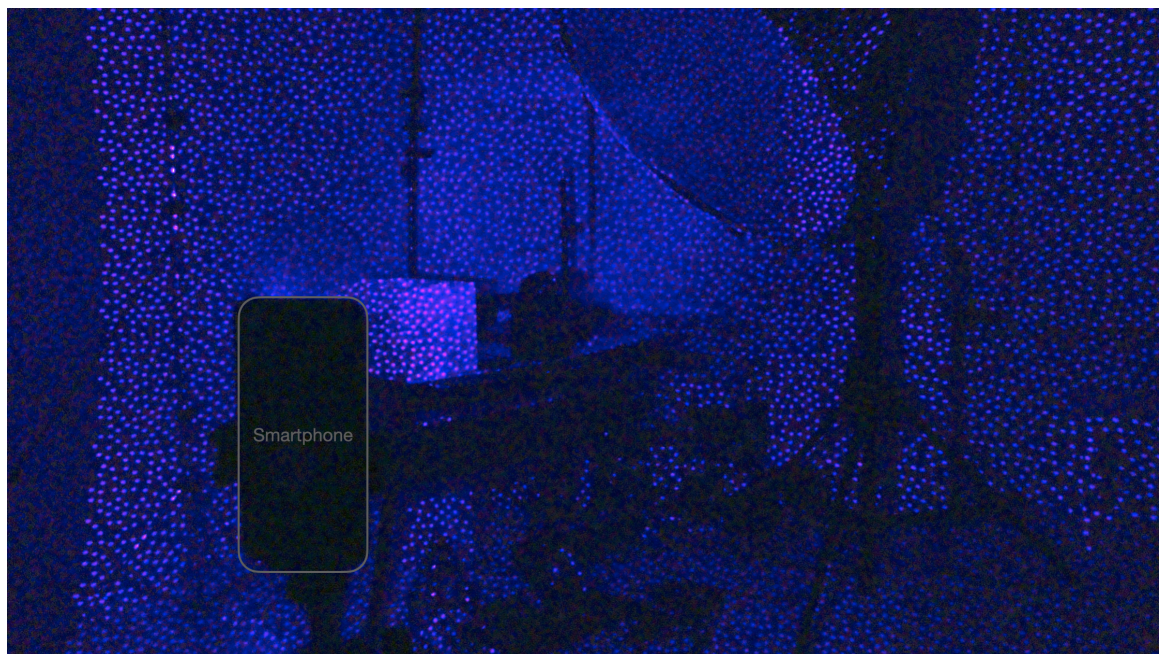


Figure 6.3: Projected IR dots captured by a full-spectrum modified CCD sensor with a B+W 093 900 nm IR pass filter

Read the Camera Data

The TrueDepth camera data can be accessed with SDK provided by Apple [114]. An app (Fig. 6.4) was modified based on the SDK to preview the camera data in real-time and save the data to *.txt* files to be processed in other platforms. The camera readout has 640×480 pixels in 16 bit depth resolution with maximum frame rates of 30 fps.

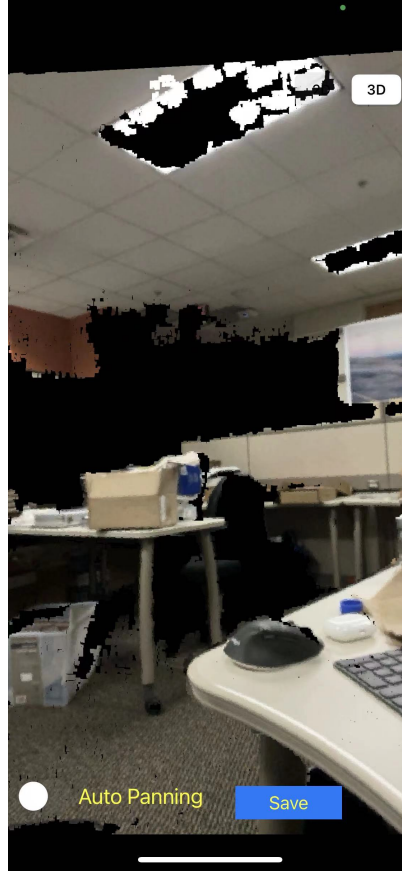


Figure 6.4: Modified app based on the SDK [114] with 3D real-time preview and data saving functions

The captured data are stored in a 2D $u - v$ coordinate system where u and v axis are the horizontal and vertical pixel count. A pixel that contains the depth information z can be located by a specific u and v number. The z depth of a point is defined by the distance from the point to the plane of the smartphone's screen. To extract the accurate shape information, the $u - v$ coordinate system need to be transformed into $x - y$ coordinate system where

x and y are the spatial x and y locations of the point. This uvz to xyz transformation can be performed using camera intrinsics matrix (6.1) which realates a camera's internal properties to an ideal “pinhole” camera model. In (6.1), f_x and f_y are the pixel focal lengths, x_0 and y_0 are the offsets of the principal point from the first pixel (top left corner of the image). The camera intrinsics matrix of the TrueDepth camera can be read with *AVCameraCalibrationData* API. The x and y location can be calculated by (6.2) and (6.3). Fig. 6.5 plots the captured depth image of a computer desk transformed from uvz to xyz coordinate system.

$$\begin{bmatrix} f_x & 0 & x_0 \\ 0 & f_y & y_0 \\ 0 & 0 & 1 \end{bmatrix} \quad (6.1)$$

$$x = (u - x_0) \times z / f_x \quad (6.2)$$

$$y = (v - y_0) \times z / f_y \quad (6.3)$$

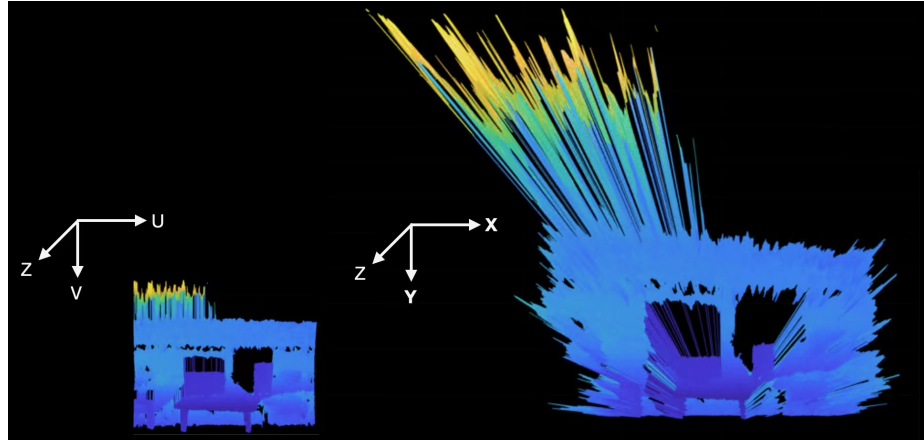
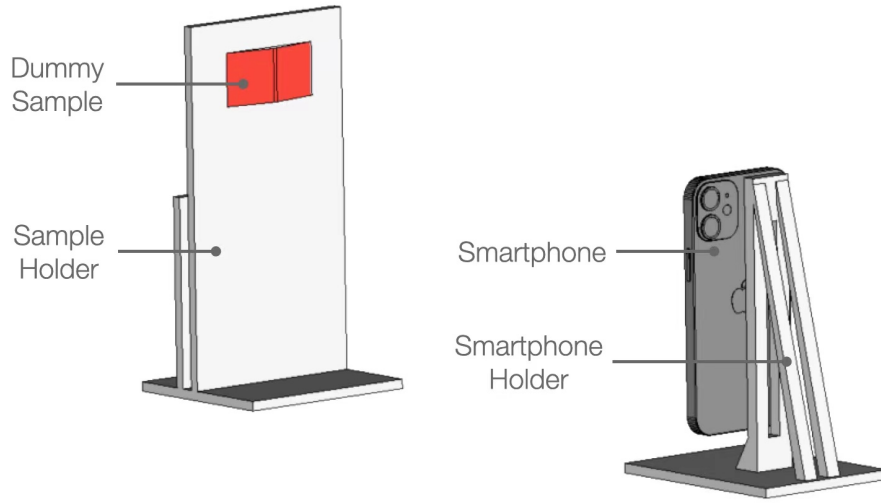


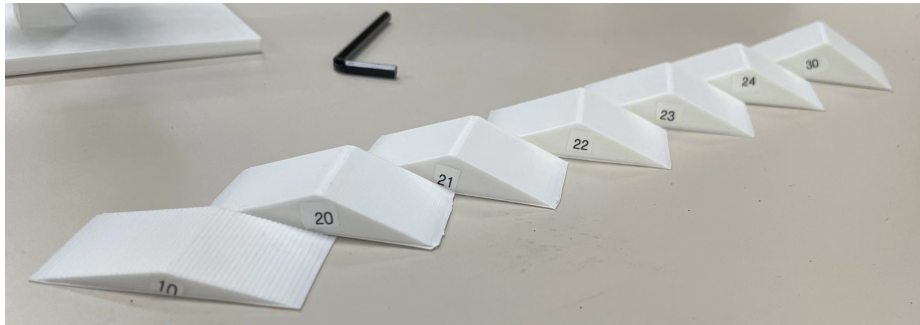
Figure 6.5: Captured depth image of a computer desk transformed from uvz (left) to xyz (right) coordinate system.

Experiment Setup

The first experiment is to verify the feasibility of using the TrueDepth camera to detect the “Rotation” angle shown in Fig. 6.1. To ensure the consistency of the captured data, measurement setup shown in Fig. 6.6a is designed and 3D printed which includes a smartphone holder, a sample holder plate, and a series of 3D printed dummy samples with different rotation angles from 10° to 30° (Fig. 6.6b).



(a)



(b)

Figure 6.6: (a) Design of the measurement setup to verify the feasibility of measuring “Rotation” angles using the TrueDepth camera; (b) 3D printed dummy samples with different rotation angles from 10° to 30° .

Data Processing Script

The captured raw data of a 20° dummy sample is shown in Fig. 6.7a. An automated data processing script was written in MATLAB with three critical steps:

- Find the plane normal of the sample holder to calibrate x-y plane.
- Find one edge of the dummy sample to calibrate z-axis rotation angle.
- Define data sampling range.

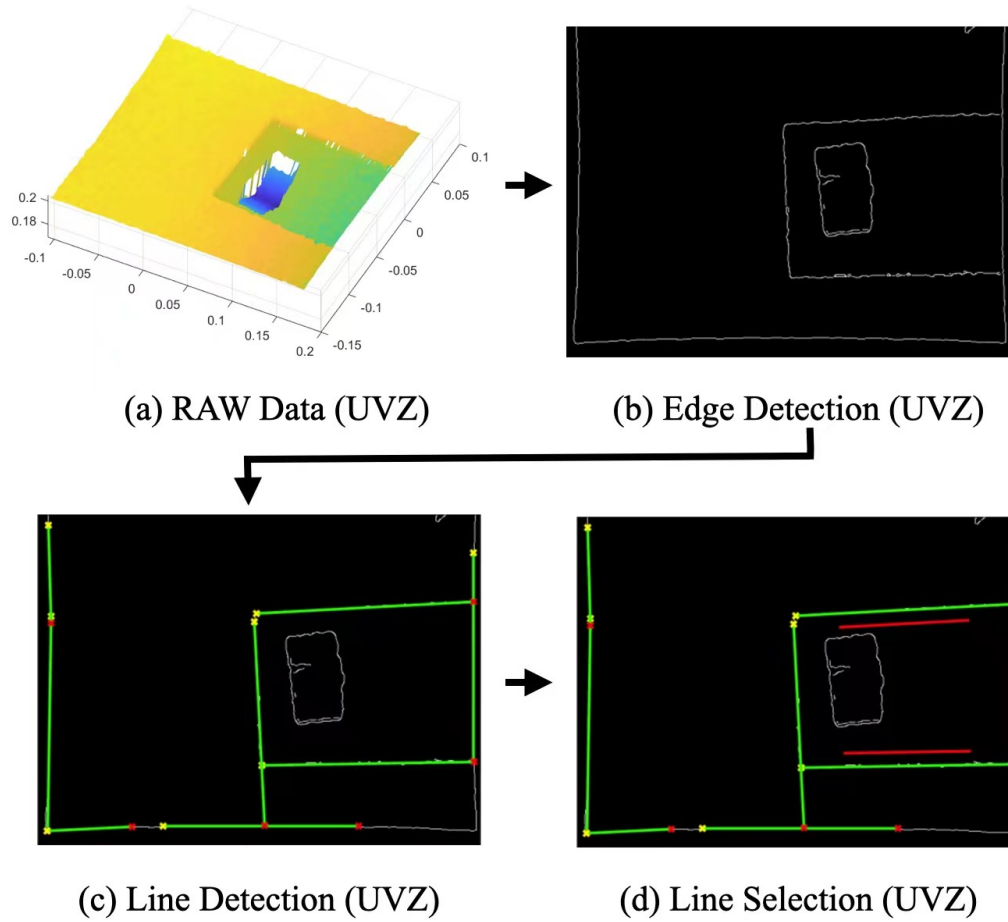


Figure 6.7: First step of data processing: calibrate x-y plane; (a) raw data; (b) edge detection; (c) line detection; (d) line selection.

Within the first step, the raw data will be converted to a greyscale image, then a “Canny” edge detector will be utilized to extract the edge of the sample holder and the edge of the

dummy sample (Fig. 6.7b). Next, the Standard Hough Transform (SHT) will be applied to the edge detection result and line detection (Fig. 6.7c) will be performed with *houghlines* function that extract the line information based on SHT. Finally, two edge lines of the sample holder will be selected (red lines in Fig. 6.7d) to calibrate the x-y plane. By running a linear interpolate curve fitting algorithm, the line equations of the selected two lines can be extracted. With the line equations, the plane normal of the sample holder (Fig. 6.8a) can be calculated. With the plane normal, the rotation of x-y axis can be calibrated to ensure a flat x-y plane. Fig. 6.8b shows the plot of the data without x-y plane calibration, where the sample holder shows a gradient color meaning the plane is tilted. With the x-y plane calibration, the sample holder is showing singular color as shown in Fig. 6.8c.

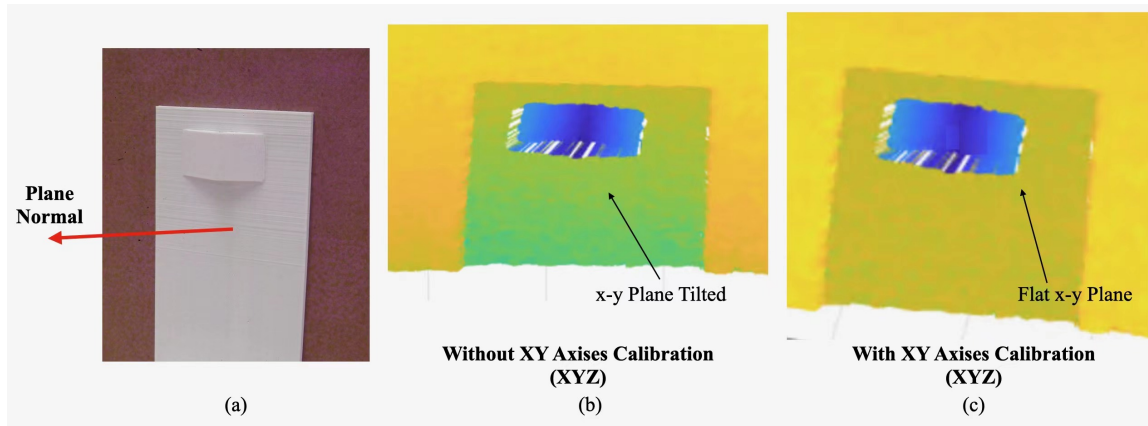


Figure 6.8: Results of the first step data processing: (a) definition of the sample holder's plane normal; (b) without x-y plane calibration; (c) with x-y plane calibration.

Fig. 6.9 shows the second step of data processing to calibrate the rotation of z-axis. Based on the output of the first step (Fig. 6.9a), the image will be cropped to ignore irrelevant data and focus on the dummy sample area (Fig. 6.9b). Then another SHT-based edge detection (Fig. 6.9c) will be performed with lower threshold to detect the lines around the dummy sample. Finally, one edge of the dummy sample will be selected (Fig. 6.9d) to calibrate the z-axis rotation of the dummy sample. As shown in Fig. 6.10, after z-axis calibration, the top edge of the dummy sample is leveled.

From the first and second step of data processing, we can extract the amount of axis

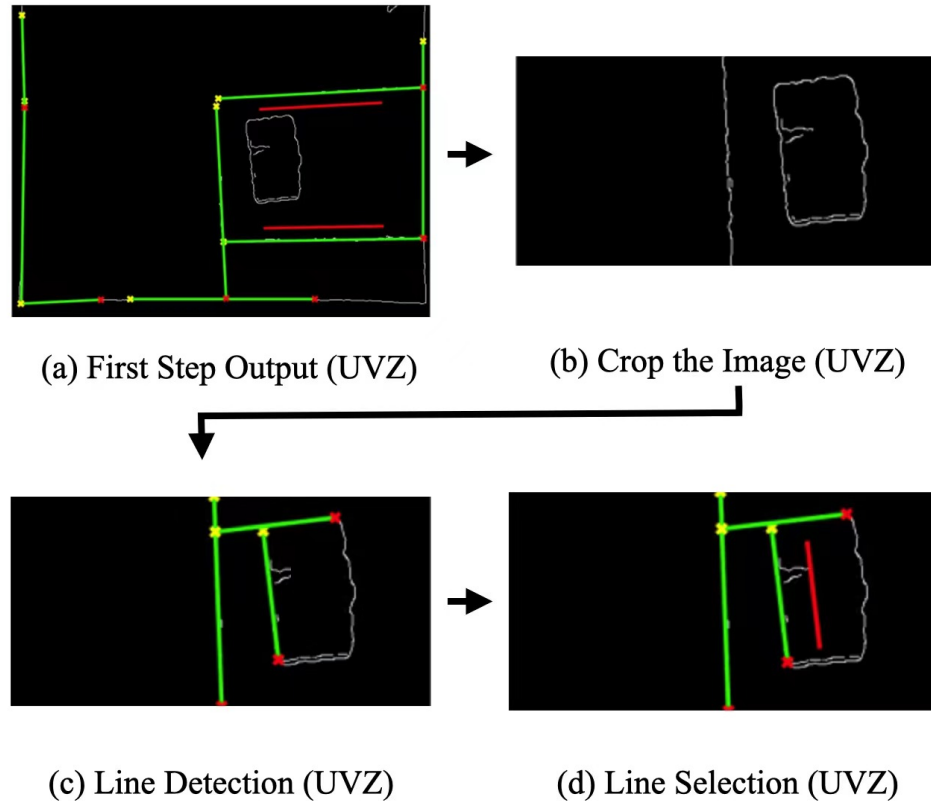


Figure 6.9: Second step of data processing: calibrate z axis; (a) output of the first step; (b) crop the image to focus on the dummy sample; (c) line detection with lower threshold; (d) line selection.

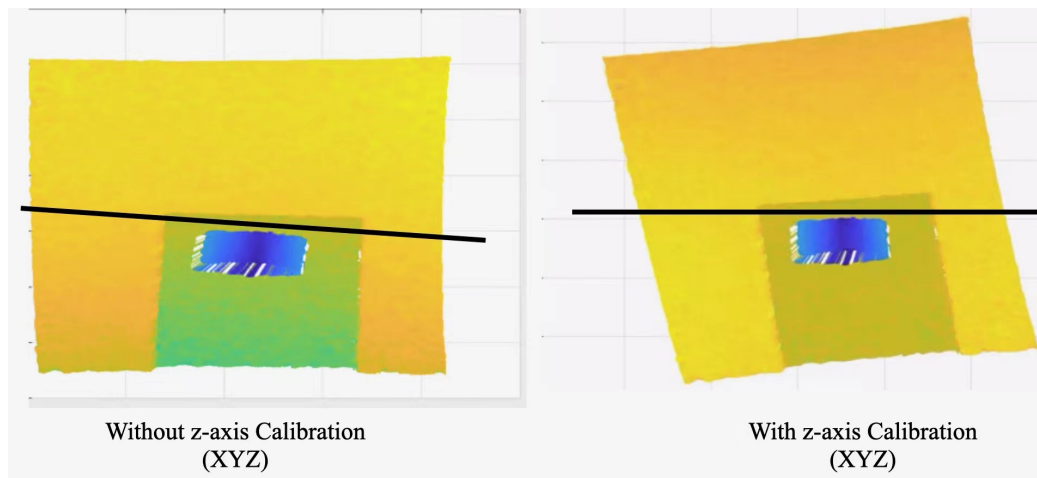


Figure 6.10: Results of the second step data processing: without x-axis calibration (left); with x-axis calibration (right).

rotation needed θ_x , θ_y , θ_z to calibrate the x-y plane and z-axis. The un-calibrated xyz coordinate can be transformed to the calibrated xyz coordinate with the rotation matrix R where,

$$\begin{bmatrix} X_{cal} \\ Y_{cal} \\ Z_{cal} \end{bmatrix} = [R] \begin{bmatrix} X_{uncal} \\ Y_{uncal} \\ Z_{uncal} \end{bmatrix} \quad (6.4)$$

$$[R] = [R_x] [R_y] [R_z] \quad (6.5)$$

$$[R_x] = \begin{bmatrix} 1 & 0 & 0 \\ 0 & \cos(\theta_x) & -\sin(\theta_x) \\ 0 & \sin(\theta_x) & \cos(\theta_x) \end{bmatrix} \quad (6.6)$$

$$[R_y] = \begin{bmatrix} \cos(\theta_y) & 0 & \sin(\theta_y) \\ 0 & 1 & 0 \\ -\sin(\theta_y) & 0 & \cos(\theta_y) \end{bmatrix} \quad (6.7)$$

$$[R_z] = \begin{bmatrix} \cos(\theta_z) & -\sin(\theta_z) & 0 \\ \sin(\theta_z) & \cos(\theta_z) & 0 \\ 0 & 0 & 1 \end{bmatrix} \quad (6.8)$$

Fig. 6.11 shows the third step of the data processing that uses the selected line in Fig. 6.9d to sample the data. The sampled area has 30 mm y-axis span and 220 mm x-axis span from the center of the dummy sample. Linear interpolate curve fitting algorithm will be utilized to extract the slope of the left side and right side of the sampled data, to get $angle1$ and $angle2$. The rotation angle of the dummy sample will be: $angle_{rot} = (angle1 + angle2)/2$. The curve fitting results are shown in Fig. 6.12.

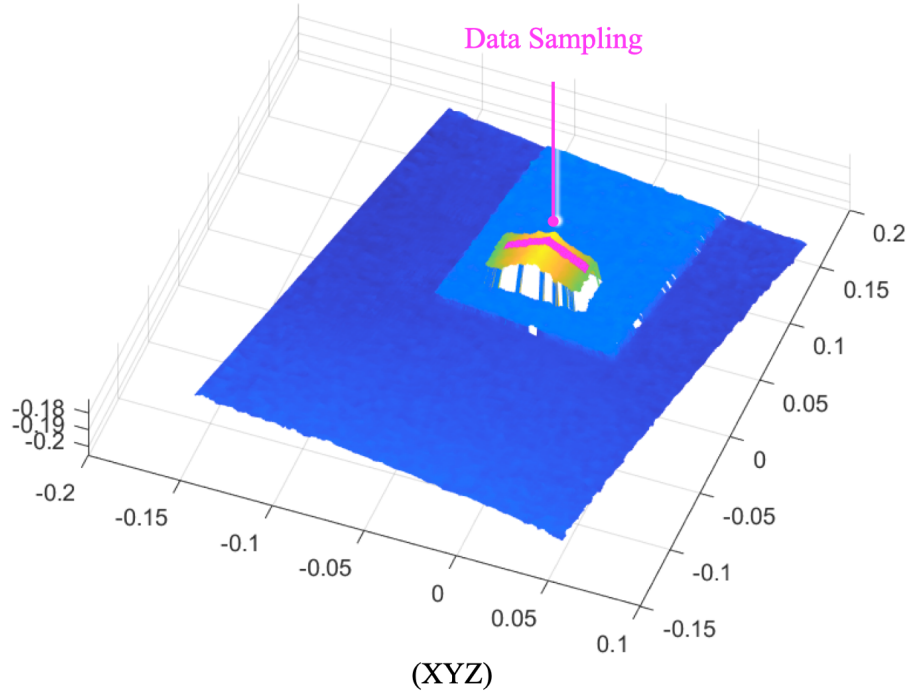


Figure 6.11: Third step of data processing: data sampling.

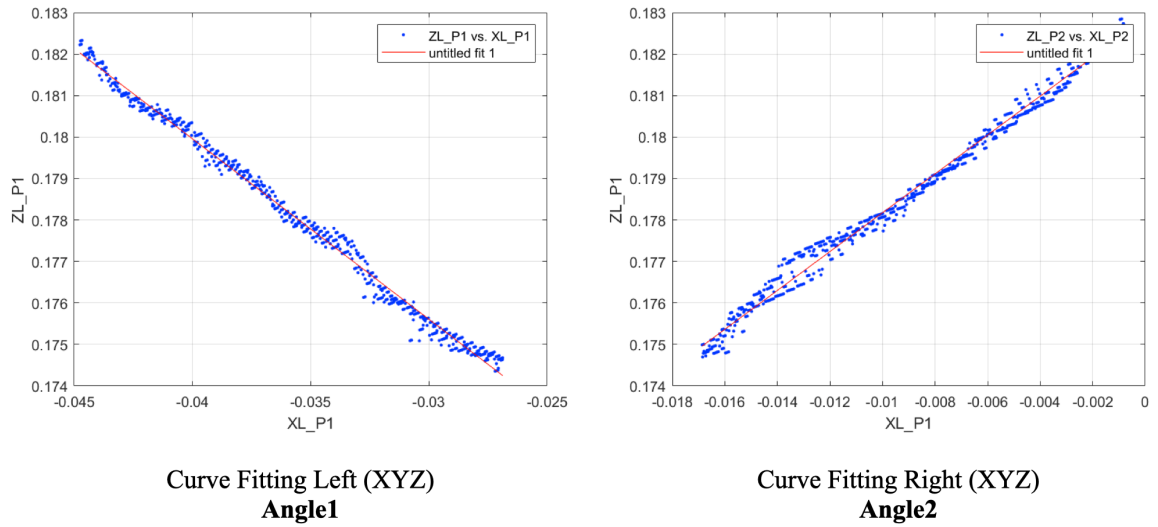


Figure 6.12: Curve fitting results of the left side (angle1) and right side (angle2) of the dummy sample.

Experiment Results

The 3-step data processing procedure is written as an automated script in MATLAB. Three sets of data was taken for each 3D printed dummy sample shown in Fig. 6.6b, in total, 21

sets of data were collected. All the data were successfully go through the MATLAB script, the output angles are shown in Table. 6.1. And the results are plotted in Fig. 6.13. The measurement results demonstrated exceptional rotation angle detection accuracy with the 3D TrueDepth camera, with the minimum averaged delta (Δ_{ave}) of 0.1948° and maximum averaged delta 0.7874° . With less than 1° averaged error, it proofed the 3D depth camera calibration method should have enough resolution as most of the beamforming ICs have phase control resolution less than 6 bit.

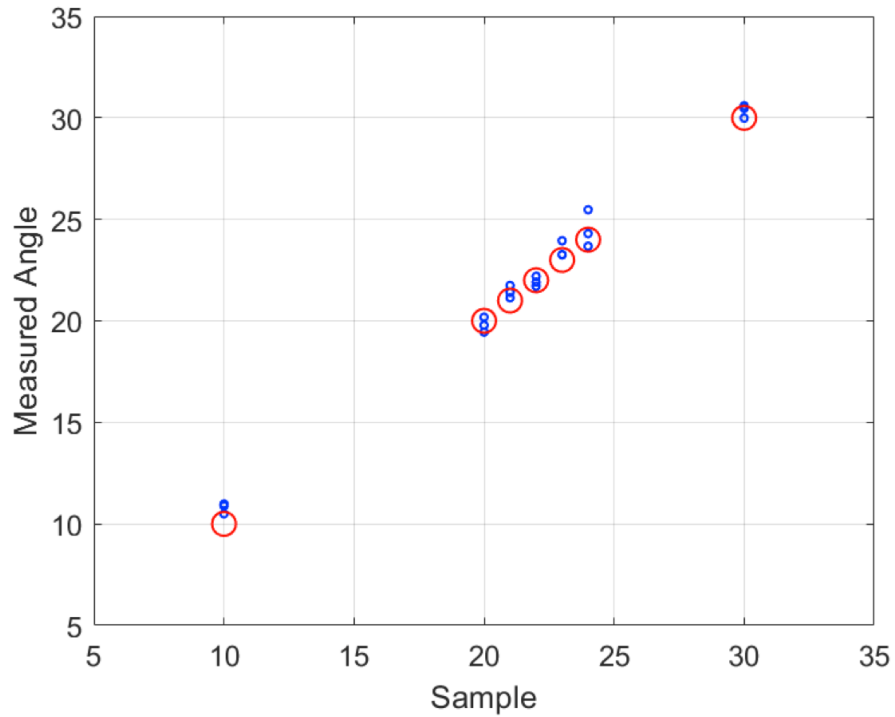


Figure 6.13: Rotation angle detection preliminary measurement Results.

6.2.2 Phased Array Tile

The development of 5G and mm-wave technologies have enabled the connection of next-generation of IoT and massive MIMO devices with high data rates and wideband operations. To satisfy the link budget, antenna arrays in different sizes are designed and utilized in an application-specific manner, which requires more design and fabrication time and cost. So solve this challenge, we choose to use a tile-based phased array architecture shown

Table 6.1:
Rotation Angle Detection Preliminary Measurement Results

Angles	Measurement1	Measurement2	Measurement3	Δ_{ave}
10°	10.4936°	10.8881°	10.9805°	0.7874°
20°	19.4473°	20.1799°	19.7839°	0.3162°
21°	21.4050°	21.1369°	21.7478°	0.4299°
22°	21.9133°	21.7054°	22.2011°	0.1948°
23°	23.2480°	23.2721°	23.9472°	0.4891°
24°	23.6779°	25.4729°	24.2970°	0.6973°
30°	29.9870°	30.4661°	30.6004°	0.3598°

in Fig. 6.14 that packs beamforming IC and antenna elements into a single tile. Individual tiles can be connected with a scalable 3D microstrip to microstrip (3D-M2M) feeding network so that can be easily scaled up to large sized arrays. The 3D-M2M feeding network can be printed onto a flexible substrate so this phased array architecture can be applied to any arbitrary shape, and calibrated with the 3D depth camera method. These features make the this tiled phased array an ideal candidate for space-limited and power efficient 5G and satellite communication applications, and mmW Rx systems for multi-streaming with high throughput that require a large number of antenna arrays.

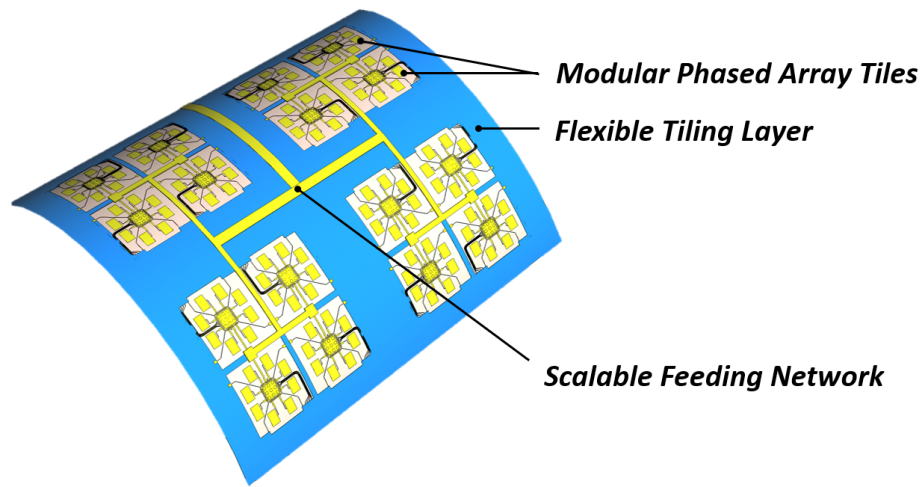


Figure 6.14: Concept demonstration of the conformal tile-based phased array architecture.

Single Tile Design

The single tile phased array consists of an Anokiwave AWS-0102 beamforming IC (BFIC) with 8 microstrip patch antenna elements on a Rogers 4350B substrate. The operating frequency range is defined by AWS-0102 BFIC which covers 17.7 GHz to 20.2 GHz for K-band SATCOM Rx radios. This BFIC has integrated individual amplifiers and phase shifter for each antenna port, the integrated micro controller can control the amount of attenuation (which controls the amount of amplification) and phase delay via an SPI interface. The design of the single tile is shown in Fig. 6.15, patch elements are fed from the edge and the feed lines are matched to $50\ \Omega$ impedance at 19.7 GHz. The BFIC is fed with a $50\ \Omega$ microstrip line and a grounding pad for the 3D-M2M transition. DC power connectors and SPI interface connectors are placed around the edge of the tile to ensure a strong bond between tiles and the tiling layer. Extra bonding points are also designed to create a even stronger inter-layer connection.

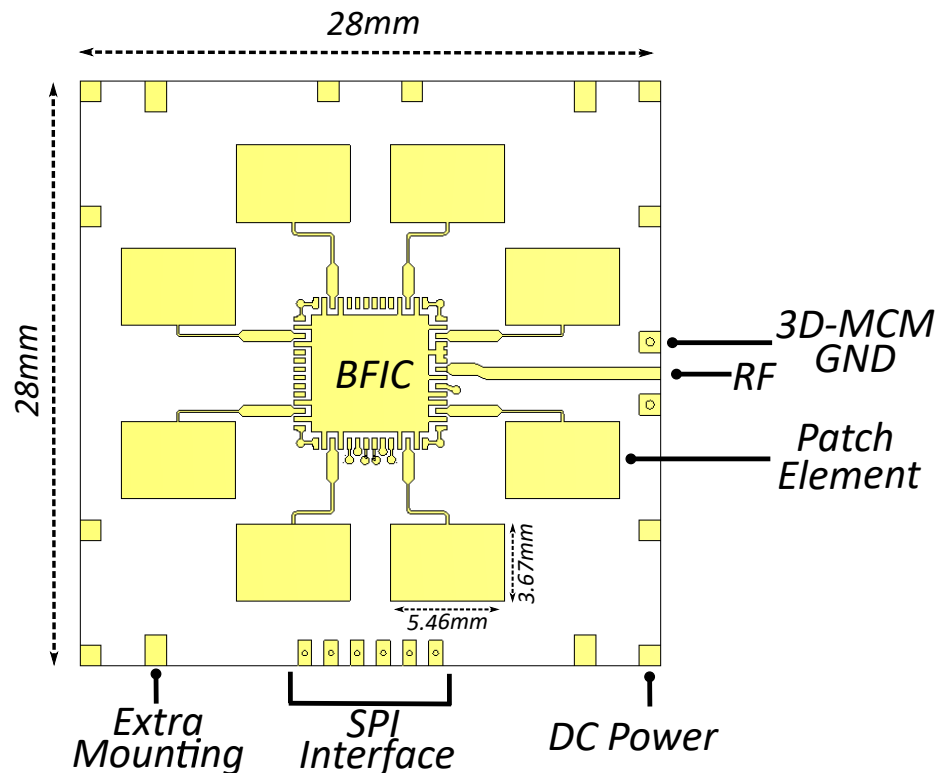


Figure 6.15: Design of a single tile

Single Tile Simulation

The single tile is designed and simulated in CST Microwave Studio. The dimension of the patch antenna elements are optimized as $5.46 \text{ mm} \times 3.67 \text{ mm}$ to have good performance at 19.7 GHz, the spacing between patch elements is also optimized for good radiation and low side lobe level (SLL) during beam steering. The simulated S_{11} and radiation pattern of each patch antenna element is shown in Fig. 6.16 and Fig. 6.17. The elements show very minimal frequency variation and good radiation performance. The averaged realized gain is 5.45 dBi and the averaged radiation efficiency at 19.7 GHz is -0.83 dB .

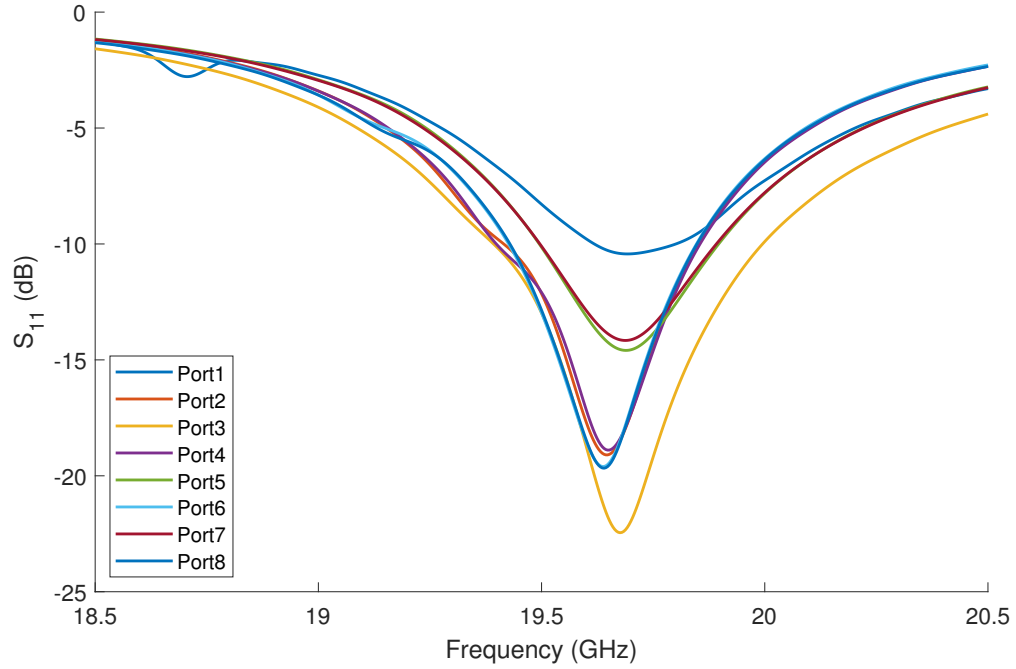


Figure 6.16: Simulated return loss of the single tile patch elements.

The BFIC on each tile has 8 individual phase shifters and power amplifiers, Fig. 6.18 shows the radiation pattern of the tile with all 8 patch elements turned on. The single tile achieved 12.7 dBi realized gain with -9.6 dB SLL at broadside. By tuning the phase shifters, the main beam can be steered from -30° to 30° with SLL varies from -9.6 dB to -4.5 dB . The summery of the single tile performance is shown in Table. 6.2.

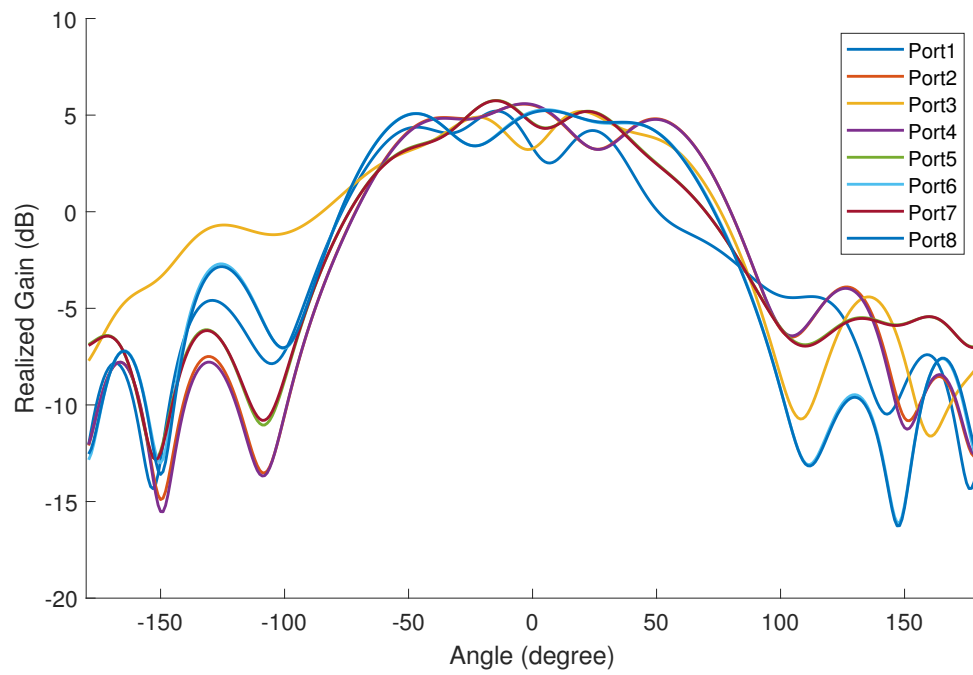


Figure 6.17: Simulated radiation pattern of the single tile patch elements.

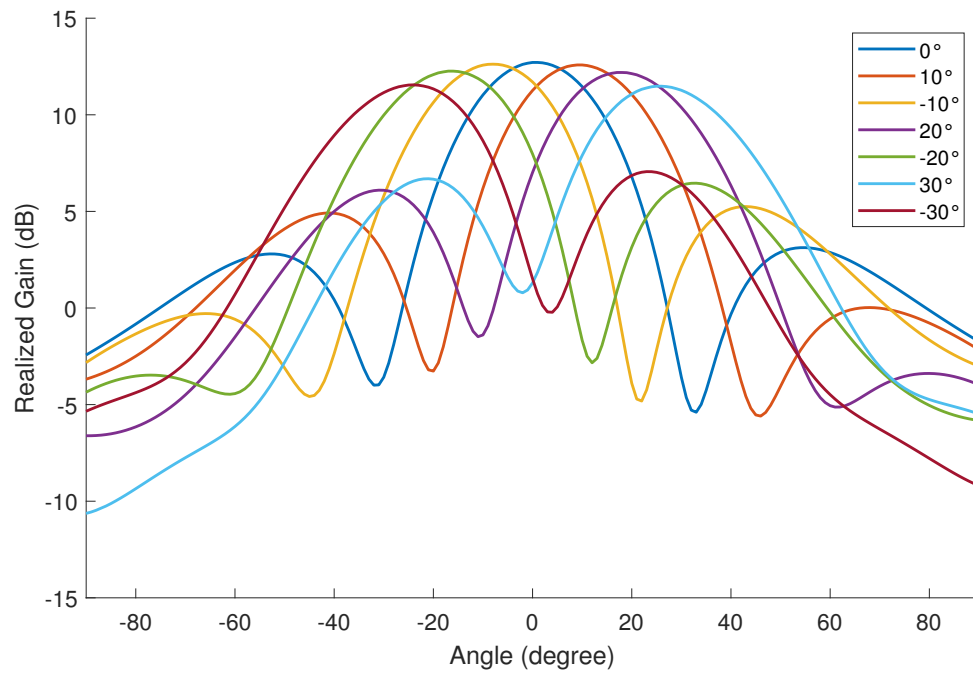


Figure 6.18: Simulated beam steering performance of the single tile.

Table 6.2:
Summery of the Single Tile Performance

Steering Angle	Realized Gain	SLL
$\theta = 0^\circ$	12.7 dBi	-9.6 dB
$\theta = 10^\circ$	12.6 dBi	-7.6 dB
$\theta = -10^\circ$	12.6 dBi	-7.6 dB
$\theta = 20^\circ$	12.2 dBi	-6.1 dB
$\theta = -20^\circ$	12.3 dBi	-5.8 dB
$\theta = 30^\circ$	11.5 dBi	-4.8 dB
$\theta = -30^\circ$	11.5 dBi	-4.5 dB

Tiling Layer Design

The tiling layer is used to attach the tiles to the feeding network and provides connections to the digital and DC interfaces such as SPI, VCC, and ground. The feeding network combines the RF out on each tile to a single output. All the ports are matched to $50\ \Omega$ by quarter-wavelength transformers. In this design, we are using Rogers 3003 flexible substrate to fabricate a tiling layer which contains two tiles. The angle between two tiles is rotatable and will be calibrated with the 3D depth camera method.

To attach each tile to the feedline, a novel 3D microstrip to microstrip (3D-M2M) transition is designed and utilized. Fig. 6.19 shows the 3D-M2M transition design between two microstrip lines, as well as a cross-section view of this structure. Two vias are placed aside the transmission line to connect ground planes of tiles and tiling layer. Square pads are added at the top of vias to reduce difficulty in soldering and provide higher stability. It has been reported that this structure can realize a low-loss and wide-band transmission [115].

Array Simulation

The 2-tile array is designed and simulated in CST Microwave Studio in two configurations: 0° and 15° rotation as shown in Fig. 6.20. The radiation pattern of 0° and 15° rotation cases are shown in Fig. 6.21. The 0° and 15° 2-tile array demonstrated 16 dBi and 14.7 dBi

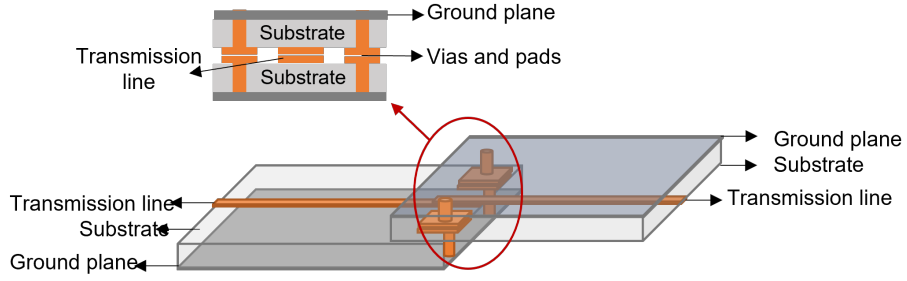


Figure 6.19: Microstrip-to-Microstrip transition.

realized gain, -11.1 dB and -8.3 dB SLL receptively at broadside, 10 dBi and 12.4 dBi realized gain, -0.6 dB and -4.9 dB SLL receptively at 60° direction. The beam steering ability of the 2-tile arrays are also simulated with steering angle from -60° to 60° . The summery of the beam steering performance is shown in Table. 6.3.

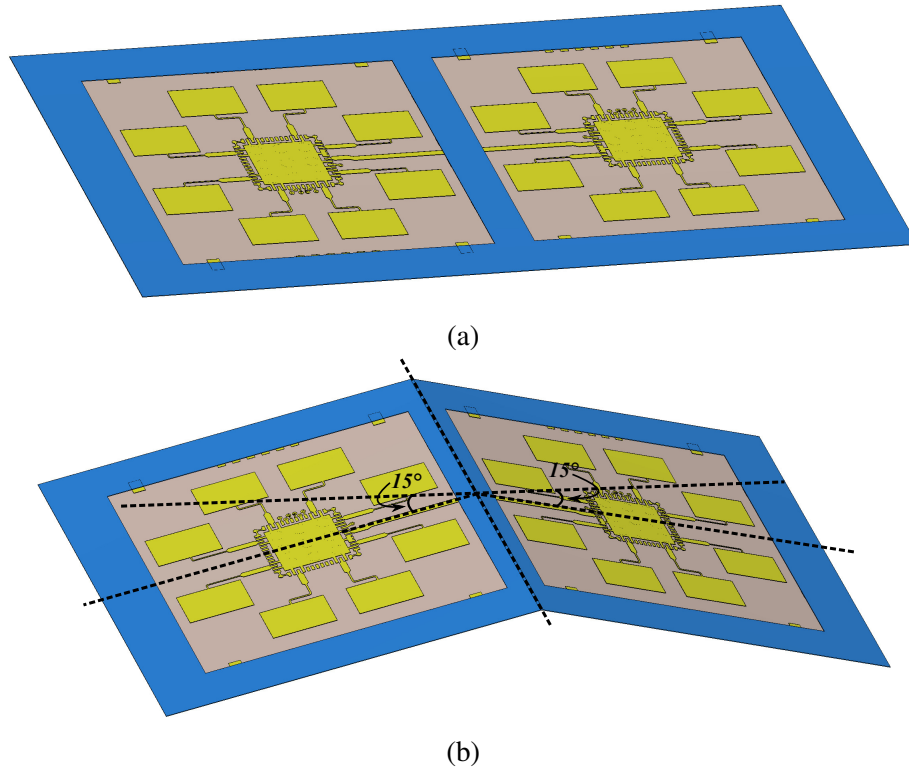
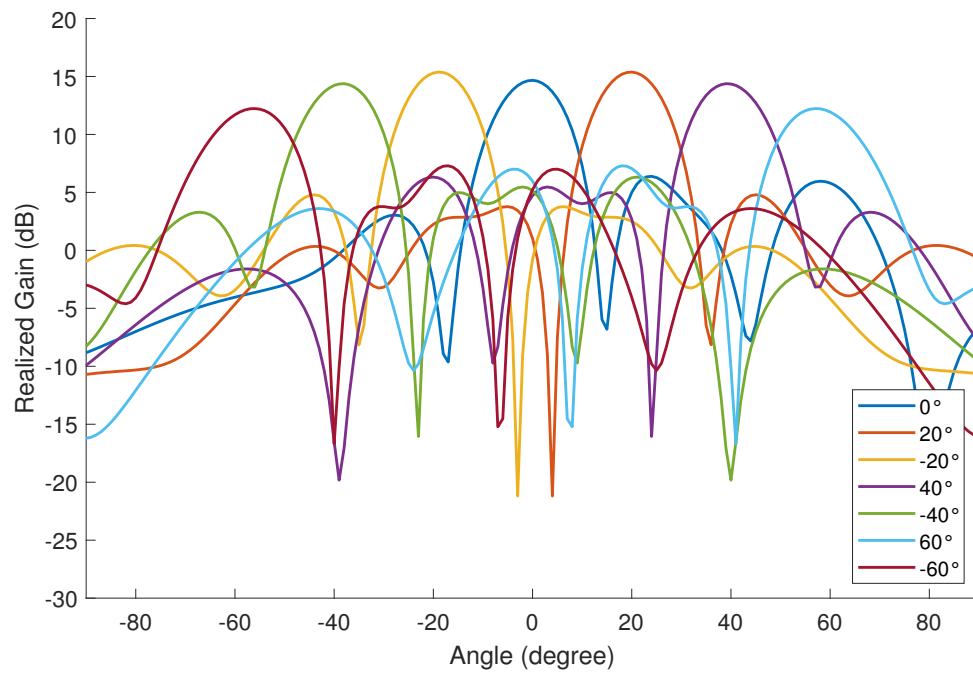
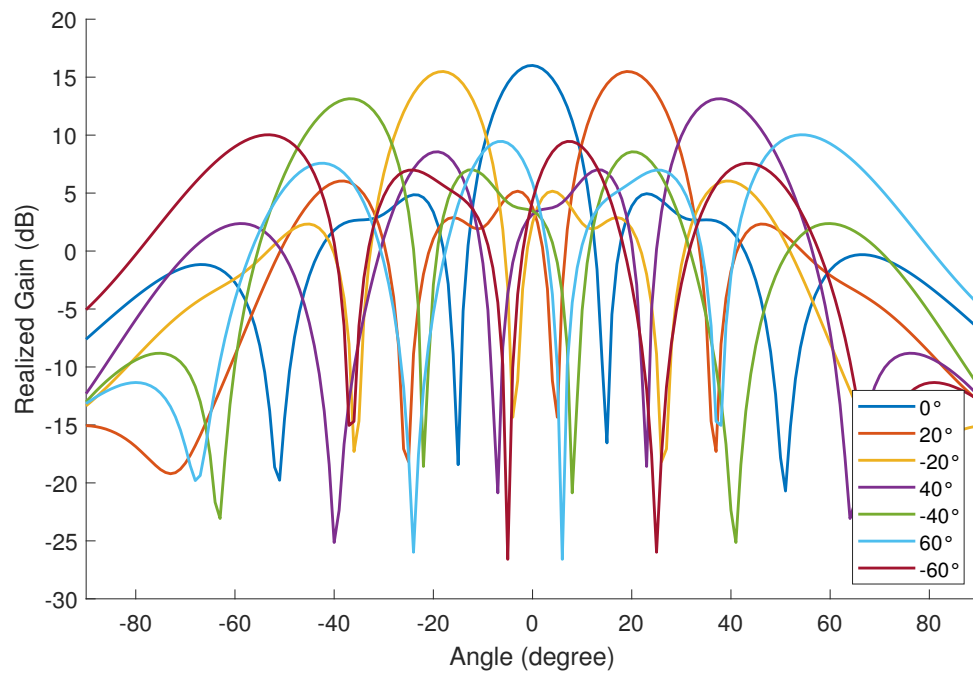


Figure 6.20: Two configurations of the 2-tile array design: (a) 0° rotation angle; (b) 15° rotation angle.



(a)



(b)

Figure 6.21: Simulated radiation patterns for different steering angles: (a) 0° rotation angle; (b) 15° rotation angle.

Table 6.3:
Summery of the 2-Tile Array Performance

Steering Angle	Realized Gain@0°	SLL@0°	Realized Gain@15°	SLL@15°
$\theta = 0^\circ$	16 dBi	−11.1 dB	14.7 dBi	−8.3 dB
$\theta = \pm 20^\circ$	15.5 dBi	−9.4 dB	15.4 dBi	−10.6 dB
$\theta = \pm 40^\circ$	13.1 dBi	−4.6 dB	14.4 dBi	−8.1 dB
$\theta = \pm 60^\circ$	10 dBi	−0.6 dB	12.4 dBi	−4.9 dB

CHAPTER 7

ADDITIONAL RESEARCH: A NOVEL 4-DOF WIDE-RANGE TUNABLE FREQUENCY SELECTIVE SURFACE USING ORIGAMI "EGGBOX" STRUCTURE

This chapter covers the additional work on novel origami-inspired "eggbox" structure that has more tunable dimensions than Miura-ori structure.

7.1 Introduction

Miura-ori is one of the most commonly used element structure in origami-inspired 3D FSS designs. Miura-ori FSS (M-FSS) features tunable equivalent electrical length and inter-element coupling by compressing from one side or changing the angle of incidence (AoI). Although compressing a Miura-ori FSS enables precise positioning by maintaining constant interspacing of elements along that axis, but it also removes a degree of freedom in the tuning parameters of an FSS device. Thus, the tunable range can be limited and insufficient in advanced ultra wideband (UWB) terrestrial and outer-space applications.

In this chapter, a novel tunable origami-inspired 3D FSS is presented using "eggbox" structure. The "eggbox" FSS can be tuned by compressing from two directions, or rotating from two axis. The multiple tuning methods enable a wider frequency tuning range. The prototype was fabricated with inkjet printing technique that is scalable, low-cost and fully additive. The measured sample shows wide-range frequency tunability, four degrees of freedom and two orthogonal linear polarizations.

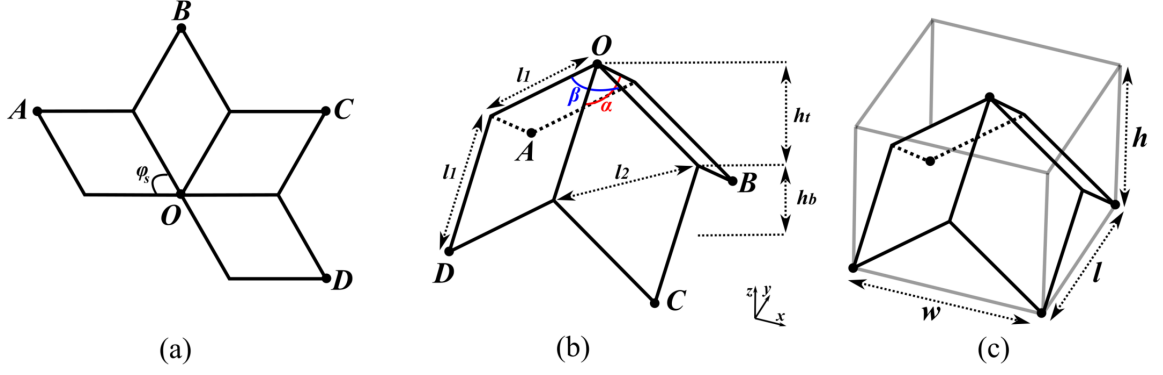


Figure 7.1: Eggbox element design: (a) 2D flat eggbox outline pattern; (b) 3D folded eggbox structure; (c) 3D folded eggbox volumetric boundary box.

7.2 Element Design

7.2.1 Mechanical Design

The “eggbox” is a non-developable structure which features additional degrees of freedom compare to widely used Miura-ori structure [116, 117, 118]. The design of an eggbox element is shown in Fig. 7.1b. The bi-directional symmetry nature of the eggbox enables the ability to compress the eggbox structure from two orthogonal directions, in this case, x axis and y axis. The size of the eggbox is defined by two lengths l_1 and l_2 . The compressing angles along y axis and x axis are defined by α and β . When the eggbox is not compressed, α and β will be equal, which can be calculated by (7.1).

$$\alpha = \beta = \theta_0 = 2 \times \arccos\left(\sqrt{1 - \frac{l_2^2}{2l_1^2}}\right) \quad (7.1)$$

When the eggbox is compressed, the relation between the two folding angles α and β can be calculated by (7.2) or (7.3).

$$\alpha = 2 \times \arccos\left(\left(\frac{1}{\cos \frac{\beta}{2}}\right) \times \left(1 - \frac{l_2^2}{2l_1^2}\right)\right) \quad (7.2)$$

$$\beta = 2 \times \arccos\left(\left(\frac{1}{\cos \frac{\alpha}{2}}\right) \times \left(1 - \frac{l_2^2}{2l_1^2}\right)\right) \quad (7.3)$$

The unfolded eggbox unit element is shown in Fig. 7.1a, the sector angle φ_s can be calculated by (7.4)

$$\varphi_s = \arccos\left(\frac{2l_1^2 - l_2^2}{2l_1^2}\right) \quad (7.4)$$

The volumetric parameters of an eggbox unit element is shown in Fig. 7.1c where the overall dimensions w , l , and h can be calculated by (7.5), (7.6), and (7.7) respectively.

$$w = 2l_1 \sin(0.5\beta) \quad (7.5)$$

$$l = 2l_1 \sin(0.5\alpha) \quad (7.6)$$

$$h = l_1 \cos(0.5\alpha) + l_1 \cos(0.5\beta) \quad (7.7)$$

To ensure a good foldability and ease of fabrication, the eggbox configuration in this work is optimized to be $l_1 = 20\text{mm}$, $l_2 = 20\text{mm}$, $\alpha(\text{unfolded}) = 110^\circ$, $\beta(\text{unfolded}) = 110^\circ$. The variation of different geometric parameters with different folding angles α is shown in Fig. 7.2 which presents the folding/compressing process of the eggbox structure.

7.2.2 RF Design

For proof-of-concept verification, the substrate utilized in this work is $110\mu\text{m}$ thick cellulose paper. The material is characterized resulting dielectric constant (ϵ_r) of 3.4 at 7.5 GHz with a loss tangent ($\tan \delta$) of 0.015.

To ensure a significant frequency tunability and take full advantage of the eggbox structure with added degrees of freedom, a cross dipole shaped conductive pattern is utilized. Cross dipole FSS element has been well studied over the years showing enhanced bandwidth, dual linear polarizations and ease of fabrication [1, 119, 120, 121, 122]. Literature

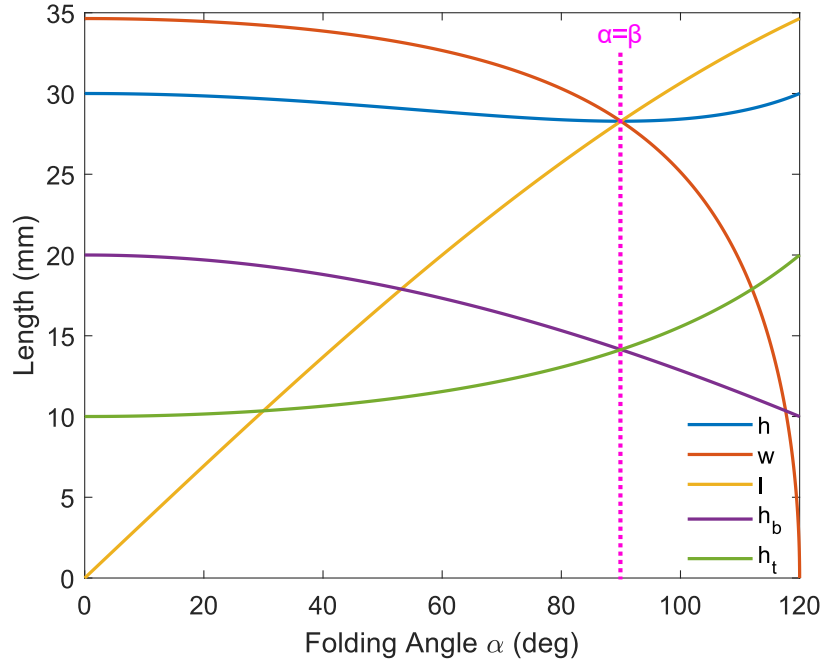


Figure 7.2: The variation of different geometric parameters with folding angles α from 0° to 120° .

[8] explores the possibility of integrating cross dipole element onto Miura-ori based FSS, showing improved tunability and bandwidth.

The eggbox FSS element shown in Fig. 7.3 is designed and simulated in CST Studio Suite 2019 with unit cell boundary condition and Floquet port excitations with the frequency domain solver. The unit cell boundary condition simulates only one singular FSS element and extrapolates to an infinite sheet. The size and distribution of the cross dipole element is optimized to ensure a great range of tunable frequencies and S_{21} performance. The center frequency is designed at 7.5 GHz with optimized cross dipole dimensions of $l_c = 15$ mm and $w_c = 3.5$ mm. The simulated frequency response will be presented and discussed in Section. III with the measurement results.

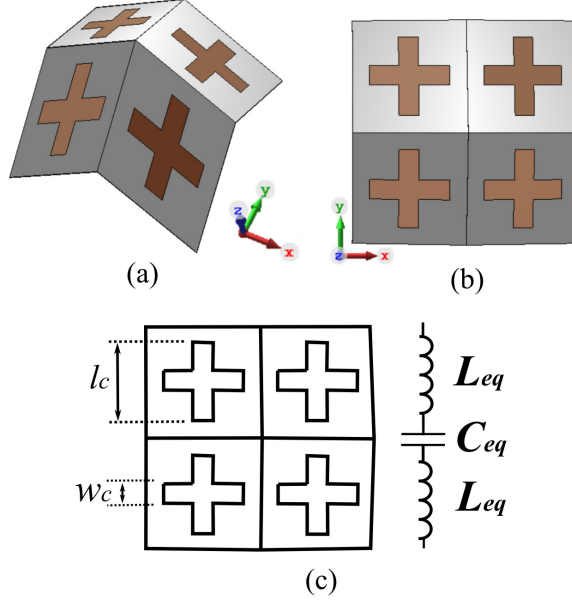


Figure 7.3: Design of cross-dipole eggbox FSS element: (a) perspective view; (b) top view; (c) equivalent circuit.

7.3 6×6 Eggbox FSS Design

7.3.1 Mechanical Simulation

As a proof-of-concept demonstrator, a 6×6 “eggbox” FSS with cross-shaped resonating elements is employed in this work. The centre frequency is designed at 7.5 GHz. The length of the FSS can be compressed from 170 mm ($\alpha = \beta = \theta_0 = 110^\circ$) down to 37 mm ($\alpha = \beta = 22^\circ$). The angle of incidence (AoI) can be customized from 0° to 30° . The design takes advantage of the bidirectional symmetry nature of the eggbox structure, tuning both orthogonal polarizations.

When compressing along the x -axis (as shown in Fig. 7.4), the decreased equivalent inductance of the horizontally faced branches, increase the resonant frequency of the horizontally polarized waves. The increased equivalent capacitance of the vertically faced branches, decrease the resonant frequency of the vertically polarized waves. Compressing along y -axis will in contrast decrease the horizontally polarized frequency and increase vertically polarized frequency.

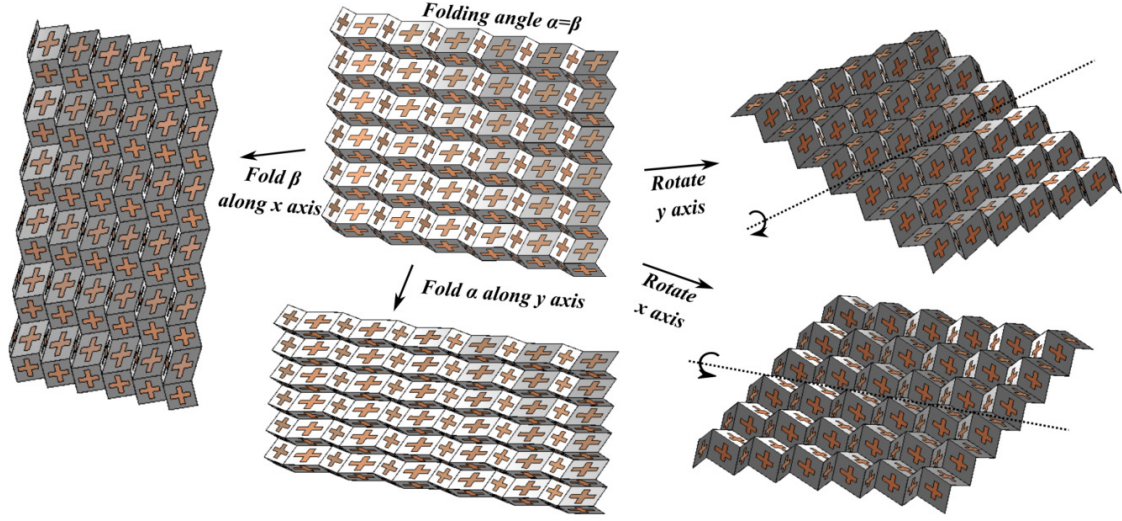


Figure 7.4: Demonstration of four degrees of freedom tuning methodology: fold along x axis; fold along y axis; rotate x axis; rotate y axis.

When rotating the structure along the x-axis, the increased equivalent inductance of the horizontally faced branches, decrease the resonant frequency of the horizontally polarized waves. Rotating along y-axis will in contrast decrease the vertically polarized frequency.

7.3.2 Fabrication

Unlike the Miura structure, the eggbox is a non-developable structure that cannot be folded out of a single planar paper sheet. Therefore, to realize the eggbox with paper-based substrate, we will utilize cuts and folds of individual eggbox FSS elements which are then adhered together. In this case, the manual fabrication process is durable and accurate enough for this proof-of-concept demonstration. To further improve the fabrication process, hybrid printing can be a faster and more accurate way to manufacture a scalable and durable eggbox FSS.

The print-fold-attach fabrication process shown in Fig. 7.5 is utilized to realize the eggbox FSS prototype consists of a 6×6 array of individual cells. First, a folding pattern for the individual eggbox cell was designed in a 2D CAD software. The 2D drawing accounts for the conductive traces, the folds, and an additional polygon to glue the edges

that enable linking of the elements together that can be easily printed with an office laserjet printer. Then, the cross dipole pattern will be printed onto the flat eggbox outline with a Dimatix DMP-2831 inkjet printer utilizing Suntronic EMD5730 silver nanoparticle (SNP) ink (Sigma-Aldrich). Cellulose paper inherently tends to absorb the conductive ink, thus, ten layers of SNP ink is printed to ensure a exceptional conductivity and flexibility. After printing, the substrate will be thermally cured at 140 °C for 1 h to sinter the SNP ink. Finally, to realize the eggbox 6×6 matrix, each folded structure was attached together by glue. The entirety of the 6×6 matrix of elements can be seen in Fig. 7.6, with an approximate length and width of 170 mm \times 170 mm in its uncompressed state.

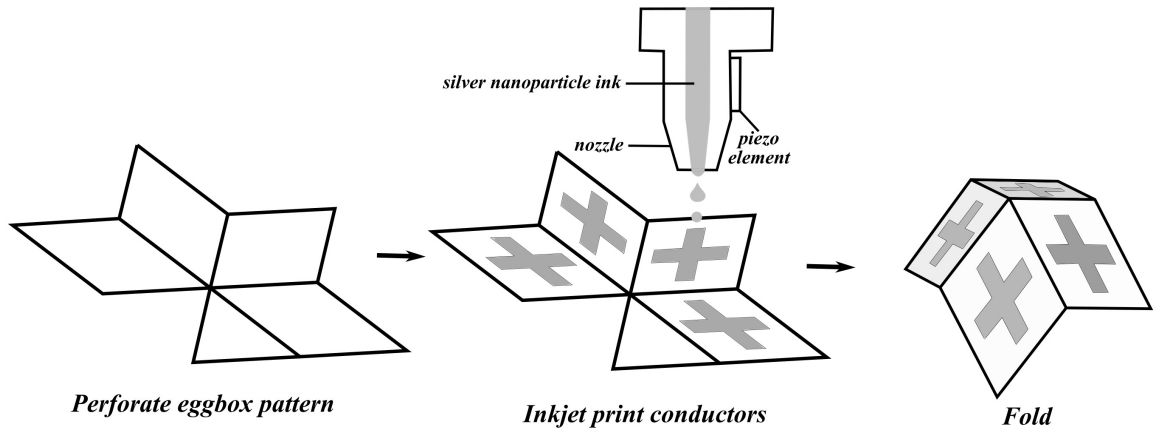


Figure 7.5: Three-step fabrication process for eggbox FSS: perforate eggbox pattern; inkjet print conductive traces; fold to 3D eggbox structure.

7.3.3 Simulation and Measurement Results

In order to measure the fabricated prototype, two horn antennas (A-INFOMW LB-20245-SF) were placed equidistant with 1.5 meter spacing, with the results measured on an Anritsu MS46522B VNA set to measure from 6 GHz to 9 GHz. The 6×6 eggbox structure is placed equidistant between the horn antennas. The eggbox structure was compressed for different angles α and β , and the length and width of the eggbox after various compressions enables determination of the fold angles α and β , which are then compared to the simulated results.

The simulated and measured insertion loss of the eggbox FSS for horizontal polariza-

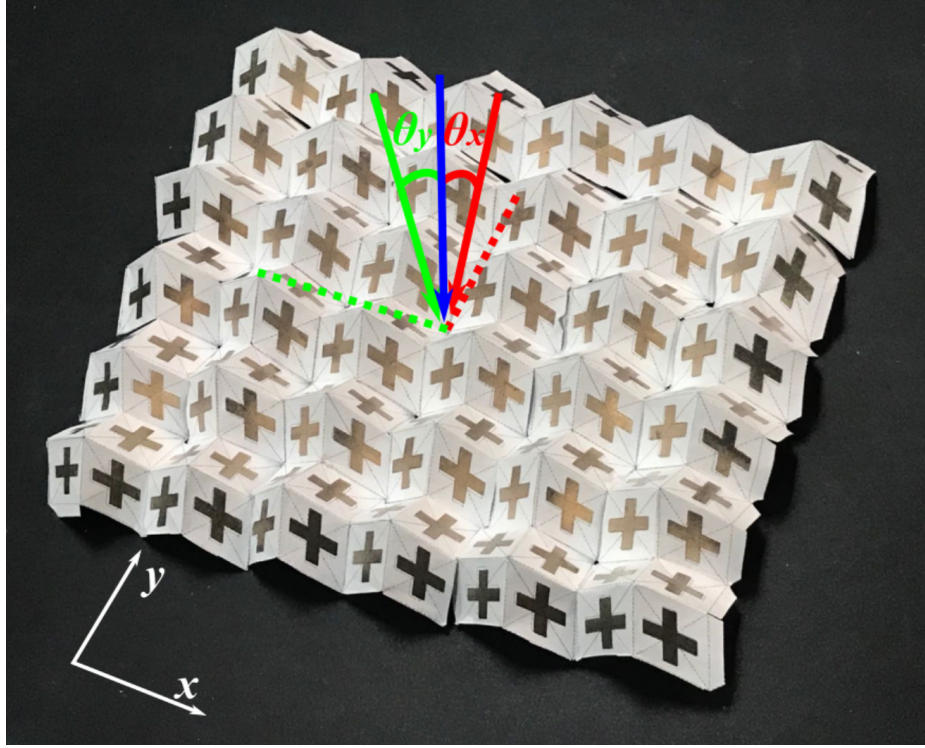


Figure 7.6: Fabricated sample of 6×6 cross-dipole eggbox FSS and incidence angles: normal incidence (blue), rotate y axis (green), rotate x axis (red).

tion (along x -axis) with different folding angles is shown in Fig. 7.7. From this figure, the resonant frequency of the metamaterial shifts higher as the folding angle β decreases. This is due to the reduced effective length of the horizontal branch of the cross element due to folding, which in turn causes a reduction of the inductance. On the other hand, the resonant frequency of the origami meta-material shifts lower as the folding angle α decreases. The result of this is due to the folding along the y -axis reducing the gap between the horizontal components of the metamaterial, leading to an increased capacitance that reduces the resonant frequency. The vertical polarization response is demonstration in Fig. 7.8. In this scenario, as the folding angle of β decreases, the frequency reduces due to the increase capacitance. If the folding angle α is reduced, the frequency of the resonant response increases due to a reduced inductance. Note that the amount of frequency shifting varies depending on the folding direction and polarization. For example, it can be seen that the folding angle β has an increased impact to the response of the system along the horizontal

polarization. Similarly, along the folding angle α has a larger impact of the response in the vertical polarization along the y-axis. The measured resonance frequency versus folding angles ($0.2\theta_0$ to θ_0) of horizontal polarization is shown in Fig. 7.9, the measured fractional bandwidth is 25%.

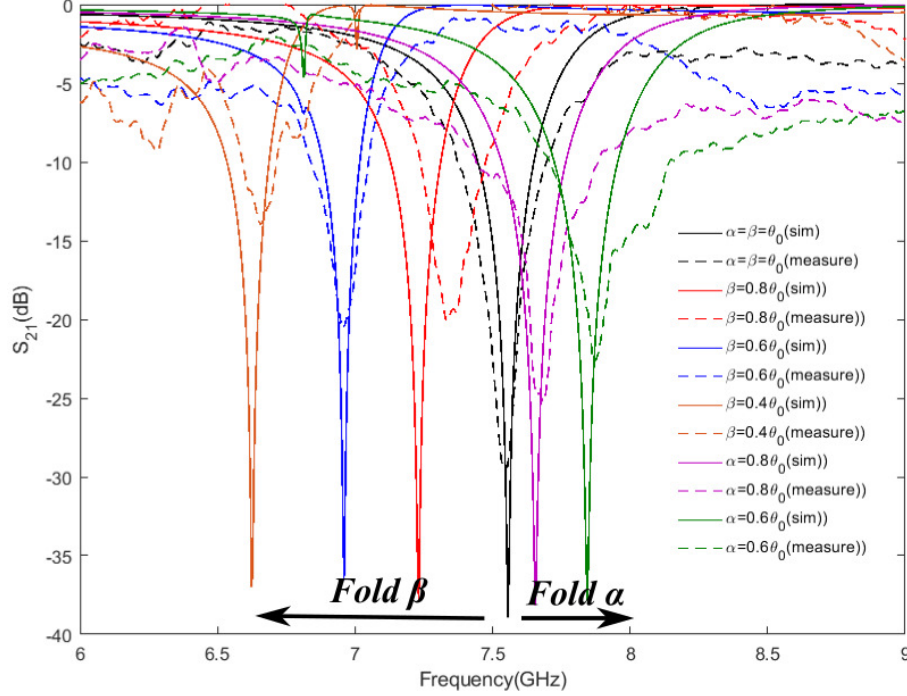


Figure 7.7: Horizontal (x-axis) polarization with different folding angles simulation and measurement results.

The simulated and measured insertion loss of the eggbox FSS for horizontal polarization (along x-axis) with different y-axis rotating angle θ_y is shown in Fig. 7.10. The resonant frequency of the eggbox FSS decreases as the rotating angle θ_y increases. This is due to the expanded effective length of the vertical branch of the cross element due to folding, which in turn causes a increase of the inductance. On the other hand, in Fig. 7.11, the resonant frequency of the horizontal branch shifts lower as the rotating angle θ_x increases.

There are some mismatches between the simulation and measurement results especially the amplitude of the insertion loss. This is because the simulation setup uses unit cell boundary condition in CST, which considers the FSS as infinitely large. The unfolded 6×6 eggbox FSS (170 mm \times 170 mm) will cover the whole antenna aperture which can

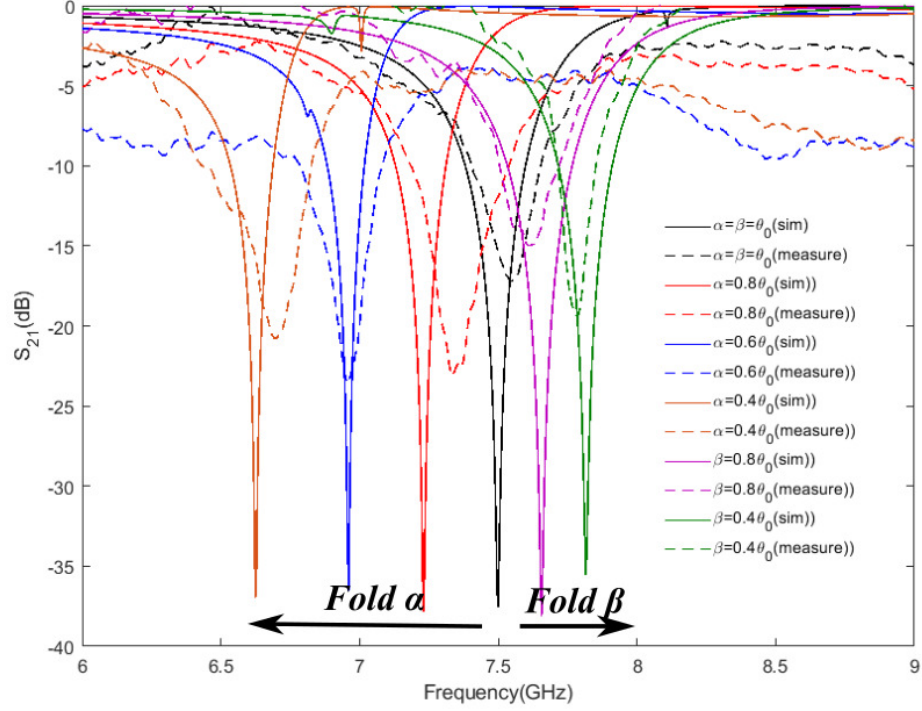


Figure 7.8: Vertical (y-axis) polarization with different folding angles simulation and measurement results.

be considered as infinity large. However, when we compress or rotate the structure, the size of the eggbox FSS can reduce to $37 \text{ mm} \times 170 \text{ mm}$ which cannot cover the entire illuminating antenna beamwidth anymore, causing leakage that reduces the insertion loss performance.

The measured performance of the eggbox FSS design presented in this paper is compared with state-of-art origami FSSs at is shown in Table. 7.1. The proposed design demonstrates widest tunable range, dual linear polarizations and 4-DOF tunability.

Table 7.1: Performance comparison of typical origami inspired FSS

Work	Type	Pattern	Freq Tunable Range	Polarization
[2]	Miura	Dipole	12.8%	Linear
[4]	Miura	Dipole	13.5%	Linear
[11]	Miura	Cross	19%	Dual-linear
This Work	Eggbox	Cross	25%	Dual-linear 4-DOF-tunable

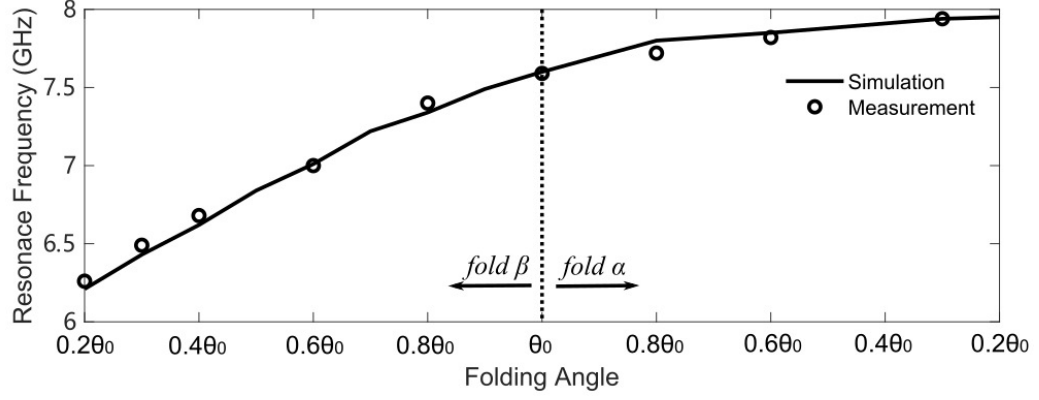


Figure 7.9: Resonance frequency versus folding angles of horizontal polarization (x-axis)

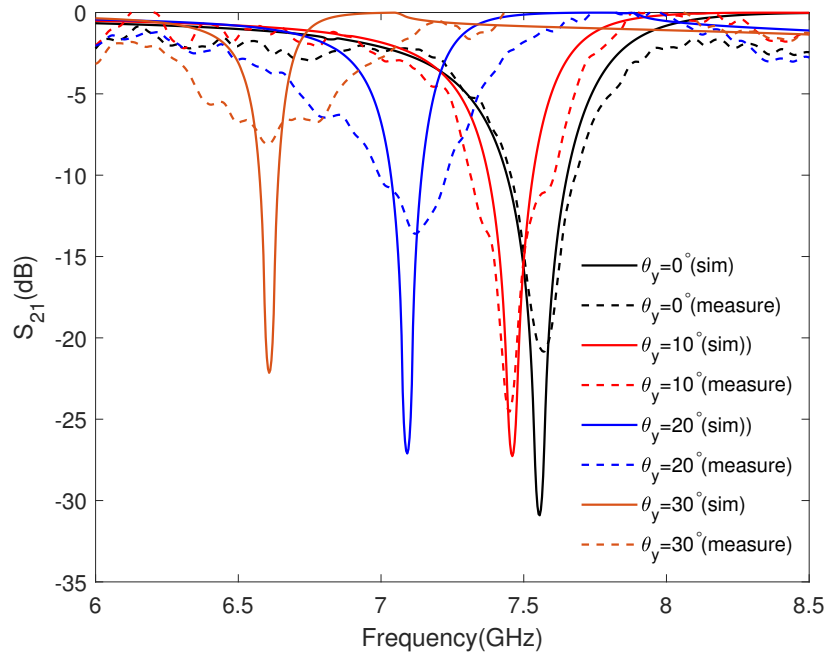


Figure 7.10: Horizontal polarization (x-axis) with different y-axis rotating angles simulation and measurement results.

7.4 Summary

This chapter covers the additional work of a novel tunable eggbox-based origami 3D FSS. The eggbox structure enables two foldable directions and two rotatable axis to tune the resonant frequency. The measured results show a wide range of frequency control of 25% fractional bandwidth. The fabrication of individual cells without the use of active devices

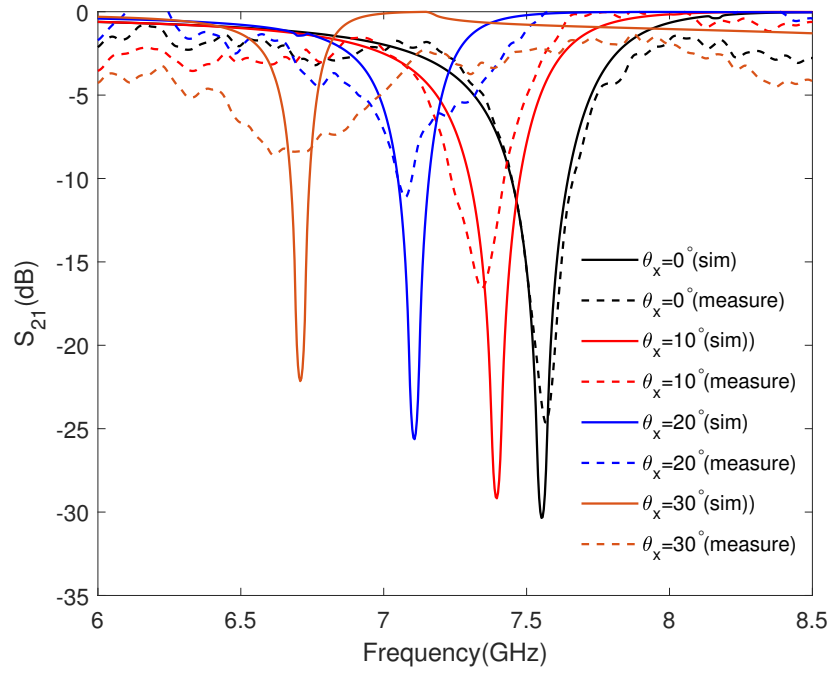


Figure 7.11: Vertical polarization (y-axis) with different x-axis rotating angles simulation and measurement results.

enables easy scalability by allowing many individual elements to be fabricated and then assembled in any desired configuration. By changing the type of substrate, or fabricate with the hybrid printing process, the design can be applicable for remote sensing, RFID, 5G, and mm-wave applications.

CHAPTER 8

ADDITIONAL RESEARCH: 3D-PRINTING AND CHARACTERIZATION OF POLYTETRAFLUOROETHYLENE (PTFE) DEMONSTRATING EXTREMELY LOW LOSS MM-WAVE DIELECTRIC REFLECTARRAYS

This chapter covers the additional work on discovering and characterizing the first 3D printable low-loss material for RF applications.

8.1 Introduction

With the development of 5G/6G technologies and the exponential growth of mobile devices, a wide set of additive manufacturing technologies are adopted in the fabrication of RF devices [123, 124]. To achieve designs similar to traditional circuit board, fabrication techniques such as ink-jet printing, aerosol jet printing, and direct write technologies can be utilized to deposit practically anything in a liquid form, from high conductivity silver nanoparticle inks and silver/gold/copper electroless solutions, to various dielectrics such as SU-8, BCB, polyimide, acrylate epoxies, etc [125]. Homogeneous polymer 3D printing is the most widespread technology to rapidly fabricate complex 3D structures with commonly used 3D printing technologies include fused deposition modeling (FDM) and stereolithography (SLA), enabling novel microwave and photonic devices including microwave and photonic metamaterials such as gradient index Luneburg lenses, mm-wave packaging, dielectric lenses, etc [123, 124, 126, 61, 127, 128, 129].

However, there is a major challenge. Most additive manufacturing processes and materials are optimized for mechanical purposes first, and have no or little consideration for electrical properties. This becomes particularly important as the frequency of operation increases to mm-wave and beyond for SATCOM and next generational communication networks, the loss tangent of these polymers and particle mixtures in the aforementioned

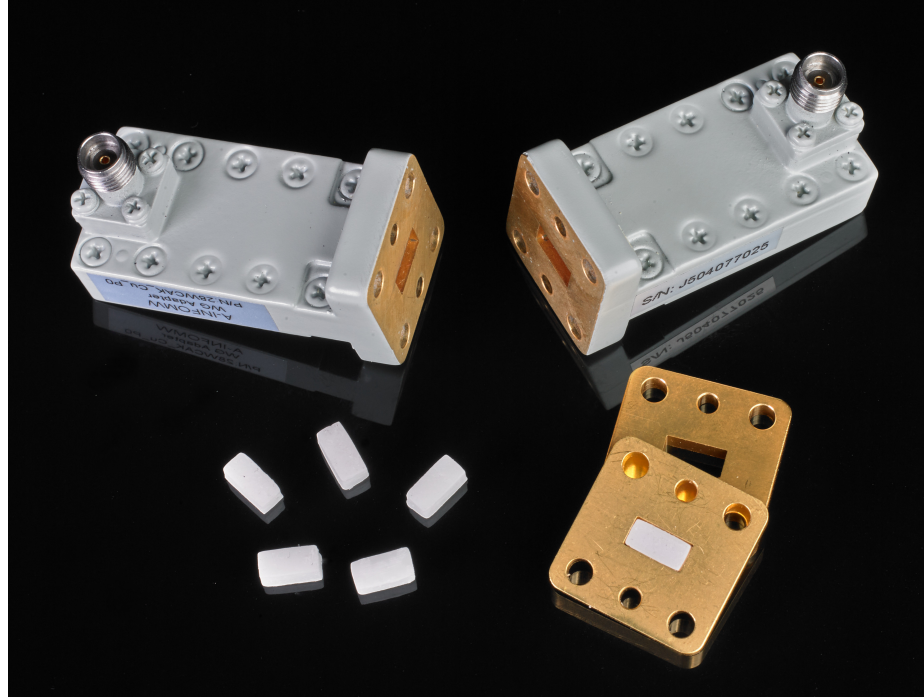
additive manufacturing techniques can cause significant performance losses in a microwave system. The loss of an antenna directly correlates to its efficiency, impacting the transceiver design by affecting the receiver signal-to-noise ratio (SNR) ratios as well as transmitter emitted power. The intersection of high performance materials for mm-wave purposes and ideal mechanical properties intertwine occasionally. Unfortunately, for general SLA resins at this time, those properties do not intertwine as far as dielectric properties, where the $\tan \delta$ varies between 0.02 to 0.04 [130]. This is because the resins themselves tend to contain polar molecules, and the increase of dielectric losses is caused by an amount of the molecules not fully cross linked after the fabrication process. Although the cross-linking can be improved through methods such as heating and UV exposing the polymer during the final curing process, the dielectric loss is still the major limiting factor for the RF performance.

Within this chapter, the 3D printed Polytetrafluoroethylene (PTFE) is reported with the lowest loss achieved by stereolithography technology. This work was a collaboration with 3M who has been developing a 3D printing process for PTFE. We performed a broadband material characterization for the SLA PTFE with Nicolson-Ross-Weir (NRW) method [131] from 26 GHz to 40 GHz. To compare the results, we also characterized a variety of commercially available 3D printing materials including FDM materials such as Ultimaker PLA, ABS; and SLA materials such as Formlabs Clear, High Temp, Flexible 80A. To demonstrate the real-life performance advantages from the low-loss material, we designed and fabricated two mm-wave dielectric reflectarray antennas utilizing SLA PTFE and Formlabs Clear. The dielectric reflectarray antennas feature a “hollow” unit cell structure that is suitable for SLA printing, and a flat profile for easy transportation and implementation. The measurement result confirms the high performance of the SLA PTFE and the applicability to mm-wave designs for modern RF devices and systems.

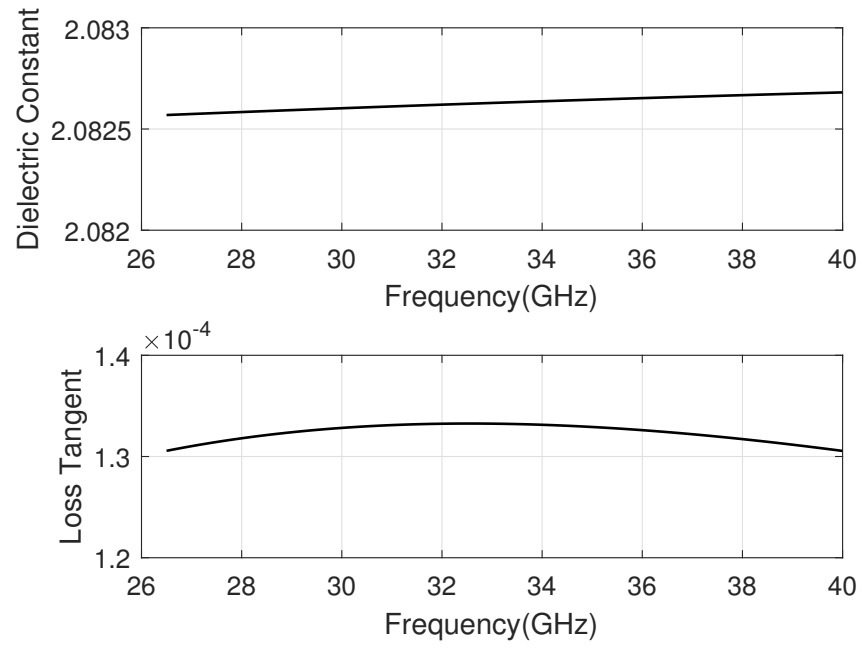
8.2 3D Printing and Characterization of PTFE

Many materials with low loss tangents tend to be ceramics and polymers that are chemically inert, such as alumina and polytetrafluoroethylene (PTFE). This tends to make them difficult to utilize within SLA systems where a chemical reaction is utilized for the solidification of materials. Custom 3D printing stereolithography resins can be designed by loading polymer resin with particles. For example, Tethon3D Porcelite porcelain-based material [132] is created in this manner. Additionally, the manufacturing needs to be adjusted heavily depending on the light absorbing properties of the print, as the Tethon 3D Porcelite resin had to be exposed by more than $5\times$ the amount of energy compared to the MadeSolid Vorex Orange in our tests [133]. Additionally, the polymer matrix must be removed in post-processing in order to get the dielectric properties of the loaded material. This leads to many challenges, including requiring a firing oven that can achieve 1260°C . Not only that, due to how the layers are deposited, the part will often shrink anisotropically, usually at a different rate in the Z direction. This can be compensated by scaling the model before printing along the correct axis. However, the entire process of fine tuning the material recipe to reach reliable printing properties, firing properties, correction due to firing, and verifying the dielectric performance can become an extremely challenging task. In that sense, a collaboration was set up with 3M who have been developing a 3D printing process for PTFE.

To utilize 3D printing materials in RF designs and simulations, the materials need to have their dielectric properties characterized. To characterize the dielectric properties, $7.11\text{ mm} \times 3.56\text{ mm} \times 3.00\text{ mm}$ samples were made for Ka-band waveguides to be measured from 26.5 GHz to 40 GHz with measurement setup shown in Figure. 8.1a. In order to capture the expected extremely low loss of the SLA PTFE, higher precision waveguides (with additional alignment pins) and a short-short-load-through (SSLT) calibration kit (A-INFO 28CLKA2-KRFRF-P0 WR28) were utilized for this measurement. Two samples



(a)



(b)

Figure 8.1: (a) Material calibration measurement setup with WR28 waveguide to coaxial adapter, $1/4\lambda$ spacer, and test samples; (b) measured SLA PTFE dielectric constant and loss tangent from 26.5 GHz to 40 GHz.

were stacked in two shims to prevent inaccuracies in the NRW method that result from samples that may be $\lambda_{effective}/2$ in thickness. After calibration, typical SLA PTFE properties were determined to be $\epsilon_r = 2.08$, $\tan \delta = 0.00013$ across 26.5 GHz to 40 GHz, nearly identical to bulk PTFE. The broadband result is shown in Figure. 8.1b. The extreme flatness of the relative permittivity is ideal for designing true time delay devices to enable high-bandwidth phased arrays by reducing beam squint, a phenomena due to phase error within the operational bandwidth.

We also characterized various 3D printing materials including SLA materials such as Formlabs Clear V4, Formlabs High Temp V2, and FDM materials such as Ultimaker Blue-ABS, Ultimaker Transparent PLA. The FDM samples were printed on Ultimaker S3 3D printer with Ultimaker AA 0.4 nozzle. The “Zig Zag” infill pattern was utilized with 100 % infill density. However, even with 100 % infill density, air gaps may still exist within the printed samples. So the characterization results for FDM materials are subject to the print settings, the value of the ϵ_r and $\tan \delta$ will be lower than the actual bulk materials. The characterization results are shown in Table. 8.1. It becomes apparent that most 3D printable materials exhibit significant loss, with most materials having a $\tan \delta$ of greater than 0.005, and high resolution SLA resins with a $\tan \delta$ greater than 0.017. With this, there is a potential to have significant performance enhancement when a low loss dielectric is utilized in 3D printed RF designs.

Table 8.1: Material Properties of Commonly Used SLA and FDM Materials

Material	Typical ϵ_r	Typical $\tan \delta$	Frequencies
SLA PTFE	2.08	0.00013	26.5 to 40 GHz
SLA Formlabs Clear V4	2.9	0.017	26.5 to 40 GHz
SLA FormLabs High Temp V2	2.8	0.018	26.5 to 40 GHz
SLA FormLabs Flexible 80A	2.8	0.05	26.5 to 40 GHz
FDM Ultimaker Blue ABS	2.6	0.005	26.5 to 40 GHz
FDM Ultimaker Transparent PLA	2.6	0.008	26.5 to 40 GHz

8.3 Extremely Low Loss mm-Wave Dielectric Reflectarrays

A reflectarray is a high-performance antenna system widely used in satellite communication, radar, and navigation applications. It combines the advantages of both parabolic reflectors and phased arrays with high gain, low profile, low cost, and ease of fabrication [78]. Dielectric reflectarray (DR) is a new type of reflectarray that uses dielectric elements to achieve phase control, eliminating the conductor losses caused by the metallic phase shifters in traditional reflectarray designs [134, 135, 136]. The phase control of DR is typically achieved by varying the height or thickness of the dielectric slabs, which makes DR designs ideal for fabrication with 3D printing technology to reduce cost and turnaround time. However, as discussed in Section. 2, most SLA dielectrics have a loss tangent above 0.017, which can absorb a significant amount of energy from the excitation waves. For example, in [134], up to -2.60 dB return loss was observed within the full 360° phase cycle with dielectric loss of 0.04, which means nearly half of the power could be forfeited by the dielectric losses. Thus, in this section, we compare two identical DR designs fabricated with the traditional SLA material Formlabs Clear and the new SLA PTFE to demonstrate the real-life performance benefits from the low-loss dielectric.

8.3.1 Unit Cell Design and Simulation

To conform to the design rules of SLA PTFE [137], instead of using solid blocks, we modified the design in [138] to be utilized as the unit cell structure. The dimension of the unit cell shown in Figure. 8.2 is defined by the element length l , angle α , wall thickness t , and element height h . This “hollow” unit cell design reduces per-layer area when printed on an SLA 3D printer, improving the printability as well as the print quality. The phase control is realized by changing the wall thickness t instead of changing the element height h , which ensures the array with a flat-surface design, reducing the inter-element radiation blockage.

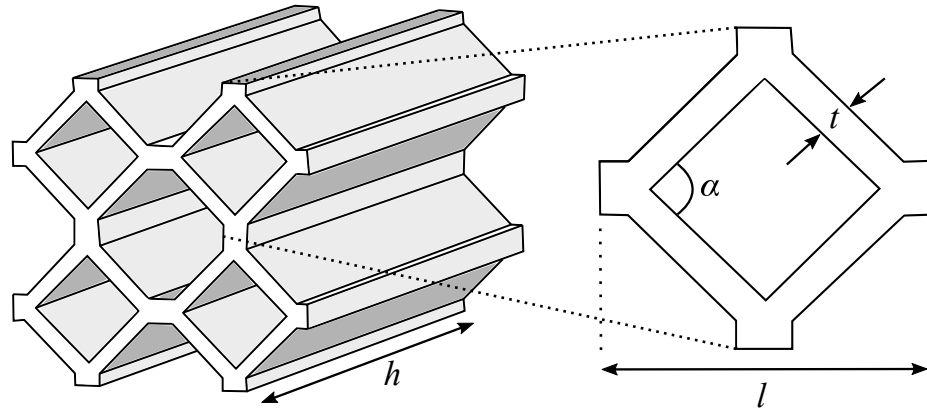


Figure 8.2: Unit cell design: four elements perspective view, single element top view. ($h = 28$ mm, $l = 6$ mm, $\alpha = 90^\circ$, $t = \text{variable}$)

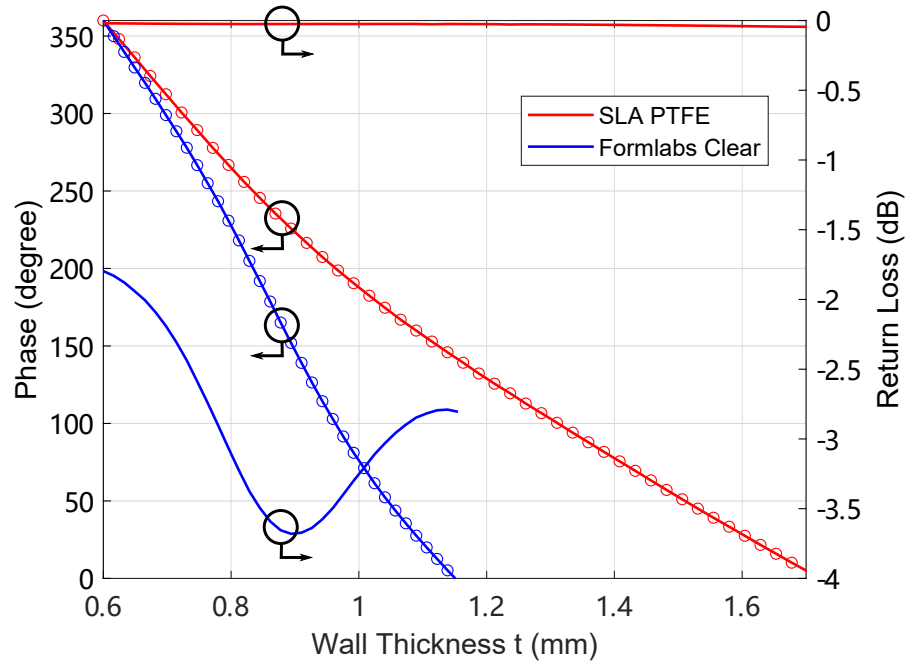


Figure 8.3: Unit cell simulation results for SLA PTFE and Formlabs Clear: phase vs wall thickness, return loss vs wall thickness.

The unit cell was designed and simulated in CST Studio Suite 2020 with the frequency domain solver and unit cell boundary conditions. The simulation results are shown in Figure. 8.3. The data was extracted and post processed in MATLAB with a linear interpolative curve fitting algorithm to ensure any desired phase value can be matched with a precise wall thickness t .

By varying the wall thickness t from 0.6 mm to 1.7 mm, a full 360° phase cycle can be achieved with SLA PTFE with a maximum return loss of -0.04 dB. For Formlabs Clear material, the full 360° phase cycle can be achieved by varying t from 0.6 mm to 1.1 mm, with a maximum return loss of -3.68 dB. A 3.64 dB improvement is observed from the unit cell simulation by replacing Formlabs Clear with SLA PTFE.

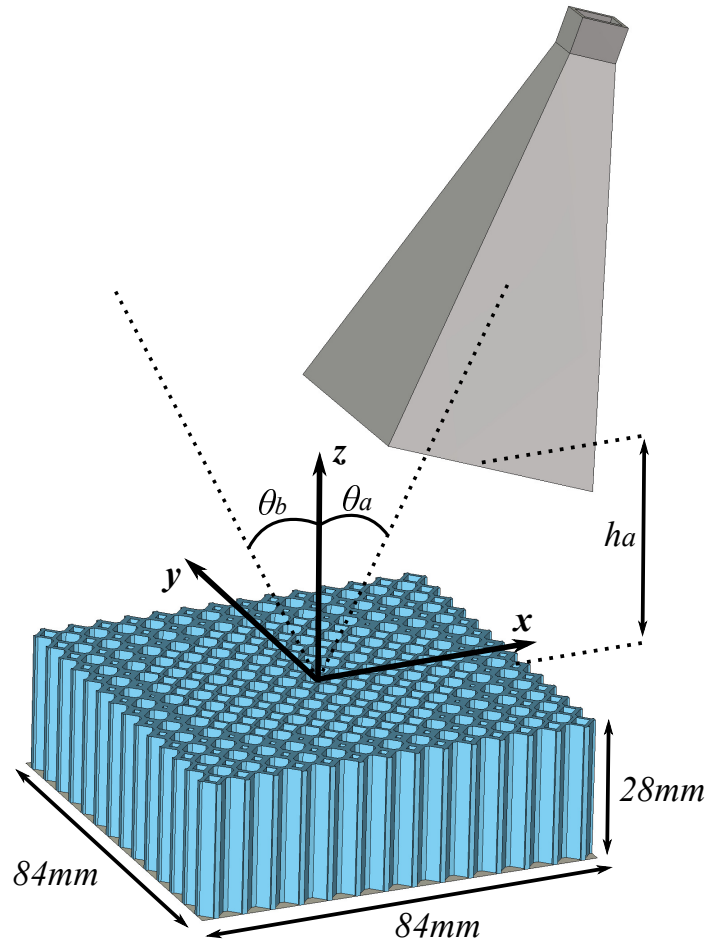


Figure 8.4: Proposed DR configuration ($\theta_a = \theta_b = 20^\circ$, $h_a = 80$ mm).

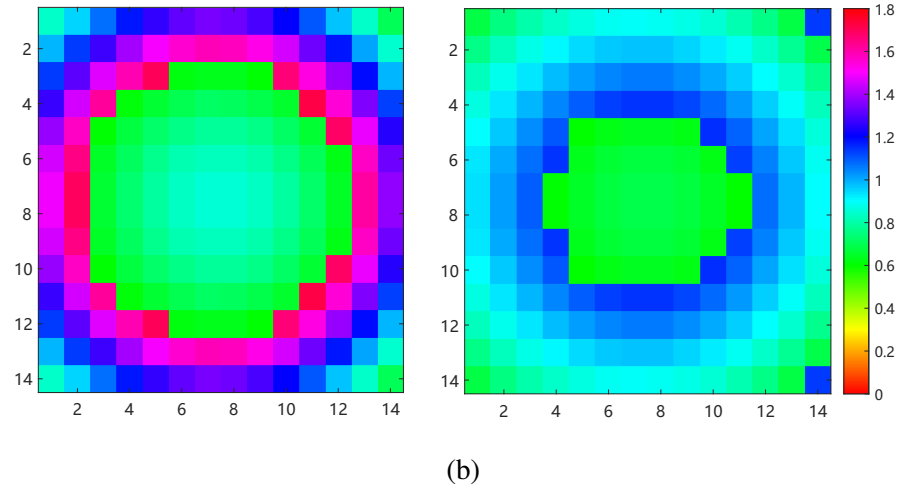
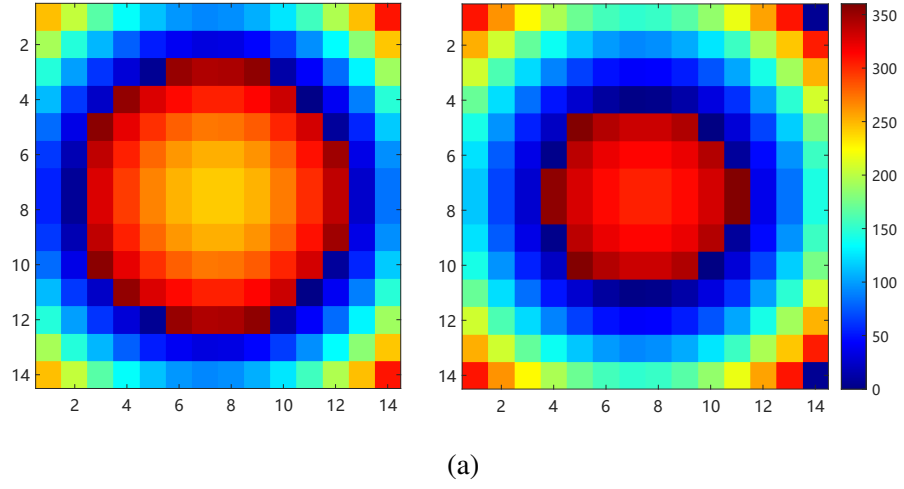


Figure 8.5: (a) Phase control patterns for SLA PTFE DR (left) and Formlabs Clear DR (right); (b) wall thickness distribution patterns for SLA PTFE DR (left) and Formlabs Clear DR (right).

8.3.2 Array Design

The ideal phase control value $\phi(x_i, y_i)$ at a given position (x_i, y_i) is given by (8.1), (8.2).

$$\phi(x_i, y_i) = k_0(d_i - (x_i \cos(\varphi_b) + y_i \sin(\varphi_b)) \sin(\theta_b)) \quad (8.1)$$

$$d_i = \sqrt{(x_i - h_a \sin(\theta_b))^2 + y_i^2 + (h_a \cos(\theta_b))^2} \quad (8.2)$$

where k_0 is the propagation constant in vacuum; d_i is the distance between feed horn phase center and element i ; φ_b is the main beam steering angle with respect to azimuths angle φ ; θ_b is the main beam direction with respect to elevation angle θ ; θ_a is the excitation horn antenna offset angle with respect to elevation angle θ ; h_a is the height of the excitation horn antenna. The proposed DR configuration is shown in Figure. 8.4, we set $\varphi_b = 0^\circ$; to avoid beam blockage and beam squint, we set $\theta_b = \theta_a = 20^\circ$; considering the beamwidth of the excitation horn antenna, we set $h_a = 80$ mm. The center frequency of this work is set to 40 GHz.

In this work, the arrays are designed with a dimension of $84 \text{ mm} \times 84 \text{ mm}$ with 14×14 elements. The dimension of this design is limited by the size of the 3D printer's build plate area, but larger 3D printers are commercially available for larger array designs. The calculated phase control patterns are shown in Figure. 8.5a. The 3D models of the arrays were generated in CST 2020 with a VBA script. The patterns for wall thickness t are shown in Figure. 8.5b. The arrays were evaluated with full-wave simulation in CST 2020 with frequency domain solver. The simulation results will be discussed in Section. 8.3.3.

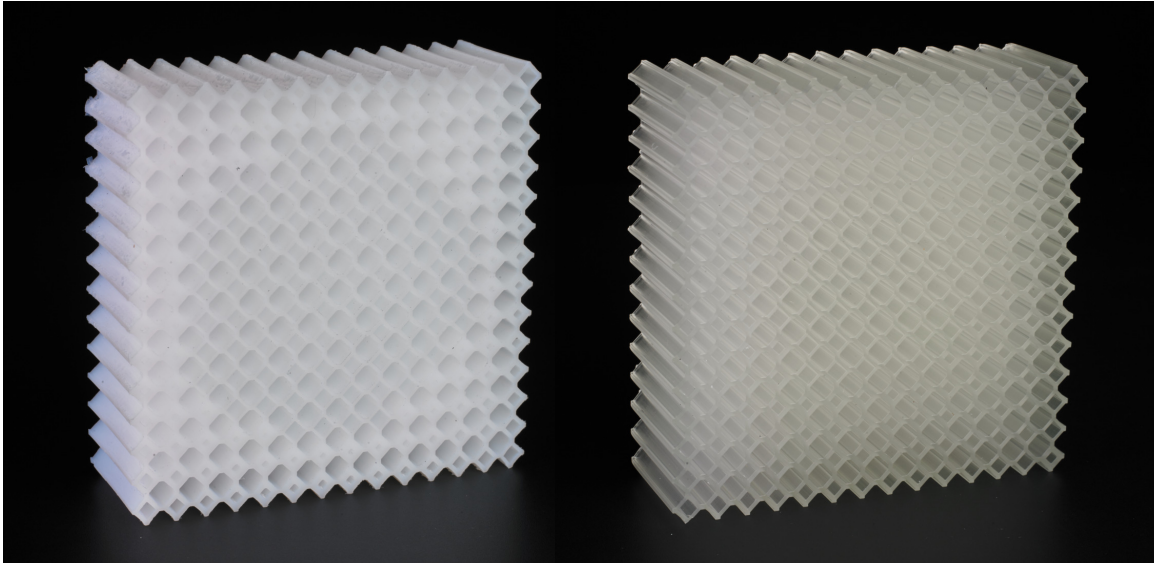


Figure 8.6: Fabricated prototypes: SLA PTFE DR (left), Formlabs Clear DR (right).

8.3.3 Fabrication, Results, and Discussion

As discussed in Section. 8.2, the SLA PTFE DR prototype was designed and fabricated by 3M. For the Formlabs Clear DR prototype, we printed the design on Formlabs Form 3 3D printer. To ensure the best consistency and accuracy, the printed sample was washed in 99 % isopropyl alcohol (IPA) to remove the extra resin left on the surface. Then the sample was post processed with Formlabs Form Cure UV curing system, with 60 min exposure under 405 nm UV lights at 60 °C. The fabricated samples of SLA PTFE DR and Formlabs Clear DR are shown in Figure. 8.6.

The radiation pattern and gain measurement setup for the DR samples are shown in Figure. 8.7. The array is held by a 3D printed frame with a rotatable arm set to $\theta_a = 20^\circ$. Two A-INFO LB-180400-20-C-KF wideband horn antennas were utilized, one as the excitation, and the other one as the receiver. The distance between the DUT and the receiver was set to 2.0 m. The gain of each DR was measured and calculated with the three-antenna method [139].

The simulated and measured radiation pattern for SLA PTFE DR is shown in Figure. 8.8a, the realized gain in simulation is 26.4 dB and measures 26.1 dB. The sidelobe level

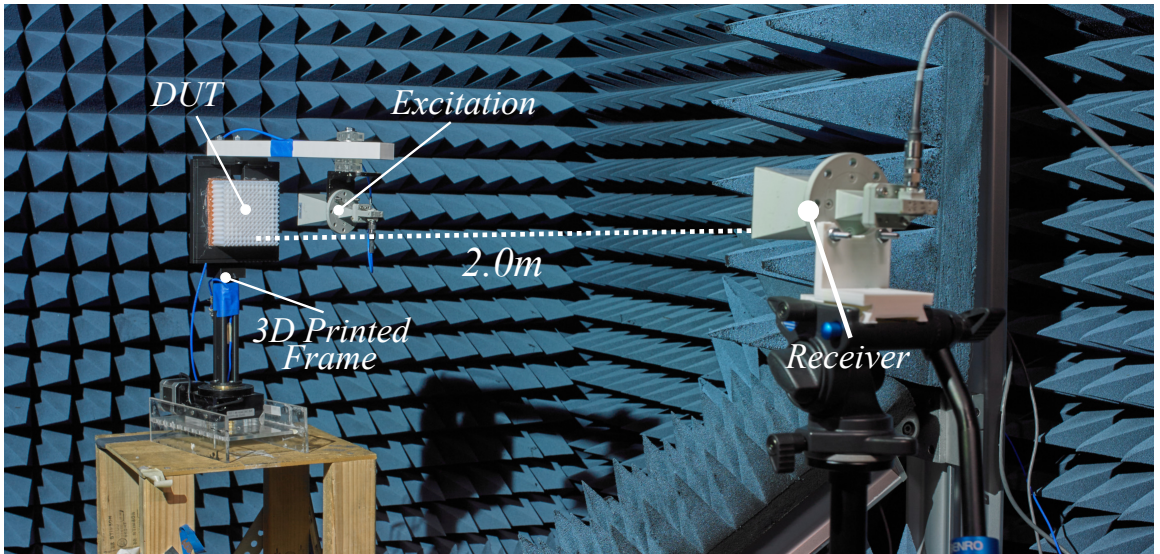
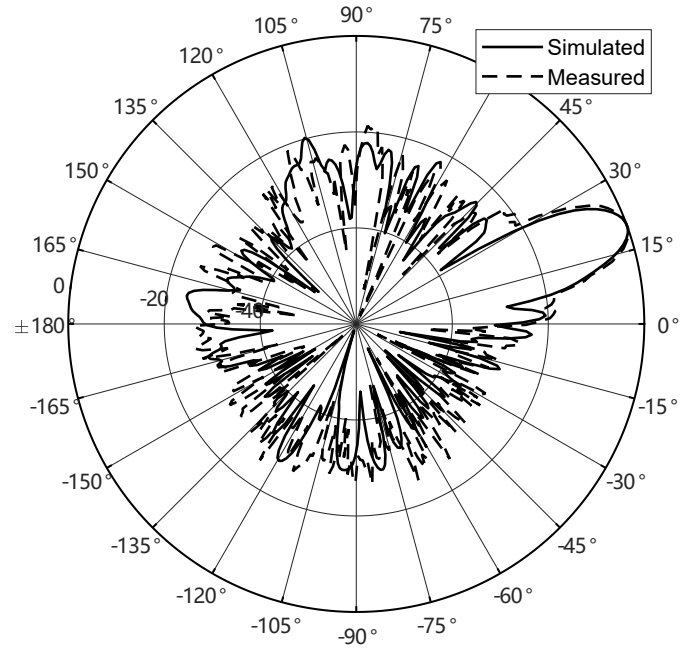
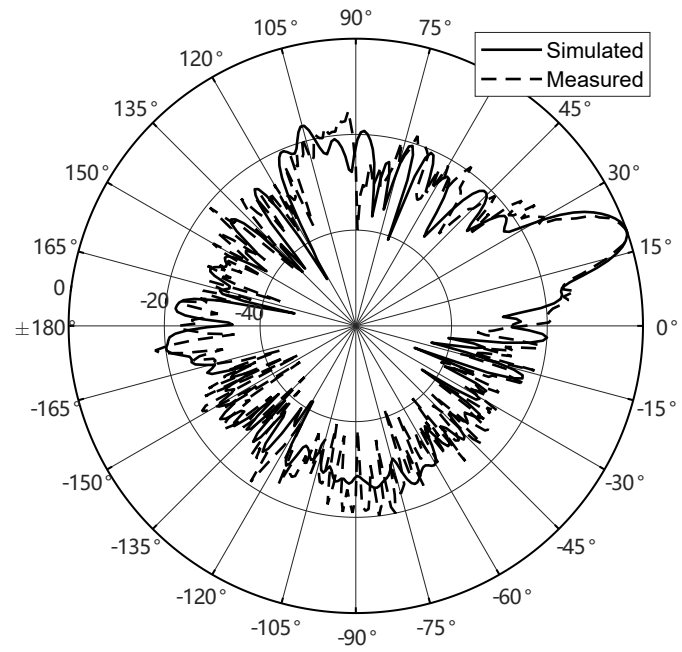


Figure 8.7: Radiation pattern and gain measurement setup in an anechoic chamber.



(a)



(b)

Figure 8.8: Simulated and measured radiation patterns at 40 GHz: (a) SLA PTFE DR; (b) Foamlabs Clear DR.

(SLL) in simulation is -19.8 dB and measures -18.7 dB. The simulated and measured radiation pattern for Formlabs Clear DR is shown in Figure. 8.8b, the realized gain in simulation is 22.2 dB and measures 22.0 dB. The SLL in simulation is -16.4 dB and measures -15.0 dB. The SLL performance is affected by the resolution of the 3D printer. If the long tube-shape structures realized thickness become thicker than designed, the side lobe levels will be impacted. Despite the slight discrepancies on the SLL level, the simulation and measurement match well for both DR designs.

The key performance comparison between the SLA PTFE DR and the Formlabs Clear DR is shown in Table. 8.2. From the measured results, the SLA PTFE DR shows 4.1 dB better realized gain and 3.7 dB better SLL. In addition, the half power beam width (HPBW) of the SLA PTFE DR is 3.8° wider. These results confirm the significant performance improvements with the low-loss SLA PTFE material, enabling a new generation of prototyping dielectric microwave devices.

Table 8.2: Measured Performance of the SLA PTFE DR and Formlabs Clear DR

Sample	Unit Cell Return Loss	Realized Gain	SLL	HPBW
SLA PTFE	-0.02 dB to -0.04 dB	26.1 dB	-18.7 dB	7.4°
Formlabs Clear	-1.8 dB to -3.7 dB	22.0 dB	-15.0 dB	11.2°

8.4 Summary

This chapter cover the characterization of the extremely low loss 3D printed PTFE up to Ka-band with electrical properties that are identical to bulk PTFE, which has orders of magnitude better than commonly used FDM and SLA 3D printable materials. This leads to the design and fabrication of extremely low loss mm-wave designs, such as Luneburg lenses or, as demonstrated, a high-performance dielectric reflectarray. The SLA PTFE DR demonstrated remarkable 4.1 dB realized gain improvement and 3.7 dB SLL improvement over an identical design fabricated with Formlabs Clear material, a representative of common 3D printable acrylate photopolymers. The SLA PTFE truly enables the possibility of

designing and fast prototyping the next-generation RF devices.

CHAPTER 9

CONTRIBUTIONS AND POTENTIAL FUTURE WORKS

9.1 Contributions

The objective of this research is to design and realize high-performance shape-changing microwave devices for 5G and mm-wave applications utilizing additive manufacturing techniques. Toward the proposed research objective, new origami-inspired structures with small form factor, exceptional tunability, and foldability are designed to expand the applicable scenarios for 5G and mm-wave applications, and new AM fabrication processes are developed. Some of the novel aspects of the research are highlighted below:

9.1.1 Fabrication Improvement

- Developed a hybrid printing fabrication process to realize complex flexible shape-changing RF structures.
- Characterized various FDM and SLA 3D printing materials, including Formlabs FLGR02 and Flexible 80A at mm-wave frequencies.
- Characterized the surface profile of 3D printed substrate, tested the number of inkjet printed SU-8 layers needed to reduce the surface roughness.
- Developed a low temperature gradient sintering process to cure inkjet printed silver nanoparticle inks on 3D printed substrate, dramatically improved conductor quality and flexibility.
- Characterized the first 3D printed PTFE with loss tangent more than $100\times$ lower than SLA printed dielectrics.

9.1.2 Novel Shape-changing RF Designs

- Demonstrated the first origami-inspired shape-changing reconfigurable FSSs at mm-wave frequencies in both single-layer and multi-layer configurations.
- Realized a wireless large-area pressure sensor enabled by a novel “sandwich-like” substrate structure with tunable hinges, and a metamaterial-based conductive pattern.
- Realized a wireless small-area pressure sensor enabled by a novel SIW based structure with tunable Voronoi insert.
- Designed and realized the first origami-inspired FSS using novel “eggbox” structure that can be tuned from two directions with two tunable polarizations.
- Demonstrated the first origami-inspired high-performance antenna: a dielectric reflectarray antenna with high gain, low SLL, deployability, and beam scan ability from -30° to 30° .
- Designed and realized the first 3D printed PTFE dielectric reflectarray antenna, demonstrated 4 dBi gain compared to an identical design with typical SLA material.
- Proposed a novel conformal phased array calibration method: utilizes 3D depth camera to scan the surface of the array, extract the element location information with computer vision program.
- Designed a true conformal phased array system using tile-based phased array architecture with a flexible tiling layer.

9.2 Potential Future Works

9.2.1 Fabrication Improvement

- To further improve the conductor flexibility for better bending/flexing range, new conductive inks such as silver nano wire should be experimented and characterized.

- To fabricate even smaller 3D structures for THz applications, Pixdro LP50 dual-printhead inkjet printer can be a potential solution to build both the dielectric and conductor at the same time layer-by-layer in μm resolution.

9.2.2 Novel Shape-changing RF Designs

- To improve the applicable scenarios for the 3D depth camera conformal phased array calibration process, more advanced computer vision and machine learning techniques can be utilized to map more complicated surfaces.
- With the 3D depth camera conformal phased array calibration process, more shape-changing origami-inspired phased arrays can be developed with more mechanical tuning and electrical tuning capabilities.

REFERENCES

- [1] B. Munk, *Frequency selective surfaces: theory and design*. John Wiley, 2000.
- [2] G. I. Kiani, K. L. Ford, L. G. Olsson, K. P. Esselle, and C. J. Panagamuwa, "Switchable frequency selective surface for reconfigurable electromagnetic architecture of buildings," *IEEE Transactions on Antennas and Propagation*, vol. 58, no. 2, pp. 581–584, 2010.
- [3] H. Fabian-Gongora, A. E. Martynyuk, J. Rodriguez-Cuevas, and J. I. Martinez-Lopez, "Active dual-band frequency selective surfaces with close band spacing based on switchable ring slots," *IEEE Microwave and Wireless Components Letters*, vol. 25, no. 9, pp. 606–608, 2015.
- [4] X. G. Huang, Z. Shen, Q. Y. Feng, and B. Li, "Tunable 3-d bandpass frequency-selective structure with wide tuning range," *IEEE Transactions on Antennas and Propagation*, vol. 63, no. 7, pp. 3297–3301, 2015.
- [5] C. Mias, "Varactor-tunable frequency selective surface with resistive-lumped-element biasing grids," *IEEE Microwave and Wireless Components Letters*, vol. 15, no. 9, pp. 570–572, 2005.
- [6] J. P. Gianvittorio, J. Zendejas, Y. Rahmat-Samii, and J. W. Judy, "Mems enabled reconfigurable frequency selective surfaces: Design, simulation, fabrication, and measurement," in *IEEE Antennas and Propagation Society International Symposium (IEEE Cat. No.02CH37313)*, vol. 2, 2002, 404–407 vol.2.
- [7] B. Schoenlinner, A. Abbaspour-Tamijani, L. C. Kempel, and G. M. Rebeiz, "Switchable low-loss rf mems ka-band frequency-selective surface," *IEEE Transactions on Microwave Theory and Techniques*, vol. 52, no. 11, pp. 2474–2481, 2004.
- [8] K. Fuchi, J. Tang, B. Crowgey, A. R. Diaz, E. J. Rothwell, and R. O. Ouedraogo, "Origami tunable frequency selective surfaces," *IEEE Antennas and Wireless Propagation Letters*, vol. 11, pp. 473–475, 2012.
- [9] S. A. Nauroze, A. Eid, and M. M. Tentzeris, "N-rim: A paradigm shift in the realization of fully inkjet-printed broadband tunable fss using origami structures," in *2018 IEEE/MTT-S International Microwave Symposium - IMS*, 2018, pp. 51–54.
- [10] S. A. Nauroze, L. Novelino, M. M. Tentzeris, and G. H. Paulino, "Inkjet-printed "4d" tunable spatial filters using on-demand foldable surfaces," in *2017 IEEE MTT-S International Microwave Symposium (IMS)*, 2017, pp. 1575–1578.

- [11] A. Biswas, C. L. Zekios, and S. V. Georgakopoulos, "Transforming single-band static fss to dual-band dynamic fss using origami," *Scientific Reports*, vol. 10, no. 1, p. 13 884, 2020.
- [12] S. A. Nauroze, L. S. Novelino, M. M. Tentzeris, and G. H. Paulino, "Continuous-range tunable multilayer frequency-selective surfaces using origami and inkjet printing," *Proceedings of the National Academy of Sciences*, vol. 115, no. 52, pp. 13 210–13 215, 2018. eprint: <https://www.pnas.org/content/115/52/13210.full.pdf>.
- [13] S. A. Nauroze and M. M. Tentzeris, "Fully inkjet-printed multi-layer tunable origami fss structures with integrated thermal actuation mechanism," in *2019 IEEE MTT-S International Microwave Symposium (IMS)*, 2019, pp. 1363–1366.
- [14] M. Shirazi, J. Huang, T. Li, and X. Gong, "A switchable-frequency slot-ring antenna element for designing a reconfigurable array," *IEEE Antennas and Wireless Propagation Letters*, vol. 17, no. 2, pp. 229–233, 2018.
- [15] T. Li, H. Zhai, X. Wang, L. Li, and C. Liang, "Frequency-reconfigurable bow-tie antenna for bluetooth, wimax, and wlan applications," *IEEE Antennas and Wireless Propagation Letters*, vol. 14, pp. 171–174, 2015.
- [16] A. Zohur, H. Mopidevi, D. Rodrigo, M. Unlu, L. Jofre, and B. A. Cetiner, "Rf mems reconfigurable two-band antenna," *IEEE Antennas and Wireless Propagation Letters*, vol. 12, pp. 72–75, 2013.
- [17] C. won Jung, M. jer Lee, G. Li, and F. De Flaviis, "Reconfigurable scan-beam single-arm spiral antenna integrated with rf-mems switches," *IEEE Transactions on Antennas and Propagation*, vol. 54, no. 2, pp. 455–463, 2006.
- [18] T. Aboufoul, A. Alomainy, and C. Parini, "Reconfiguring uwb monopole antenna for cognitive radio applications using gaas fet switches," *IEEE Antennas and Wireless Propagation Letters*, vol. 11, pp. 392–394, 2012.
- [19] X. Liu, S. Yao, B. S. Cook, M. M. Tentzeris, and S. V. Georgakopoulos, "An origami reconfigurable axial-mode bifilar helical antenna," *IEEE Transactions on Antennas and Propagation*, vol. 63, no. 12, pp. 5897–5903, 2015.
- [20] J. Costantine, Y. Tawk, I. Maqueda, M. Sakovsky, G. Olson, S. Pellegrino, and C. G. Christodoulou, "Uhf deployable helical antennas for cubesats," *IEEE Transactions on Antennas and Propagation*, vol. 64, no. 9, pp. 3752–3759, 2016.
- [21] S. I. Hussain Shah, S. Ghosh, and S. Lim, "A novel dna inspired mode and frequency reconfigurable origami helical antenna," in *2018 IEEE International Sym-*

posium on Antennas and Propagation USNC/URSI National Radio Science Meeting, 2018, pp. 187–188.

- [22] S. I. H. Shah and S. Lim, “Bioinspired dna origami quasi-yagi helical antenna with beam direction and beamwidth switching capability,” *Scientific Reports*, vol. 9, no. 1, p. 14 312, 2019.
- [23] Y. Xu, Y. Kim, M. M. Tentzeris, and S. Lim, “Bi-directional loop antenna array using magic cube origami,” *Sensors (Basel, Switzerland)*, vol. 19, no. 18, 2019.
- [24] S. Lee, S. I. H. Shah, H. L. Lee, and S. Lim, “Frequency-reconfigurable antenna inspired by origami flasher,” *IEEE Antennas and Wireless Propagation Letters*, vol. 18, no. 8, pp. 1691–1695, 2019.
- [25] S. I. H. Shah, D. Lee, M. M. Tentzeris, and S. Lim, “A novel high-gain tetrahedron origami,” *IEEE Antennas and Wireless Propagation Letters*, vol. 16, pp. 848–851, 2017.
- [26] S. Yao, X. Liu, and S. V. Georgakopoulos, “Morphing origami conical spiral antenna based on the nojima wrap,” *IEEE Transactions on Antennas and Propagation*, vol. 65, no. 5, pp. 2222–2232, 2017.
- [27] M. Hamza, C. L. Zekios, and S. V. Georgakopoulos, “A thick origami reconfigurable and packable patch array with enhanced beam steering,” *IEEE Transactions on Antennas and Propagation*, vol. 68, no. 5, pp. 3653–3663, 2020.
- [28] M. Hwang, G. Kim, S. Kim, and N. S. Jeong, “Origami-inspired radiation pattern and shape reconfigurable dipole array antenna at c-band for cubesat applications,” *IEEE Transactions on Antennas and Propagation*, pp. 1–1, 2020.
- [29] W. Su, R. Bahr, S. A. Nauroze, and M. M. Tentzeris, “Novel 3d-printed “chinese fan” bow-tie antennas for origami/shape-changing configurations,” in *2017 IEEE International Symposium on Antennas and Propagation USNC/URSI National Radio Science Meeting*, 2017, pp. 1245–1246.
- [30] W. Su, S. A. Nauroze, B. Ryan, and M. M. Tentzeris, “Novel 3d printed liquid-metal-alloy microfluidics-based zigzag and helical antennas for origami reconfigurable antenna “trees”,” in *2017 IEEE MTT-S International Microwave Symposium (IMS)*, 2017, pp. 1579–1582.
- [31] J. Kimionis, M. Isakov, B. S. Koh, A. Georgiadis, and M. M. Tentzeris, “3d-printed origami packaging with inkjet-printed antennas for rf harvesting sensors,” *IEEE Transactions on Microwave Theory and Techniques*, vol. 63, no. 12, pp. 4521–4532, 2015.

- [32] R. Bahr, A. Nauroze, W. Su, and M. M. Tentzeris, “Self-actuating 3d printed packaging for deployable antennas,” in *2017 IEEE 67th Electronic Components and Technology Conference (ECTC)*, 2017, pp. 1425–1430.
- [33] U. M. Dilberoglu, B. Gharehpapagh, U. Yaman, and M. Dolen, “The role of additive manufacturing in the era of industry 4.0,” *Procedia Manufacturing*, vol. 11, pp. 545–554, 2017, 27th International Conference on Flexible Automation and Intelligent Manufacturing, FAIM2017, 27-30 June 2017, Modena, Italy.
- [34] A. Kumar, “Methods and materials for smart manufacturing: Additive manufacturing, internet of things, flexible sensors and soft robotics,” *Manufacturing Letters*, vol. 15, pp. 122–125, 2018, Industry 4.0 and Smart Manufacturing.
- [35] R. Prabhu, S. R. Miller, T. W. Simpson, and N. A. Meisel, “Exploring the Effects of Additive Manufacturing Education on Students’ Engineering Design Process and its Outcomes,” *Journal of Mechanical Design*, vol. 142, no. 4, Nov. 2019, 042001. eprint: https://asmedigitalcollection.asme.org/mechanicaldesign/article-pdf/142/4/042001/6436899/md_142_4_042001.pdf.
- [36] C. Culmone, G. Smit, and P. Breedveld, “Additive manufacturing of medical instruments: A state-of-the-art review,” *Additive Manufacturing*, vol. 27, pp. 461–473, 2019.
- [37] E. Sacco and S. K. Moon, “Additive manufacturing for space: Status and promises,” *The International Journal of Advanced Manufacturing Technology*, vol. 105, no. 10, pp. 4123–4146, 2019.
- [38] S. M. Wagner and R. O. Walton, “Additive manufacturing’s impact and future in the aviation industry,” *Production Planning & Control*, vol. 27, no. 13, pp. 1124–1130, 2016. eprint: <https://doi.org/10.1080/09537287.2016.1199824>.
- [39] Optomec, “Aerosol jet® printed electronics overview,” Tech. Rep., Jan. 2014.
- [40] T. Seifert, E. Sowade, F. Roscher, M. Wiemer, T. Gessner, and R. R. Baumann, “Additive manufacturing technologies compared: Morphology of deposits of silver ink using inkjet and aerosol jet printing,” *Industrial & Engineering Chemistry Research*, vol. 54, no. 2, pp. 769–779, 2015.
- [41] R. R. Søndergaard, M. Hösel, and F. C. Krebs, “Roll-to-roll fabrication of large area functional organic materials,” *Journal of Polymer Science Part B: Polymer Physics*, vol. 51, no. 1, pp. 16–34, 2013. eprint: <https://onlinelibrary.wiley.com/doi/pdf/10.1002/polb.23192>.
- [42] *Super inkjet printer*, SIJ-S030, SIJTechnology, Inc., 2020.

- [43] J. Kimionis, M. Isakov, B. S. Koh, A. Georgiadis, and M. M. Tentzeris, “3d-printed origami packaging with inkjet-printed antennas for rf harvesting sensors,” *IEEE Transactions on Microwave Theory and Techniques*, vol. 63, no. 12, pp. 4521–4532, 2015.
- [44] M. F. Farooqui and A. Shamim, “3-d inkjet-printed helical antenna with integrated lens,” *IEEE Antennas and Wireless Propagation Letters*, vol. 16, pp. 800–803, 2017.
- [45] S. Choi, W. Su, M. M. Tentzeris, and S. Lim, “A novel fluid-reconfigurable advanced and delayed phase line using inkjet-printed microfluidic composite right/left-handed transmission line,” *IEEE Microwave and Wireless Components Letters*, vol. 25, no. 2, pp. 142–144, 2015.
- [46] B. K. Tehrani, R. A. Bahr, W. Su, B. S. Cook, and M. M. Tentzeris, “E-band characterization of 3d-printed dielectrics for fully-printed millimeter-wave wireless system packaging,” in *2017 IEEE MTT-S International Microwave Symposium (IMS)*, 2017, pp. 1756–1759.
- [47] T.-H. Lin, S. N. Daskalakis, A. Georgiadis, and M. M. Tentzeris, “Achieving fully autonomous system-on-package designs: An embedded-on-package 5g energy harvester within 3d printed multilayer flexible packaging structures,” in *2019 IEEE MTT-S International Microwave Symposium (IMS)*, 2019, pp. 1375–1378.
- [48] A. C. de Leon, Q. Chen, N. B. Palaganas, J. O. Palaganas, J. Manapat, and R. C. Advincula, “High performance polymer nanocomposites for additive manufacturing applications,” *Reactive and Functional Polymers*, vol. 103, pp. 141–155, 2016.
- [49] D. Espalin, J. Ramírez, F. Medina, and R. Wicker, “Multi-material, multi-technology fdm: Exploring build process variations,” *Rapid Prototyping Journal*, vol. 20, pp. 236–244, 2014.
- [50] B. Zhang, W. Chen, Y. Wu, K. Ding, and R. Li, “Review of 3d printed millimeter-wave and terahertz passive devices,” *International journal of antennas and propagation*, vol. 2017, pp. 1–10, 2017.
- [51] *What resolution can 3d printers print? — all3dp*, <https://all3dp.com/3d-printer-resolution/>, (Accessed on 08/24/2022).
- [52] H. Quan, T. Zhang, H. Xu, S. Luo, J. Nie, and X. Zhu, “Photo-curing 3d printing technique and its challenges,” *Bioactive Materials*, vol. 5, no. 1, pp. 110–115, 2020.
- [53] B. K. Tehrani, S. A. Nauroze, R. A. Bahr, and M. M. Tentzeris, “On-package mm-wave fss integration with 3d-printed encapsulation,” in *2017 IEEE International*

Symposium on Antennas and Propagation USNC/URSI National Radio Science Meeting, 2017, pp. 9–10.

- [54] *Form 3+: Industrial-quality desktop sla 3d printer*, <https://formlabs.com/3d-printers/form-3/>, (Accessed on 08/24/2022).
- [55] *Dimatix materials printer dmp-2850: Support — fujifilm [united states]*, <https://www.fujifilm.com/us/en/business/inkjet-solutions/deposition-products/dmp-2850/support>, (Accessed on 08/24/2022).
- [56] B. K. Tehrani, B. S. Cook, and M. M. Tentzeris, “Inkjet printing of multilayer millimeter-wave yagi-uda antennas on flexible substrates,” *IEEE Antennas and Wireless Propagation Letters*, vol. 15, pp. 143–146, 2016.
- [57] J. Kimionis, S. Shahramian, Y. Baeyens, A. Singh, and M. M. Tentzeris, “Pushing inkjet printing to w-band: An all-printed 90-ghz beamforming array,” in *2018 IEEE/MTT-S International Microwave Symposium - IMS*, 2018, pp. 63–66.
- [58] R. A. Bahr, Y. Fang, W. Su, B. Tehrani, V. Palazzi, and M. M. Tentzeris, “Novel uniquely 3d printed intricate voronoi and fractal 3d antennas,” in *2017 IEEE MTT-S International Microwave Symposium (IMS)*, 2017, pp. 1583–1586.
- [59] X. He, K. Hu, Y. Cui, R. Bahr, B. Tehrani, and M. Tentzeris, “Additively manufactured “smart” rf packaging structures: A quantum leap for on-demand customizable integrated 5g and iot modules,” *IEEE Microwave Magazine*, vol. 8, 2022.
- [60] X. He, Y. Fang, R. A. Bahr, and M. M. Tentzeris, “Rf systems on antenna (soa): A novel integration approach enabledby additive manufacturing,” in *2020 IEEE MTT-S International Microwave Symposium (IMS)*, 2020.
- [61] T.-H. Lin, S. N. Daskalakis, A. Georgiadis, and M. M. Tentzeris, “Achieving fully autonomous system-on-package designs: An embedded-on-package 5g energy harvester within 3d printed multilayer flexible packaging structures,” in *2019 IEEE MTT-S International Microwave Symposium (IMS)*, 2019, pp. 1375–1378.
- [62] A. Vena, L. Sydänheimo, L. Ukkonen, and M. M. Tentzeris, “A fully inkjet-printed chipless rfid gas and temperature sensor on paper,” in *2014 IEEE RFID Technology and Applications Conference (RFID-TA)*, 2014, pp. 115–120.
- [63] S. Kim, T. Le, M. M. Tentzeris, A. Harrabi, A. Collado, and A. Georgiadis, “An rfid-enabled inkjet-printed soil moisture sensor on paper for “smart” agricultural applications,” in *SENSORS, 2014 IEEE*, 2014, pp. 1507–1510.
- [64] Y. Kawahara, H. Lee, and M. Tentzeris, “Sensprout: Inkjet-printed soil moisture and leaf wetness sensor,” Sep. 2012, pp. 545–545.

- [65] S. Kim, Y. Kawahara, A. Georgiadis, A. Collado, and M. M. Tentzeris, “Low-cost inkjet-printed fully passive rfid tags for calibration-free capacitive/haptic sensor applications,” *IEEE Sensors Journal*, vol. 15, no. 6, pp. 3135–3145, 2015.
- [66] W. Su, B. S. Cook, Y. Fang, and M. M. Tentzeris, “Fully inkjet-printed microfluidics: A solution to low-cost rapid three-dimensional microfluidics fabrication with numerous electrical and sensing applications,” *Scientific Reports*, vol. 6, no. 1, p. 35 111, 2016.
- [67] B. S. Cook, J. R. Cooper, and M. M. Tentzeris, “An inkjet-printed microfluidic rfid-enabled platform for wireless lab-on-chip applications,” *IEEE Transactions on Microwave Theory and Techniques*, vol. 61, no. 12, pp. 4714–4723, 2013.
- [68] W. Su, Q. Liu, B. Cook, and M. Tentzeris, “All-inkjet-printed microfluidics-based encodable flexible chipless rfid sensors,” in *2016 IEEE MTT-S International Microwave Symposium (IMS)*, 2016, pp. 1–4.
- [69] R. Baccarelli, G. Orecchini, F. Alimenti, and L. Roselli, “Feasibility study of a fully organic, cnt based, harmonic rfid gas sensor,” in *2012 IEEE International Conference on RFID-Technologies and Applications (RFID-TA)*, 2012, pp. 419–422.
- [70] B. Turki, M. Ali Ziai, A. Hillier, K. Belsey, A. Parry, S. Yeates, J. C. Batchelor, and S. Holder, “Chemical vapor detecting passive rfid tag,” in *2019 IEEE International Conference on RFID Technology and Applications (RFID-TA)*, 2019, pp. 113–115.
- [71] T. Lin, R. Bahr, M. Tentzeris, R. Pulugurtha, V. Sundaram, and R. Tummala, “Novel 3d-/inkjet-printed flexible on-package antennas, packaging structures, and modules for broadband 5g applications,” in *2018 IEEE 68th Electronic Components and Technology Conference (ECTC)*, 2018, pp. 214–220.
- [72] B. K. Tehrani, R. A. Bahr, W. Su, B. S. Cook, and M. M. Tentzeris, “E-band characterization of 3d-printed dielectrics for fully-printed millimeter-wave wireless system packaging,” in *2017 IEEE MTT-S International Microwave Symposium (IMS)*, 2017, pp. 1756–1759.
- [73] F. Walther, T. Drobek, A. M. Gigler, M. Hennemeyer, M. Kaiser, H. Herberg, T. Shimitsu, G. Morfill, and R. Stark, “Surface hydrophilization of su-8 by plasma and wet chemical processes,” *Surface and Interface Analysis*, vol. 42, pp. 1735 –1744, Dec. 2010.
- [74] S. A. Nauroze, L. Novelino, M. M. Tentzeris, and G. H. Paulino, “Inkjet-printed “4d” tunable spatial filters using on-demand foldable surfaces,” in *2017 IEEE MTT-S International Microwave Symposium (IMS)*, 2017, pp. 1575–1578.

- [75] B. Munk, *Frequency selective surfaces: theory and design*. John Wiley, 2000.
- [76] B. A. Munk, *Finite antenna arrays and FSS*. IEEE Press, 2003.
- [77] J. A. Stankovic, “Wireless sensor networks,” *Computer*, vol. 41, no. 10, pp. 92–95, 2008.
- [78] J. Huang, *Reflectarray Antennas*. Wiley-IEEE Press, 2007, ISBN: 047008491X.
- [79] A. J. Rubio, A.-S. Kaddour, N. Brown, L. L. Howell, S. P. Magleby, and S. V. Georgakopoulos, “A physically reconfigurable origami reflectarray based on the augmented square twist pattern,” in *2021 IEEE Texas Symposium on Wireless and Microwave Circuits and Systems (WMCS)*, 2021, pp. 1–4.
- [80] M. Cooley, B. Yon, D. Konapelsky, D. Sall, R. March, A. Harris, S. Yen, N. Fasanella, S. Wilson, E. Tomek, T. Chambers, N. Stickle, C. Peter, E. Rahul, T. Ring, and M. Wiens, “Rf design and development of a deployable membrane reflectarray antenna for space,” in *2019 IEEE International Symposium on Phased Array System Technology (PAST)*, 2019, pp. 1–4.
- [81] R. E. Hodges, N. Chahat, D. J. Hoppe, and J. D. Vacchione, “A deployable high-gain antenna bound for mars: Developing a new folded-panel reflectarray for the first cubesat mission to mars.,” *IEEE Antennas and Propagation Magazine*, vol. 59, no. 2, pp. 39–49, 2017.
- [82] G. Wu, S. Qu, and S. Yang, “Wide-angle beam-scanning reflectarray with mechanical steering,” *IEEE Transactions on Antennas and Propagation*, vol. 66, no. 1, pp. 172–181, 2018.
- [83] S. R. Rengarajan, “Scanning and defocusing characteristics of microstrip reflectarrays,” *IEEE Antennas and Wireless Propagation Letters*, vol. 9, pp. 163–166, 2010.
- [84] P. Nayeri, F. Yang, and A. Z. Elsherbeni, “Bifocal design and aperture phase optimizations of reflectarray antennas for wide-angle beam scanning performance,” *IEEE Transactions on Antennas and Propagation*, vol. 61, no. 9, pp. 4588–4597, 2013.
- [85] Y. Qu, C. Guo, W. Peng, J. Ding, Y. Gao, and Y.-C. Song, “Design of a bifocal single reflectarray antenna with improving beam scanning performance,” *The Open Electrical & Electronic Engineering Journal*, vol. 9, pp. 200–207, 2015.
- [86] E. Martinez-de Rioja, J. A. Encinar, and G. Toso, “Bifocal dual-reflectarray antenna to generate a complete multiple spot beam coverage for satellite communications in ka-band,” *Electronics*, vol. 9, no. 6, 2020.

- [87] F. Yang, P. Nayeri, A. Z. Elsherbeni, J. C. Ginn, D. J. Shelton, G. D. Boreman, and Y. Rahmat-Samii, "Reflectarray design at infrared frequencies: Effects and models of material loss," *IEEE Transactions on Antennas and Propagation*, vol. 60, no. 9, pp. 4202–4209, 2012.
- [88] P. Nayeri, M. Liang, R. A. Sabory-García, M. Tuo, F. Yang, M. Gehm, H. Xin, and A. Z. Elsherbeni, "3d printed dielectric reflectarrays: Low-cost high-gain antennas at sub-millimeter waves," *IEEE Transactions on Antennas and Propagation*, vol. 62, no. 4, pp. 2000–2008, 2014.
- [89] R. Deng, F. Yang, S. Xu, and M. Li, "Radiation performances of conformal dielectric reflectarray antennas at sub-millimeter waves," in *2016 IEEE International Conference on Microwave and Millimeter Wave Technology (ICMMT)*, vol. 1, 2016, pp. 217–219.
- [90] S. Zhang, "Three-dimensional printed millimetre wave dielectric resonator reflectarray," *IET Microwaves, Antennas Propagation*, vol. 11, no. 14, pp. 2005–2009, 2017.
- [91] M. h. Jamaluddin, R. Sauleau, X. Castel, R. Benzerger, L. Coq, R. Gillard, and T. Koleck, "Design, fabrication and characterization of a dielectric resonator antenna reflectarray in ka-band," *Progress In Electromagnetics Research B*, vol. 25, pp. 261–275, Jan. 2010.
- [92] F. Ahmadi, K. Forooraghi, Z. Atlasbaf, and B. Virdee, "Dual linear-polarized dielectric resonator reflectarray antenna," *IEEE Antennas and Wireless Propagation Letters*, vol. 12, pp. 635–638, 2013.
- [93] Y. Sun and K. W. Leung, "Millimeter-wave substrate-based dielectric reflectarray," *IEEE Antennas and Wireless Propagation Letters*, vol. 17, no. 12, pp. 2329–2333, 2018.
- [94] M. Abd-Elhady, W. Hong, and Y. Zhang, "A ka-band reflectarray implemented with a single-layer perforated dielectric substrate," *IEEE Antennas and Wireless Propagation Letters*, vol. 11, pp. 600–603, 2012.
- [95] T. Castle, D. M. Sussman, M. Tanis, and R. D. Kamien, "Additive lattice kirigami," *Science Advances*, vol. 2, no. 9, 2016. eprint: <https://advances.sciencemag.org/content/2/9/e1601258.full.pdf>.
- [96] A. Rafsanjani, A. Akbarzadeh, and D. Pasini, "Snapping mechanical metamaterials under tension," *Advanced Materials*, vol. 27, p. 5931, Oct. 2015.
- [97] Y. Cui, S. A. Nauroze, R. Bahr, and E. M. Tentzeris, "3d printed one-shot deployable flexible "kirigami" dielectric reflectarray antenna for mm-wave applications,"

in *2020 IEEE/MTT-S International Microwave Symposium (IMS)*, 2020, pp. 1164–1167.

- [98] J. Han, L. Li, G. Liu, Z. Wu, and Y. Shi, “A wideband 1 bit 12×12 reconfigurable beam-scanning reflectarray: Design, fabrication, and measurement,” *IEEE Antennas and Wireless Propagation Letters*, vol. 18, no. 6, pp. 1268–1272, 2019.
- [99] M. Zhang, S. Gao, Y. Jiao, J. Wan, B. Tian, C. Wu, and A. Farrall, “Design of novel reconfigurable reflectarrays with single-bit phase resolution for ku-band satellite antenna applications,” *IEEE Transactions on Antennas and Propagation*, vol. 64, no. 5, pp. 1634–1641, 2016.
- [100] X. Yang, S. Xu, F. Yang, M. Li, Y. Hou, S. Jiang, and L. Liu, “A broadband high-efficiency reconfigurable reflectarray antenna using mechanically rotational elements,” *IEEE Transactions on Antennas and Propagation*, vol. 65, no. 8, pp. 3959–3966, 2017.
- [101] X. Yang, S. Xu, F. Yang, M. Li, H. Fang, Y. Hou, S. Jiang, and L. Liu, “A mechanically reconfigurable reflectarray with slotted patches of tunable height,” *IEEE Antennas and Wireless Propagation Letters*, vol. 17, no. 4, pp. 555–558, 2018.
- [102] T. Niu, J. Zhang, L. Cheng, P. Cao, R. Cui, and Z. Mei, “Reconfigurable terahertz reflectarray based on graphene radiating patches,” in *2020 14th European Conference on Antennas and Propagation (EuCAP)*, 2020, pp. 1–4.
- [103] S. A. Long and G. H. Huff, “A fluidic loading mechanism for phase reconfigurable reflectarray elements,” *IEEE Antennas and Wireless Propagation Letters*, vol. 10, pp. 876–879, 2011.
- [104] Z. Wang, F. Zhang, H. Gao, O. Franek, G. F. Pedersen, and W. Fan, “Over-the-air array calibration of mmwave phased array in beam-steering mode based on measured complex signals,” *IEEE Transactions on Antennas and Propagation*, vol. 69, no. 11, pp. 7876–7888, 2021.
- [105] O. Bucci, M. Migliore, G. Panariello, and P. Sgambato, “Accurate diagnosis of conformal arrays from near-field data using the matrix method,” *IEEE Transactions on Antennas and Propagation*, vol. 53, no. 3, pp. 1114–1120, 2005.
- [106] M. D. Migliore, “A compressed sensing approach for array diagnosis from a small set of near-field measurements,” *IEEE Transactions on Antennas and Propagation*, vol. 59, no. 6, pp. 2127–2133, 2011.
- [107] S. Islam and C. Fulton, “Fixed probe based one-shot calibration technique for small digital phased array,” in *2019 IEEE International Symposium on Phased Array System and Technology (PAST)*, 2019, pp. 1–5.

- [108] I. Gupta, J. Baxter, S. Ellingson, H.-G. Park, H. S. Oh, and M. G. Kyeong, “An experimental study of antenna array calibration,” *IEEE Transactions on Antennas and Propagation*, vol. 51, no. 3, pp. 664–667, 2003.
- [109] A. C. Fikes, A. Safaripour, F. Bohn, B. Abiri, and A. Hajimiri, “Flexible, conformal phased arrays with dynamic array shape self-calibration,” in *2019 IEEE MTT-S International Microwave Symposium (IMS)*, 2019, pp. 1458–1461.
- [110] J. Zhang, H. Kang, N. Hu, Y. Chen, J. Huang, Y. Qin, S. Zha, and X. Huang, “Structural mutual coupling calibration experiments of full polarization conformal phased array,” in *2019 Joint International Symposium on Electromagnetic Compatibility, Sapporo and Asia-Pacific International Symposium on Electromagnetic Compatibility (EMC Sapporo/APEMC)*, 2019, pp. 700–703.
- [111] D. Bekers, R. van Dijk, and F. van Vliet, “Mutual-coupling based phased-array calibration: A robust and versatile approach,” in *2013 IEEE International Symposium on Phased Array Systems and Technology*, 2013, pp. 630–637.
- [112] *The green bank telescope laser metrology computer control system*, <https://www.adass.org/adass/proceedings/adass98/creagerre/>, (Accessed on 08/24/2022).
- [113] J. Geng, “Structured-light 3d surface imaging: A tutorial,” *Adv. Opt. Photon.*, vol. 3, no. 2, pp. 128–160, 2011.
- [114] *Streaming depth data from the truedepth camera — apple developer documentation*, https://developer.apple.com/documentation/avfoundation/additional_data_capture/streaming_depth_data_from_the_truedepth_camera, (Accessed on 08/24/2022).
- [115] K. Hu, X. He, and M. M. Tentzeris, “Flexible and scalable additively manufactured antenna array tiles for satellite and 5g applications using a novel rugged microstrip-to-microstrip transition,” in *2021 IEEE International Symposium on Antennas and Propagation and USNC-URSI Radio Science Meeting (APS/URSI)*, 2021, pp. 37–38.
- [116] P. P. Pratapa, K. Liu, and G. H. Paulino, “Geometric mechanics of origami patterns exhibiting poisson’s ratio switch by breaking mountain and valley assignment,” *Phys. Rev. Lett.*, vol. 122, p. 155 501, 15 2019.
- [117] R. Xie, Y. Chen, and J. M. Gattas, “Parametrisation and application of cube and eggbox-type folded geometries,” *International Journal of Space Structures*, vol. 30, no. 2, pp. 99–110, 2015. eprint: <https://doi.org/10.1260/0266-3511.30.2.99>.

- [118] H. Nassar, A. Lebé, and L. Monasse, “Curvature, metric and parametrization of origami tessellations: Theory and application to the eggbox pattern,” *Proceedings of the Royal Society A: Mathematical, Physical and Engineering Sciences*, vol. 473, no. 2197, p. 20 160 705, 2017.
- [119] G. I. Kiani, L. G. Olsson, A. Karlsson, K. P. Esselle, and M. Nilsson, “Cross-dipole bandpass frequency selective surface for energy-saving glass used in buildings,” *IEEE Transactions on Antennas and Propagation*, vol. 59, no. 2, pp. 520–525, 2011.
- [120] F. C. Seman, S. Omar, F. Poad, W. Y. Yong, S. K. A. Rahim, E. Baharudin, and S. Shah, “Phase characteristics of multi-layer crossed-dipole fss in salisbury screen absorber,” in *2018 IEEE International RF and Microwave Conference (RFM)*, 2018, pp. 356–358.
- [121] P. Majumdar, Z. Zhao, Y. Yue, C. Ji, and R. Liu, “Equivalent circuit model of cross and circular ring fss using vector fitting,” in *Proceedings of 2014 3rd Asia-Pacific Conference on Antennas and Propagation*, 2014, pp. 1042–1045.
- [122] Y. Zouaoui, L. Talbi, and K. Hettak, “Cross dipole fss bandwidth enhancement,” in *2019 IEEE International Symposium on Antennas and Propagation and USNC-URSI Radio Science Meeting*, 2019, pp. 947–948.
- [123] S. A. Nauroze, J. G. Hester, B. K. Tehrani, W. Su, J. Bito, R. Bahr, J. Kimionis, and M. M. Tentzeris, “Additively manufactured rf components and modules: Toward empowering the birth of cost-efficient dense and ubiquitous iot implementations,” *Proceedings of the IEEE*, vol. 105, no. 4, pp. 702–722, 2017.
- [124] D. Helena, A. Ramos, T. Varum, and J. N. Matos, “Antenna design using modern additive manufacturing technology: A review,” *IEEE Access*, vol. 8, pp. 177 064–177 083, 2020.
- [125] H. Xuanke, H. Kexin, C. Yepu, B. Ryan, T. Bijan, and M. T. Manos, “Additively manufactured “smart” rf packaging structures: A quantum leap for on-demand customizable integrated 5g and iot modules,” *IEEE Microwave Magazine*, 2022.
- [126] Y. Xie, Y. Fu, Z. Jia, J. Li, C. Shen, Y. Xu, H. Chen, and S. A. Cummer, “Acoustic imaging with metamaterial luneburg lenses,” *Scientific Reports*, vol. 8, no. 1, p. 16 188, 2018.
- [127] Y. Cui, S. A. Nauroze, R. Bahr, and E. M. Tentzeris, “3d printed one-shot deployable flexible “kirigami” dielectric reflectarray antenna for mm-wave applications,” in *2020 IEEE/MTT-S International Microwave Symposium (IMS)*, 2020, pp. 1164–1167.

- [128] Y.-X. Zhang, Y.-C. Jiao, and S.-B. Liu, “3-d-printed comb mushroom-like dielectric lens for stable gain enhancement of printed log-periodic dipole array,” *IEEE Antennas and Wireless Propagation Letters*, vol. 17, no. 11, pp. 2099–2103, 2018.
- [129] Y. Li, L. Ge, M. Chen, Z. Zhang, Z. Li, and J. Wang, “Multibeam 3-d-printed luneburg lens fed by magnetoelectric dipole antennas for millimeter-wave mimo applications,” *IEEE Transactions on Antennas and Propagation*, vol. 67, no. 5, pp. 2923–2933, 2019.
- [130] S. Sahin, N. K. Nahar, and K. Sertel, “Dielectric properties of low-loss polymers for mmw and thz applications,” *Journal of Infrared, Millimeter, and Terahertz Waves*, vol. 40, no. 5, pp. 557–573, 2019.
- [131] A. M. Nicolson and G. F. Ross, “Measurement of the intrinsic properties of materials by time-domain techniques,” *IEEE Transactions on Instrumentation and Measurement*, vol. 19, no. 4, pp. 377–382, 1970.
- [132] *Porcelite guideline copy 4.pages*, <https://tethon3d.com/wp-content/uploads/Porcelite-User-Guide.pdf>, (Accessed on 08/24/2022).
- [133] B. Tehrani, R. Bahr, D. Revier, B. Cook, and M. Tentzeris, “The principles of ”smart” encapsulation: Using additive printing technology for the realization of intelligent application-specific packages for iot, 5g, and automotive radar applications,” in *2018 IEEE 68th Electronic Components and Technology Conference (ECTC)*, 2018, pp. 111–117.
- [134] P. Nayeri, M. Liang, R. A. Sabory-García, M. Tuo, F. Yang, M. Gehm, H. Xin, and A. Z. Elsherbeni, “3d printed dielectric reflectarrays: Low-cost high-gain antennas at sub-millimeter waves,” *IEEE Transactions on Antennas and Propagation*, vol. 62, no. 4, pp. 2000–2008, 2014.
- [135] Y. Cui, S. A. Nauroze, R. Bahr, and E. M. Tentzeris, “3d printed one-shot deployable flexible “kirigami” dielectric reflectarray antenna for mm-wave applications,” in *2020 IEEE/MTT-S International Microwave Symposium (IMS)*, 2020, pp. 1164–1167.
- [136] S. Zhang, “Three-dimensional printed millimetre wave dielectric resonator reflectarray,” *IET Microwaves, Antennas Propagation*, vol. 11, no. 14, pp. 2005–2009, 2017.
- [137] *3d-printing-design-guide-final.pdf*, <https://multimedia.3m.com/mws/media/16537540/3d-printing-design-guide-final.pdf>, (Accessed on 08/24/2022).

- [138] Y. Cui, A. Eid, and M. M. Tentzeris, “A 3d-printed mm-wave deployable origami dielectric reflectarray antenna,” in *2020 IEEE International Symposium on Antennas and Propagation and North American Radio Science Meeting*, 2020, pp. 1679–1680.
- [139] *Microsoft word - antennameasurement.doc*, <https://ewh.ieee.org/r6/scv/aps/archives/2010Hillbun.pdf>, (Accessed on 08/24/2022).